International Doctorate on AstroParticle Physics

Università degli Studi di Milano
Dipartimento di Fisica
Scuola di Dottorato di Ricerca
Ciclo XXVII

Université Paris Diderot
École Doctorale 560 STEP'UP:
Sciences de la Terre et Physique de l'univers

Mass composition studies of Ultra High Energy cosmic rays through the measurement of the Muon Production Depths at the Pierre Auger Observatory

Thesis presented by
Laura Collica

Supervisors
Lino Miramonti
Antoine Letessier-Selvon

Directors of the Doctoral Schools
Marco Bersanelli
Yannick Giraud-Héraud

Referees

Corinne Bérat	LPSC Grenoble
Antonella Castellina	INAF/INFN Torino

Defended on November 28, 2014 in front of the Jury composed by

Antonio Insolia	Univ. Catania/INFN
Corinne Bérat	LPSC Grenoble
Antonella Castellina	INAF/INFN Torino
Olivier Deligny	IPN CNRS Paris
Antoine Letessier-Selvon	LPNHE CNRS Paris
Lino Miramonti	Univ. Milano/INFN

Acknowledgements

"The number of lives that enter our own is incalculable."
John Berger

Working in the Auger collaboration allowed me to grow as a scientist and as a person. For that I am grateful to my supervisor Lino Miramonti who gave me the possibility to do the PhD in Auger and who encouraged me all the time.

I would like to express my gratitude to my supervisor Antoine Letessier-Selvon, who has welcomed me in the LPNHE Auger group in Paris and from whom I have learned a much.

I would like to thank my referees, Antonella Castellina and Corinne Berat, for the very constructive comments and recommendations. In particular, Antonella Castellina encouraged me and guided constantly during this research work and I am deeply grateful to her for that.

Thanks to my collegues in Milan, Barbara Caccianiga and Marco Giammarchi, for the constant support they showed me.

A grateful thought goes to Viviana Scherini, Lorenzo Perrone and Mariangela Settimo, for the kindness and the assistance provided during the different phases of this project. I am also grateful to Olivier Deligny, who gave me useful advice and remarks to my work.

Then, I am thankful to Alessandra Tonazzo, who helped me with the paperwork in Paris.

Many friends have supported me during the last years (too many to list here but you know who you are!). I greatly value their friendship and I deeply appreciate their belief in me. A special thought goes to Matte, Sere, Duda and Eli: thank you for listening and offering me advice whenever I needed it.

Most importantly, none of this would have been possible without the love and patience of my family. I would like to express my heart-felt gratitude to my family, who constantly supports me despite the distance.

Thanks to all, for all I have learned and the experiences I had.

"Todo pasa y todo queda,
pero lo nuestro es pasar,
pasar haciendo caminos,
caminos sobre la mar.

Nunca persegui la gloria,
ni dejar en la memoria
de los hombres mi cancion;
yo amo los mundos sutiles,
ingravidos y gentiles,
como pompas de jabon.

Me gusta verlos pintarse
de sol y grana, volar
bajo el cielo azul, temblar
subitamente y quebrarse...
Nunca persegui la gloria.

Caminante, son tus huellas
el camino y nada mas;
caminante, no hay camino,
se hace camino al andar.

Al andar se hace camino
y al volver la vista atras
se ve la senda que nunca
se ha de volver a pisar.

Caminante no hay camino
sino estelas en la mar..."

Antonio Machado

Contents

Abstract **1**

Resumé **3**

1 Ultra High Energy Cosmic Rays **5**
1.1 Energy spectrum 5
    1.1.1 The Ankle energy region 6
    1.1.2 End of the spectrum 8
1.2 Sources 10
    1.2.1 Bottom-up models 10
    1.2.2 Top-down models 13
1.3 Propagation 13
    1.3.1 Magnetic fields 13
    1.3.2 Interaction with the background radiation fields 14

2 Extensive Air Showers **17**
2.1 Physics of EAS 17
    2.1.1 Heitler's model of electromagnetic showers 18
    2.1.2 Hadronic showers 19
2.2 EAS Simulations 21
2.3 The muon component at ground 22
2.4 EAS detection techniques 25
    2.4.1 Ground arrays 25
    2.4.2 Atmospheric light detectors 26
    2.4.3 UHECR detectors 28

3 The Pierre Auger Observatory **31**
3.1 Fluorescence Detector 31
    3.1.1 FD Calibration 32
    3.1.2 FD Trigger 34
    3.1.3 Geometric reconstruction with the FD 34
    3.1.4 The longitudinal profile and the energy reconstruction with the FD 35
3.2 Surface Detector 36
    3.2.1 SD Calibration 37
    3.2.2 SD trigger and event selection 37

3.2.3 SD aperture and exposure 38
3.2.4 Geometric reconstruction with the SD 39
3.2.5 Energy reconstruction with the SD 39

4 Overview of Mass Composition Studies at Auger 43
4.1 FD observable sensitive to mass 43
4.1.1 X_{max} and RMS(X_{max}) measurement 44
4.1.2 $\langle lnA \rangle$ measurement 45
4.2 SD observables sensitive to mass 47
4.2.1 Risetime Asymmetry 47
4.2.2 Measurement of the muon signal using vertical events 48
4.2.2.1 The Muon fraction and the muon signal 50
4.2.2.2 The muon signal scaling 51
4.2.3 Measurement of the muon signal using horizontal events 52
4.3 Muon production depth reconstruction 54
4.3.1 The muon time distributions model 54
4.3.2 The MPD analysis for inclined events 57
4.4 Current status of the measurements of mass composition of UHECRs 61

5 The Smoothing Method 65
5.1 The smoothing 65
5.2 Optimization of the convolute range 69
5.3 Evaluation of the physical background 71
5.4 Method accuracy 74
5.4.1 The dependence on the hadronic model 76

6 Extension of the Muon Production Depth Analysis: MC studies 81
6.1 The apparent MPD profile: reconstruction limit at ground 81
6.2 Universal Shower Profile Function 83
6.3 The apparent MPD profile: dependence on primary zenith angle and energy 85
6.4 The apparent MPD profile: dependence on hadronic models 89

7 Extension of the Muon Production Depth Analysis: SD reconstruction 91
7.1 Detector Effects and Electromagnetic contamination 92
7.1.1 The Gold Deconvolution Algorithm 92
7.1.2 Evaluation and subtraction of the EM component 94
7.2 Optimization of the reconstruction bias 99
7.3 Method resolution 101

8 MPD Analysis: application to SD data 105
8.1 MPD reconstruction: summary 105
8.2 Data selection 106
8.3 Method systematics 106
8.4 The evolution of the measured X^{μ}_{max} with energy 108
8.5 The evolution of RMS(X^{μ}_{max}) with energy 109

9 Muon production depth reconstruction with LSD **113**
9.1 Beyond 2015: science case and technical strategy 113
9.2 Beyond 2015: proposed upgrades 114
9.2.1 Scintillator-based detectors 114
9.3 LSD 115
9.4 MPD reconstruction with the bottom layer 117
9.4.1 Reconstruction bias and resolution 119

Conclusions and outlook **123**

Bibliography **127**

Abstract

The Pierre Auger Observatory (Auger) in Argentina studies Ultra High Energy Cosmic Rays (UHECRs) physics. The flux of cosmic rays at these energies (above 10^{18} eV) is very low (less than 100 particle/km^2-year) and UHECR properties must be inferred from the measurements of the secondary particles that the cosmic ray primary produces in the atmosphere. These particles cascades are called *Extensive Air Showers* (EAS) and can be studied at ground by deploying detectors covering large areas. The EAS physics is complex, and the properties of secondary particles depend strongly on the first interaction, which takes place at an energy beyond the ones reached at accelerators. As a consequence, the analysis of UHECRs is subject to large uncertainties and hence many of their properties, in particular their composition, are still unclear.

Two complementary techniques are used at Auger to detect EAS initiated by UHECRs: a 3000 km^2 surface detector (SD) array of water Cherenkov tanks which samples particles at ground level and fluorescence detectors (FD) which collect the ultraviolet light emitted by the de-excitation of nitrogen nuclei in the atmosphere, and can operate only in clear, moonless nights. Auger is the largest cosmic rays detector ever built and it provides high-quality data together with unprecedented statistics.

The main goal of this thesis is the measurement of UHECR mass composition using data from the SD of the Pierre Auger Observatory. Measuring the cosmic ray composition at the highest energies is of fundamental importance from the astrophysical point of view, since it could discriminate between different scenarios of origin and propagation of cosmic rays. Moreover, mass composition studies are of utmost importance for particle physics. As a matter of fact, knowing the composition helps in exploring the hadronic interactions at ultra-high energies, inaccessible to present accelerator experiments.

The Auger Collaboration has published important results regarding mass composition of UHECRs using FD measurements [Aab et al. (2014)]. Nevertheless, it is crucial to study mass composition with SD data, in order to have an independent measurement that can either support or disfavor FD results. Besides, the almost 100% duty cycle of the SD yields an event statistics one order of magnitude greater than the FD one, which allows one to study composition at the highest energies.

In this context, the Auger Collaboration has recently published results regarding a method which uses the timing information from the SD signals to characterize the longitudinal development of the muon component of EAS [Aab et al. (2014)]. In particular, the method allows one to reconstruct the distribution of muon production depths (MPD), which carries information about the mass of primary particles. The so-called MPD analysis is applied to high energy inclined events only. In the present thesis we will discuss the extension of the method to a wider energy and zenith range.

Chapter 1 gives an overview of cosmic rays physics, discussing briefly their energy spectrum, origin and propagation. Chapter 2 describes the properties of EAS and the detection techniques exploited to study them. In chapter 3, the main features of the Pierre Auger Observatory are described in detail, including the reconstruction of the most relevant variables by both SD and FD. Chapter 4 gives an overview of the more important results achieved by the Auger Collaboration regarding the UHECRs mass composition. Chapters 5 describes the Smoothing Method, a technique which allows to measure the muon content of the showers by exploiting the different time distributions of muon and electromagnetic signals in SD detectors. The evaluation of its physical background and its accuracy is part of this thesis work. In Chapter 6 the MPD profile properties are discussed, in order to define the explorable analysis ranges in primary energy, primary zenith angle and distance from the core. In Chapter 7 the extension of the MPD reconstruction with SD is investigated. In particular we show that the two main problems related to the extension of the analysis, i.e. the EM contamination and the detector effects, can be solved by exploiting at the same time the Smoothing Method and the deconvolution of the muon signal with the tank response to muons. In Chapter 8 the proposed method is applied to SD data and the results obtained are discussed, together with the method systematics. Finally, in Chapter 9 the part of the thesis work carried out with the LPNHE group in Paris is described. In particular we have investigated the possibility to reconstruct the MPD profile with one of the proposed upgrade of Auger, the Layered Surface Detector (LSD).

Resumé

L'observatoire Pierre Auger, situé en Argentine, étudie la physique des rayons cosmiques de ultra haute énergie (UHECRs, i.e. $E > 10^{18}$ eV). Le flux de rayons cosmiques à cette énergies est faible et les propriétés doivent être déduite à partir des mesures des particules secondaires qui sont produites par les rayons cosmiques primaires dans l' atmosphère. Ces cascades sont appelées *gerbe atmosphériques étendues* (EAS) et peuvent être étudiés au sol en déployant des détecteurs couvrant de larges zones.

La physique des EAS est complexe et les propriétés des particules secondaires dépendent de la première intéraction, qui se déroule à un niveau d'énergie supérieur de ceux atteints dans les accélérateurs. En conséquence, l'analyse de UHECRs est soumis à d'importantes incertitudes et donc beaucoup de leurs propriétés, en particulier leur composition, sont encore inconnues.

Deux techniques complémentaires sont utilisées pour détecter le EAS initiées par UHECRs à Auger: un réseau de 1600 détecteurs couvrant 3000 km^2 qui échantillonnent les particules au niveau du sol (SD) et des détecteurs de fluorescence (FD) qui recueillent la lumière ultra-violette émise par la désexcitation des noyaux d'azote dans l'atmosphère, et ne peut fonctionner que pendant des nuits sans lune.

L'objectif principal de cette thèse est la mesure de la composition de la masse de UHECR à partir des données du SD de l'Observatoire Pierre Auger. La mesure de la composition des rayons cosmiques aux énergies les plus élevées est une clé obligatoire du point de vue astrophysique, car cela pourrait permettre de séparer les diffèrents scènarios d'origine et la propagation des rayons cosmiques. De plus, les études de composition de masse sont de la plus haute importance pour la physique des particules, car une fois la composition connue, on peut explorer l'interaction hadronique à des énergies inaccessibles aux accélérateurs d'aujourd'hui.

La collaboration Auger a publié des resultats importants concernant la composition de UHECRs utilisant des mesures FD [Abraham et al. (2010)]. Cependant, il est essentiel d'étudier la composition de masse avec les données SD, afin d'avoir une mesure indépendante qui peut soit soutenir soit contredire les resultats de FD. Par ailleurs, le cycle utile de 100 % du SD donne une analyse statistique d'événements un ordre de grandeur plus grand que celui de FD, permettant ainsi d'étudier la composition aux plus hautes énergies.

Dans ce contexte, la collaboration Auger a recemment publié des resultats concernant la méthode qui utilise les informations des signaux SD pour caractériser le développement longitudinal de muons des EAS [Aab et al. (2014)]. En particulier, la méthode permet de reconstruire la distribution des profondeurs de production de muons (*Muon Production Depth*), qui comporte des informations sur la masse des particules primaires. Cette

methode, est appliquée seulement aux événements inclinés à haute énergie. Dans cette thèse, nous allons discuter l'extension de la méthode à une gamme de zénith et d'énergie plus larges.

Le premier chapitre donne une introduction générale de la physique des rayons cosmiques. Les deux chapitres suivants décrivent respectivement la physique de gerbes atmospheriques et l'observatoire Pierre Auger. Le chapitre 4 donne un aperçu des importants résultats obtenus par la Collaboration Auger par rapport à la composition de la masse UHECRs. Le chapitre 5 décrit la méthode de *Smoothing* qui permet la mesure de la teneur en muons des gerbes en exploitant les différentes distributions de temps de muons et des signaux électromagnétiques dans les détecteurs de SD. L'évaluation de son fond physique et de sa précision est une partie de ce travail de thèse. Dans le chapitre 6, les propriétés de profil MPD sont discutées, afin de définir les gammes d'énergie primaire, d'angle zénithal et la distance du point d'impact exploitable par la méthode. Dans le chapitre 7, l'extension de la reconstruction MPD avec des détecteurs SD est étudiée. En particulier, nous montrerons que les deux principaux problèmes liés à l'extension de l'analyse, c'est -à-dire la contamination EM et les effets du détecteur, peuvent être résolus en exploitant à la fois le *Smoothing* et la déconvolution des signaux de muons de la réponse de la cuve. Dans le chapitre 8 la méthode proposée est appliquée aux données SD et les résultats obtenus sont discutés, ainsi que systématiques afférents.

Enfin, dans le chapitre 9 est décrite la partie de la thèse effectuée avec le groupe Auger á LPNHE Paris. En particulier, nous avons étudié la possibilité de reconstruire le profil MPD avec l'une des mises à jour proposé pour *Auger-Beyond2015*, la cuve segmentée (*Layered Surface Detector*).

CHAPTER 1

Ultra High Energy Cosmic Rays

The Earth's atmosphere is permanently exposed to a flux of ionized energetic particles and nuclei arriving from all directions, the so called cosmic rays. The understanding of origin, composition and energy spectrum of the ultra-high energy cosmic rays, i.e. cosmic rays with energies larger than 10^{18} eV is mandatory in Astroparticle Physics.

Cosmic rays have been discovered by Victor Hess in 1912, when he underwent a balloon campaign of measurements to study the ionization rate in the atmosphere and its origin [Hess (1912)].

Even if their first observation dates back one hundred years ago, the origin of these particles is still unknown and the mechanisms through which they are accelerated to such high energies are also unclear. Indeed, the strong decrease in flux with energy makes the study of cosmic rays of high energies challenging.

In this chapter the energy spectrum, the sources and the propagation of cosmic rays will be briefly described.

1.1 Energy spectrum

The cosmic rays energy spectrum has been measured by many experiments, which exploit different techniques and are located at various atmopehric depths depending on the energy region they wanted to study. The differential flux follows a power law $E^{-\gamma}$ and spans more than 12 orders of magnitude (Figure 1.1). The flux falls at a rate of about 3 orders of magnitude per energy decade, from about one particle per m^2 per second at around 100 GeV to one particle per km^2 per year above 10 EeV.

Fig. 1.1 shows the all-particle differential energy spectrum, i.e. number of particles per m^2 sr s GeV. At low energies, the spectral index γ is about 2.6-2.7 [Cronin (2009)]. At higher energies, three features can be observed in the spectrum:

- a steepening around $3 \cdot 10^{15}$ eV, referred to as the *knee*, described the spectral index changes from $\approx$ 2.7 to ≈ 3.0.
- a further steepening, around $5 \cdot 10^{17}$ eV, the *second knee*, where γ decreases to $\approx$ 3.2.
- a pronounced flattening, at around $3 \cdot 10^{18}$ eV, referred to as the *ankle*, where γ returns to $\approx$ 2.7.

These spectral characteristics imply significant changes in the properties of cosmic rays, which can be ascribed to a variation in the chemical composition and/or the location of the sources and/or a propagation effect.

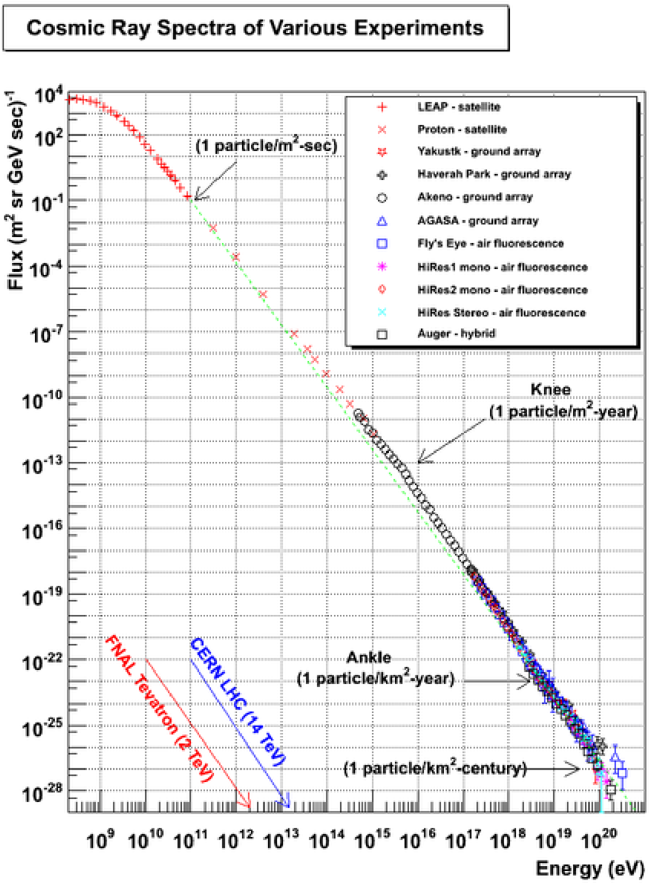

Figure 1.1: Differential energy spectrum of cosmic rays. Approximate integral fluxes are indicated: one particle per $m^2 - sec$ at $\sim$ 100 GeV, one particle per $m^2 - yr$ at the knee, one particle per $km^2 - yr$ at the ankle. The energies accessed by the most powerful accelerators are also shown [Cronin et al. (1997)].

1.1.1 The Ankle energy region

In the energy range between 10^{17} and 10^{19} eV the transition from galactic to extra-galactic cosmic rays is expected to occur.

As pointed out before, the ankle consists of a flattening of the spectrum to a spectral index close to 2.7. This flattening has been observed by several experiments. The energy spectrum derived by the HiRes, made of two fluorescence telescopes [Sokolsky and Thomson (2007)], Auger [Abraham et al. (2010)] and Telescope Array (TA) [Abu-Zayyad et al. (2012)], both hybrid instruments, is shown in Figure 1.2. Although systematic differences are visible, all three measurements show the spectral flattening at the ankle, as well as a flux suppression at the highest energies which will be discussed in the next Section. The HiRes found the break at energy $10^{18.65}$ eV, with a spectral index between the two breaks of 2.81 ± 0.03. The spectrum is consistent with various models and in particular with a pure proton composition one [Abbasi et al. (2014)]. The Auger

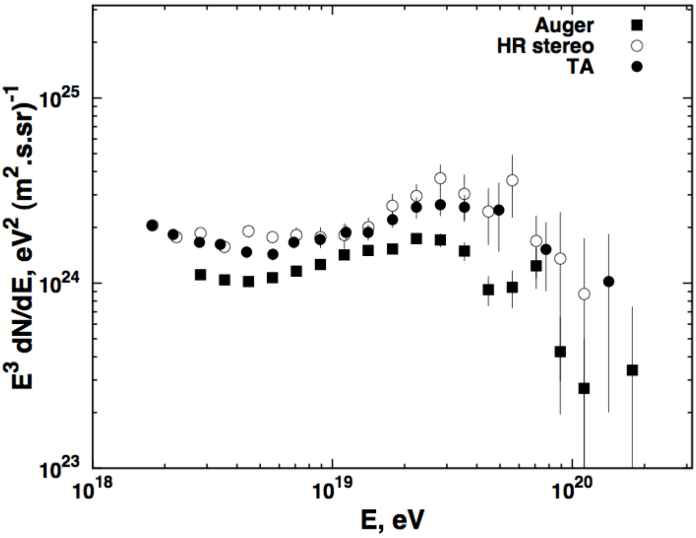

Figure 1.2: The cosmic ray spectrum for the highest energy region, as measured by HiRes, Auger and TA. The particle flux is multiplied by E^3 to show better the shape of the energy spectrum [Stanev (2012)]

spectrum has a slightly different shape. From $4 \cdot 10^{18}$ eV to $4 \cdot 10^{19}$ eV the slope of the spectrum is 2.68 ± 0.01. The Auger spectrum can be explained by several different models some of which include mixed chemical composition at acceleration in the sources. The fit to the spectrum measured by the TA experiment gives a slope between the breaks of 2.68 ± 0.04. Since the TA measurement is based on smaller statistics its results should be considered preliminary. All three spectra are consistent with each other within systematic uncertainties, due to the energy scale.

There are several models proposed to describe the ankle energy region.

For instance, the *ankle model* assumes that the ankle hosts the transition from galactic to extragalactic cosmic rays, which equally contribute to the flux in this region. The former is predicted to have iron-dominated composition while the latter is assumed to have proton-dominated composition with a flat generation spectrum $\propto E^{-2}$ valid for non-relativistic shock acceleration [Hillas (2006),De Marco & Stanev (2005)].

In the *dip model*, the transition is supposed to happen at lower energy, i.e. at $\approx 1 \cdot 10^{18}$ eV, while the ankle is interpreted as the spectral feature due to the electron-positron pair production by extragalactic protons interacting with the Cosmic Microwave Background Radiation (CMB) [Berezinsky (2007)]. Its observational confirmation would thus be in favor of a proton-dominated composition.

On the other hand, the *mixed composition model* assumes that the extragalactic cosmic rays have a mixed composition, with nuclear abundances similar to that of the galactic cosmic rays, and the ankle is interpreted as the galactic-extragalactic cosmic ray transition [Allard et. al (2007)].

These models are able to reproduce the high energy cosmic ray data quite well, although with a different source spectrum and a correspondingly different interpretation of the ankle (see Figure 1.3).

Disentangling the properties of the ankle to favour one of the models is complicated and cannot be done by the study of the sole spectrum. As described above, each model predicts a different composition and mass composition studies are thus crucial.

For example, the *ankle model* needs a heavy galactic component, and it is thus in contradiction with observations, since all data, including both HiRes and Auger, show proton or light nuclei composition at these energies.

The *dip model* predicts an almost pure iron composition at the second knee, and a proton composition above. This model is compatible with the results published by TA (see [Kido & Kalashev (2013)]).

The signature of the *mixed composition model* in terms of mass would be a change from iron primaries to a mixed composition of lighter nuclei. The model predicts an abundance of heavy elements of the order of 10% for energies above the Ankle, which is compatible with current observations from Auger (see Chapter 4).

1.1.2 End of the spectrum

As shown in Figure 1.2 the cosmic ray spectrum above $10^{19.3}$ eV is evidently suppressed.

The energy of the cutoff, i.e. energy at which the flux has lowered to half of its value, is $E_{1/2} = 4 \cdot 10^{19}$ eV as measured by Auger, with a spectral index above it of 4.2 ± 0.1. The same feature, although at a higher energies, $E_{1/2} = 5.6 \cdot 10^{19}$ eV, has been observed by HiRes and TA [Stanev (2012)]. The statistical significance of the cut-off is more than 5σ.

The suppression of the spectrum can be ascribed to two different scenario:

- propagation effect (the Greisen-Zatsepin-Kuzmin mechanism) [Greisen (1966),Zatsepin & Kuzmin (1966)];
- exhaustion of the sources;

or the combination of them.

Propagation scenario The GZK effect gives a theoretical upper limit on the energy of cosmic rays from distant sources, based on interactions between UHE particles and the photons of CMB.

Cosmic rays with energies above the threshold $E_{thr} = 5 \cdot 10^{19}$ eV see a CMB photon as a 300 MeV photon, and undergo photopion production via Δ resonance. Since CMB photons are everywhere, the universe will be partially opaque to UHECRs, limiting them to a mean free path of about 50 Mpc if they are above the threshold energy. As a result, extragalactic cosmic rays traveling over distances larger than 50 Mpc and with energies greater than this threshold should never be observed on Earth. This distance is also known as GZK horizon.

Source scenario As we will see in the next section, the maximum energy attainable at an accelerating source is given by:

$$E_{max} = ZeRB\beta \tag{1.1}$$

where Ze is the particle charge, R is the source size, B is strength of the local magnetic field and β is the shock velocity in terms of speed of light. The flux suppression may thus indicate the upper-limit of the power of the accelerator.

In order to disentangle these two scenario, the knowledge of the composition at the highest energies is of utmost importance. Indeed, by means of the energy spectrum

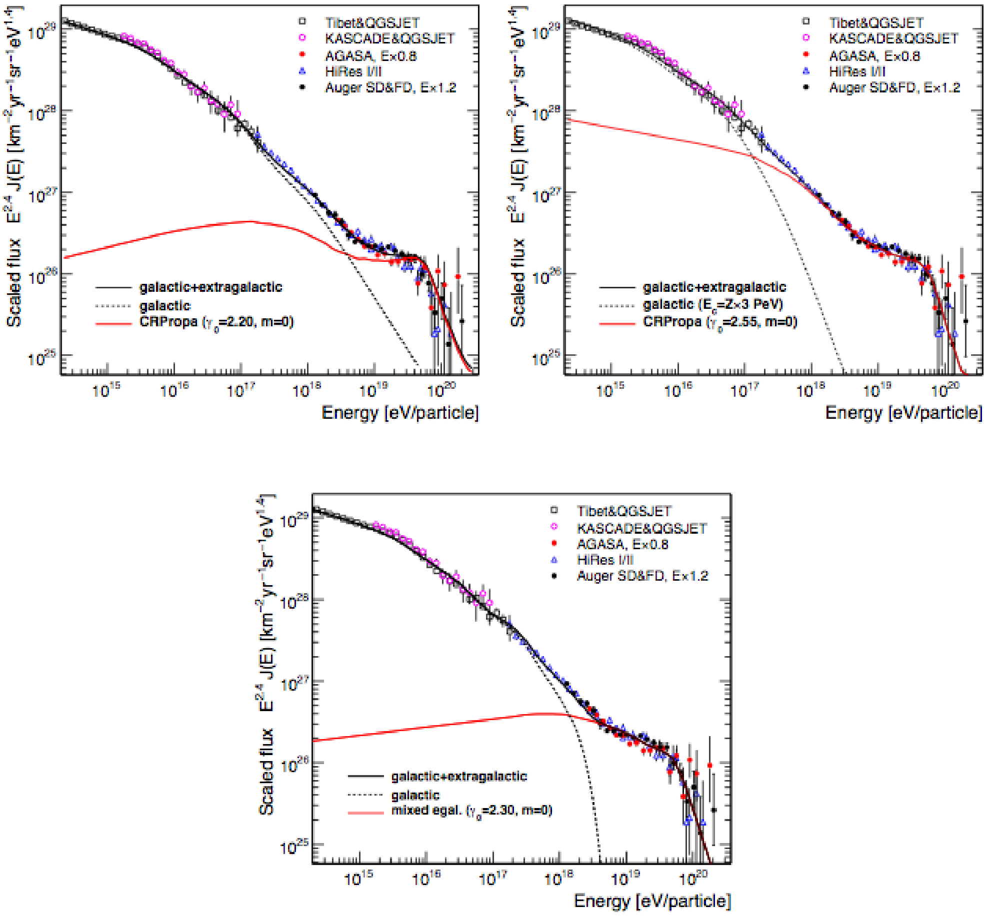

Figure 1.3: Models describing the transition between galactic and extragalactic cosmic ray component, together with data from several experiments. Ankle model (top left), dip model (top right) and mixed composition model (bottom). See [Unger (2008)] for details.

alone, it is not possible to distinguish between different scenarios, since there are too many unknowns, as for example the source distributions and evolution, the acceleration characteristics and the cosmic ray mass composition. This is clearly visible in Figure 1.3, where the spectra from different astrophysical models are compared to the spectrum.

The TA Collaboration finds their measurements at the highest end of the spectrum to be compatible with the GZK expectation, for a uniform distribution of sources that accelerate protons to energies well above the GZK threshold, as was also concluded by HiRes.

On the contrary, the data from the Pierre Auger Observatory indicate that above $10^{18.3}$ eV, UHECR primaries consist of a mixed composition, with the fraction of light nuclei becoming smaller with increasing energy. An interesting scenario was recently developed, trying to explain the Auger data [Aloisio et. al (2013)]. A very hard injection spectrum ($\gamma \leq 1.5 - 1.6$), such as in rapidly rotating neutron stars, and an enhanced Galactic component could give a very good fit to Auger data above 5 EeV. An ad-hoc component should however be considered for the lower energies, below 5 EeV. Therefore, the observed suppression of the energy spectrum mainly would stem from the source characteristics rather than being the imprint of particle propagation through the CMB.

However, current data are insufficient to conclude whether the observed feature is due to energy-loss during propagation, or to the reach of the maximum acceleration in the sources, or indeed to a combination of both source properties and propagation effects.

1.2 Sources

One of the most important challenge in the astroparticle field is the understanding of which kind of astrophysical objects accelerate particles at such high energies. On the theory side, several models have been proposed, which can be classified in two categories: *bottom-up* and *top-down*. We will briefly discuss both model types in the following sections.

1.2.1 Bottom-up models

These models are based on the existence of astrophysical objects ables to accelerate cosmic rays through electromagnetic fields. Two distinct accelerating mechanisms could occur: diffusive shock acceleration, based on Fermi mechanism, and one shot acceleration in very high electric field, which can be generated by rapidly rotating compact magnetized objects such as neutron stars. Both accelation types have to fit the power law spectrum and to provide the necessary power, taking into account energy losses during cosmic rays propagation.

The maximum energy attainable at a given source was postulated by Hillas [Hillas (1984)]: $E_{max} = ZeRB\beta$, as already indicated before. For ultra relativistic shocks the condition requires that the gyroradius is contained in the acceleration region, and it holds for both accelerating mechanisms.

Figure 1.4 depicts the acceleration capabilities of some astrophysical objects. A large magnetic field or a large acceleration region size are required to achieve a given maximum region.

For example, the candidates to accelerate protons up to 10^{20} eV are: neutron stars, gamma ray bursts, active galactic nuclei, radio galaxies and large-scale shocks due to merging clusters of galaxies. We will summarize briefly the characteristics of these objects.

Neutron stars In the case of compact objects, such as neutron stars or pulsars, Equation 1.1 becomes $E_{max} = \omega/cZB_s r_{ns}^2$ where ω is the pulsar angular velocity, B_s is the surface magnetic field and r_{ns} is the neutron star radius. Taking the values for the Crab pulsar: $B_s \sim 10^{12}G$, $r_{ns} \sim$ 10 km, $\omega \sim$ 200 Hz, a maximum energy $\sim 10^{18}$ eV is achieved.

Gamma ray bursts Gamma ray bursts are one of the most energetic events in the universe and they could be associated with the collapse of massive stars or with the merging of black holes or neutron stars. The observed gamma-rays are emitted by relativistic electrons via synchrotron radiation and inverse Compton scattering. However, the typical GRBs distance is too large (more than 100 Mpc) to account easily for the UHE-

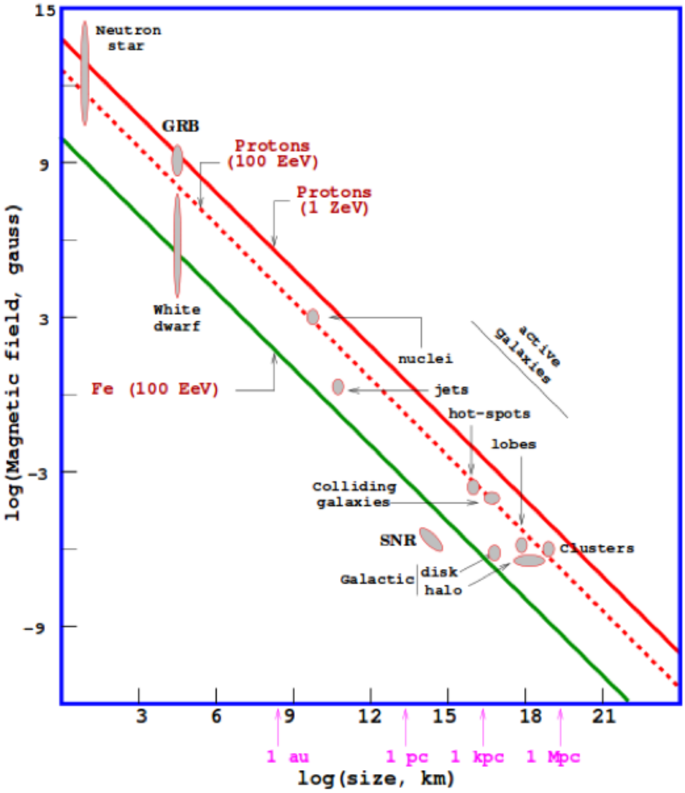

Figure 1.4: The Hillas plot illustrating the acceleration capabilities of some astrophysical objects. Accelerating candidates below the diagonal lines cannot reach the indicated energies. From Anchordoqui et al. (2002)

CRs flux.

Active Galactic Nuclei Active galactic nuclei are the most favored sources for cosmic rays at the highest energies. According to the standard model of AGN, acceleration may be due to the accretion of matter into the supermassive black hole ($M \sim 10^6 - 10^9 M_\odot$). Typical values for these objects are $R \sim 10^{-2}\ pc$ and $B \sim 5\ G$, which allow to accelerate protons up to 10^{20} eV.

However, large energy losses take place due to high field density, reducing the maximum energy achievable for protons and blocking the escape of heavy nuclei. Nevertheless, the acceleration can occur in AGN jets too, where particles are injected with higher Lorentz factors and the energy losses are less important.

Radio-galaxies hot spots Fanaroff-Riley II galaxies are the largest known dissipative objects in the universe. Jets from the central black holes, interacting with the intergalactic medium, make radio lobes and regions of intense synchrotron emission, the so called *hot spots*. While radio lobes exceed the galaxy dimension reaching hundreds of kpc, hot spots are limited to the observable region ($\sim 1\ pc$), and the typical magnetic field inside them is $B \sim 300\ \mu G$. The maximum energy which could be reached for protons is ap-

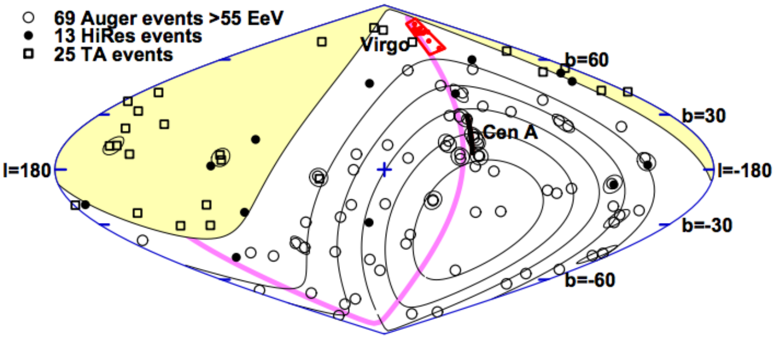

Figure 1.5: Arrival directions of the 69 Auger events, 13 HiRes events and the TA 25 events in galactic coordinates. The colored area shows the part of the Galaxy that Auger does not see. The six areas defined within the Auger field of view have equal exposures. The events that form a pair at angular distance less than 5° are circled[Stanev (2012)].

proximately $E_{max} \sim 5 \cdot 10^{20}$ eV.

Clusters of galaxies Galaxy clusters are huge objects ($\sim 500\ kpc$) with magnetic fields of the order of μG. They are thus candidate sites for high energy cosmic rays acceleration. However, due to the interaction of UHECRs with the CMB during the propagation inside them, the maximum energy reachable is at most 10^{19} EeV.

On the experimental side, searches for anisotropies in the arrival directions of UHECRs have been made in many experiments, both on large and small angular scales. Indeed, localized excesses at small angular scales at energies above 10 EeV are expected, because the bending of the trajectories of charged particles in the magnetic fields becomes smaller. It is also interesting to search for excesses at large angular scales, that could result either from the spreading of point-like sources by magnetic fields, or by the contribution of clustered sources.

In Figure 1.5, the arrival directions of the highest energy events of Auger, HiRes and TA are shown in galactic coordinates. In order to judge the possible direction of the sources by close-by arrival directions of groups of highest energy events, pairs of events at angular distance less than 5° from each other are searched. There are 11 such pairs in the Auger 69 events data set. Six such pairs are within 18 degrees of CenA. An isotropic Monte Carlo in the Auger field of view creates on the average 11 pairs, the same number as in data. There are three pairs consisting on HiRes and Auger events and one TA-Auger pair. There also two pairs consisting of TA events as shown in Figure 1.5.

The TA exposure is peaked in the northern hemisphere so the AGNs visible to TA are not the same as the ones visible to Auger, though there is some overlap. When the distribution of nearby AGNs is taken into account, and assuming equal AGN luminosities, the correlating fraction would be 44%, rather consistent with the updated correlation fraction from Auger. In the full TA SD data set, there are 11 correlating events out of 25, while the expected number of random coincidences is 5.9. The probability of this correlation to occur by chance with isotropic distribution of arrival directions is 0.02. More data are necessary to show whether this correlation is statistically significant or not.

1.2.2 Top-down models

An alternative to acceleration models is provided by the hypothetical existence of a new unstable or meta-stable super-massive particle, such as supersymmetric particles or topological defects.

The decay or annhihilation of this particle should produce a cascade of energetic photons, neutrinos, light leptons, and a small fraction of protons and neutrons.

Therefore, the footprint of these models consists in a photon domination of the spectrum at the highest energies. For a detailed review see [Bhattacharjee & Sigl (2000)].

Due to the Auger limits on photon and neutrino fluxes at ultra-high energies, this scenario is disfavored since it cannot explain a significant part of the observed flux [Letessier-Selvon (2013)].

1.3 Propagation

During their propagation from the sources to the Earth, cosmic rays are deflected by magnetic fields and interact with the background radiation fields.

As already suggested, processes which take place during cosmic rays propagation affect the energy spectrum measured on Earth.

The investigation of the magnetic fields in the universe and of the energy losses which cosmic rays could undergo in the outer space is therefore another important challenge of astroparticle physics.

1.3.1 Magnetic fields

The galactic magnetic field has a large scale structure and its strength is estimated by measuring the Faraday rotation of the radio emission of pulsars. The typical value of the field is few μG, approximately uniform over few kpc scales.

The magnetic field lines follow spiral arms. In Figure 1.6, the trajectories for nuclei with E/Z= 1 EeV and E/Z= 10 EeV are sketched.

For $E/Z \simeq 1$ EeV, nuclei are trapped by magnetic fields and follow helicoidal trajectories around field lines. On the contrary, for E/Z value above 10 EeV, the trajectory is not significantly affected by the magnetic field since the gyroradius for a particle of that energy is comparable to the traveled distance.

In this case the information of the incoming direction is preserved and the correlation with sources can in principle be established.

Assuming a constant magnetic field along the traveled distance *d*, the angular deflection is

$$d\theta(E,d) \simeq \frac{d}{r_L} \simeq= 0.52^\circ \cdot Z \cdot (\frac{E}{10^{20}eV})^{-1} \cdot (\frac{B}{10^{-9}G}) \cdot (\frac{d}{Mpc}) \qquad (1.2)$$

where $r_L \simeq E/(Z \cdot B_\perp)$ is the *gyroradius*. Therefore, for a proton of energy $\sim 10^{20}$ eV in a magnetic field $\sim \mu G$ on a distance $\sim kpc$, the deviation will be less than 1°.

In the case of extragalactic magnetic fields, whose typical values are of the order of nG, the angular deflection would be the same, given the large traveled distance (of the order of Mpc) and the fact that they are not constant.

Therefore, ultra-high energy cosmic rays are weakly deflected by galactic and extragalactic magnetic fields and they in principle point at the sources.

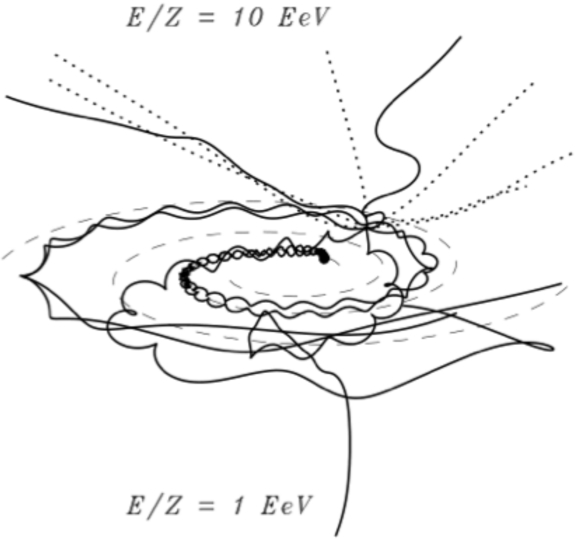

Figure 1.6: Examples of trajectories of nuclei with E/Z= 1 EeV (solid lines) and E/Z= 10 EeV (dotted lines) in the galactic magnetic field. Dashed lines indicate the spiral arms. BSS-S model from [Harari et al. (1999)].

1.3.2 Interaction with the background radiation fields

At the highest energies, cosmic rays interact with the cosmic microwave background (CMB) and the infrared background (IR).

As described before, Greisen, Zatsepin and Kuzmin predicted that the spectrum of high energy cosmic rays protons would show a cut-off at about $5 \cdot 10^{19}$ eV, due to the photopion production on CMB photons:

$$\begin{aligned} p + \gamma_{CMB} &\to p + \pi^0 \\ p + \gamma_{CMB} &\to n + \pi^+ \\ p + \gamma_{CMB} &\to p + e^+ + e^- \end{aligned} \tag{1.3}$$

These processes have a high cross-sections ($\sigma \sim 6 \cdot 10^{-28} cm^{-2}$) and the energy loss per interaction is about 20%, giving an attenuation length of a few tens of Mpc. Sources of the highest energy events must thus be within a sphere of about 50 Mpc, the so called *GZK horizon*.

The energy threshold for the pion production is

$$E_{thr} = \frac{m_\pi}{4E_\gamma}(2m_p + m_\pi) \simeq 10^{20} eV \tag{1.4}$$

while the energy threshold for the pair production is

$$E_{thr} = \frac{m_e(m_p + m_e)}{E_\gamma} \simeq 10^{17} eV \tag{1.5}$$

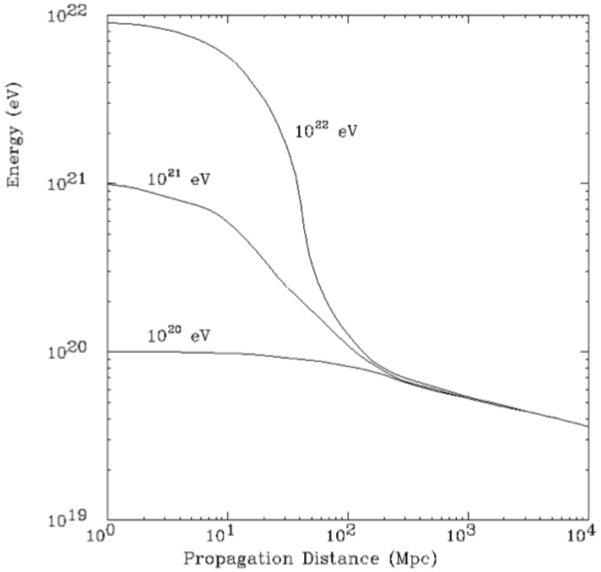

Figure 1.7: The energy of protons as a function of propagation distance. The different curves represent different initial energies at the source. [Cronin (2005)]

Figure 1.7 shows the theoretical prediction of proton energy as a function of propagation distance. Protons with energy greater than the GZK energy threshold lose part of the energy and after 100 Mpc reach energies of about 10^{20} eV, independently from their initial energy.

As described in Section 1.1.2, the interaction of ultra high energy cosmic rays with CMB could thus explain the suppression of the flux at the end of the energy spectrum, assuming that at those energies protons are the dominant component.

The GZK processes produce a flux of high energy neutrinos and photons, generated in the pion decays. Therefore, the eventual detection of cosmogenic neutrinos and photons flux could help the analysis of the UHECRs features and origin since it will allow to disentangle the propagation scenario from the source one, which assumes a decreasing of acceleration power at the sources.

Heavy nuclei of mass A interacts with CMB and IR during their propagation, undergoing photo-disintegration and pair production:

$$\begin{aligned} A + \gamma_{CMB,IR} &\rightarrow (A-1) + N \\ A + \gamma_{CMB,IR} &\rightarrow (A-2) + 2N \\ A + \gamma_{CMB,IR} &\rightarrow A + e^{+} + e^{-} \end{aligned} \tag{1.6}$$

where N is a nucleon.

The threshold energy for these reactions increases with A while the cross-section increases with Z^2. Therefore, the interaction length in the case of heavy nuclei will be smaller with respect to protons, but the cutoff energy will be greater.

In Figure 1.8 the expected distribution of distances for several nuclear species on the basis of a uniform source distribution is shown. It is notable that for distances greater

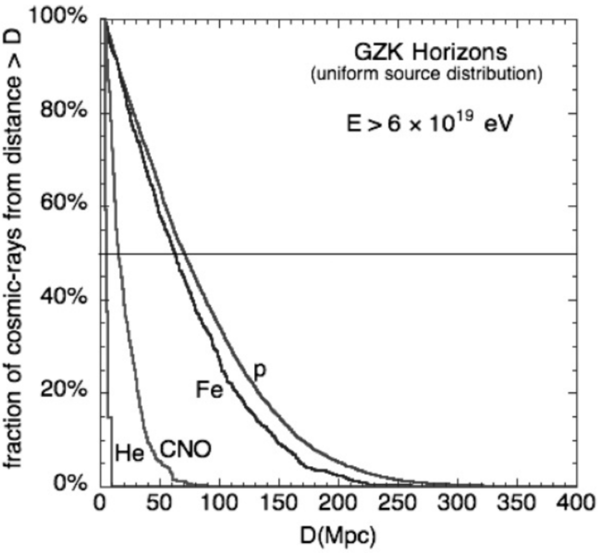

Figure 1.8: GZK horizons for protons and nuclei. [Cronin (2009)]

than 50 Mpc only proton and iron nuclei survive. Therefore, it is generally assumed a two components composition at these energies.

CHAPTER 2

Extensive Air Showers

As already described in Chapter 1, UHECRs properties cannot be determined from direct detection but must be inferred from the measurements of the secondary particles that the cosmic ray primary produces in the atmosphere. They are called *Extensive Air Showers* (EAS).

Indeed, above 100 TeV the primary flux is very small (less than 1 particle/m^2-year) and large detection areas are needed in order to collect enough particles in a reasonable time.

The indirect detection allows to reconstruct fairly well the energy and the arrival direction of cosmic rays. The primary mass is instead more difficult to determine, mostly at the highest energies.

However, measuring the cosmic ray composition at the highest energies is a mandatory task from the astrophysical point of view, since its knowledge could allow to separate the different scenarios of origin and propagation of cosmic rays.

Mass composition studies are also of the utmost importance for particle physics, as knowing the composition one can explore the hadronic interaction at ultra-high energies, inaccessible to present accelerator experiments.

Indeed, hadronic cross-sections are extrapolated from the current LHC data, and they are the most important source of systematic uncertainty in the mass composition studies. The latter can thus help to constrain hadronic interaction models and increase our knowledge in high energy particle physics.

In this chapter the EAS properties will be described, together with the two main EAS detection techniques.

2.1 Physics of EAS

When a cosmic ray enters the atmosphere, it interacts with the air molecules, generating a shower of secondary particles. These particles interact again inside the atmosphere generating new particles. The iteration of this process produces the EAS.

High energy cosmic rays produce air showers which reach the ground. For example, a 10^{19} eV vertical proton produces at sea level about $3 \cdot 10^{10}$ particles, with an extension at ground over a few km^2.

An EAS is formed by essentially three components: hadronic, muonic and electromagnetic. The hadronic component is generated at the top of the atmosphere, and gives rise to the other two components.

After the first interaction, whose depth depends on the composition and energy of the primary particle, the atmosphere acts like a calorimeter of variable density with a vertical thickness of more than 11 interaction lengths and 26 radiation lengths.

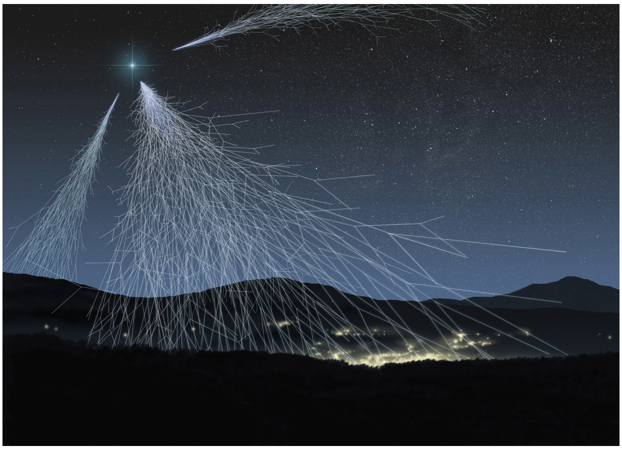

Figure 2.1: Artistic view of a cosmic ray shower. Credit: ASPERA.

At the beginning, the shower is mostly composed of pions and kaons. These particles interact with the atmospheric nuclei or decay, giving rise to more hadrons, muons, electrons, neutrinos and gamma rays.

The evolution of an extensive air shower is dominated by the electromagnetic component, which dissipates around 85% of the primary energy. The muonic component carries about 10% of the total energy, while the rest is associated to pions (4%) and, in smaller amount, to neutrinos and baryons.

2.1.1 Heitler's model of electromagnetic showers

A simplified model of the development of electromagnetic showers was suggested by Heitler [Heitler (1954)]. In Heitler's model, all particles have the same radiation length λ_r and after each interaction, two particles of the same energy are produced for any existing particle. It is assumed that at each step electrons emit radiation via bremsstrahlung while photons produce an e^+/e^- pair. Besides, cross-sections are assumed to be independent of energy and collision energy losses are ignored.

The radiation length λ_r is usually measured in g/cm^2: in the case of Air, it is $\lambda_r = 37\ g/cm^2$. The interaction step length d is therefore given by $d = \lambda_r ln2$. After n steps the number of particles will be $N_n = 2^n$, each of them with $E = E_0/N_n$, where E_0 is the primary energy. The development continues until the particle energy falls below the critical value E_c, i.e. the energy at which the rate of energy loss by electrons via bremsstrahlung is equal to the rate of energy loss by ionization. In air, $E_c = 80\ MeV$. At this point the maximum development is reached, and from then on particles interact with atmosphere losing energy until they are absorbed.

Even if the model is highly simplified, it correctly reproduces three properties of electromagnetic cascades:

- the number of particles at the maximum of the cascade is proportional to the primary energy

$$N_{max} = E_0/E_c \tag{2.1}$$

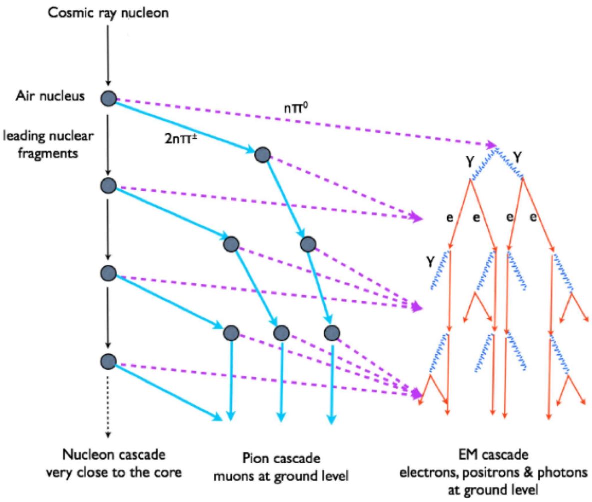

Figure 2.2: Schematic evolution of an hadronic cascade. [Letessier-Selvon & Stanev (2011)]

- the maximum position (along the shower axis) is logarithmic with energy

$$X_{max} = X_0 + \lambda_r log_{10}(E_0/E_c) \tag{2.2}$$

  where X_0 is the first interaction point.

- the evolution rate of X_{max} with the logarithm of the energy, the so-called *elongation rate*, defined as

$$D_{10} = \frac{dX_{max}}{dlog_{10}E_0} = 2.3 \cdot \lambda_r \tag{2.3}$$

  is given by λ_r. The elongation rate is about $85\ g/cm^2$ in air.

Extensive simulations of electromagnetic cascades confirm qualitatively these properties, even if the particle number at maximum and the ratio of electrons to photons are overestimated by the model.

2.1.2 Hadronic showers

Heitler's model can be adapted to describe hadronic showers [Matthews (2005), Stanev (2010)]. As indicated before, we can consider an EAS as the sum of three components: hadronic (nucleons, mesons), muonic and electromagnetic.

The hadronic cascade feeds the muonic and electromagnetic one, and a sketch of the evolution of an hadronic cascade is shown in Figure 2.2.

For the hadronic shower development, the relevant parameter is the hadronic interaction length λ_I.

At each step of thickness $d = \lambda_I ln2$, $2N_\pi$ charged pions and N_π neutral pions are produced. While π^0s decay immediately due to the very small decay length, $\pi^\pm$s interact further, generating neutral and charged pions with smaller energy, until the critical

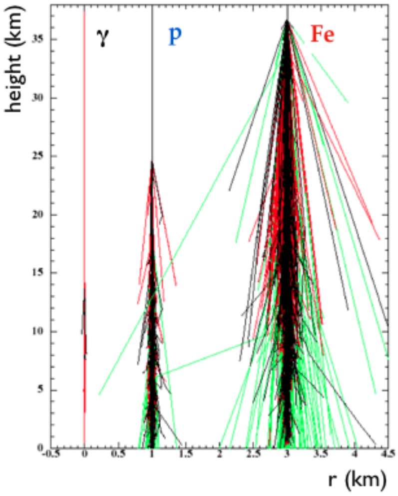

Figure 2.3: The shower development of vertical showers generated by different primaries.

energy is attained, where they decay rather than interact ($E_c = 20\ GeV$ in air). Then, they will decay in muons.

Therefore, the longer it takes for charged pions to reach the critical energy, the larger will be the electromagnetic component. Consequently, deep showers will have fewer muons at ground while primaries with higher cross sections, i.e. higher mass, will have a larger muon to electron ratio at ground.

The number of muons in the shower is correlated to the number of charged pions. By assuming that all pions decay in muons when they reach the critical energy, we have

$$lnN_\mu = lnN_{\pi^\pm} = \frac{2}{3}N_\pi n_c = \beta ln(\frac{E_0}{E_c}) \tag{2.4}$$

where $n_c = ln(E_0/E_c)/ln3N_\pi$ is the number of steps needed for the pions to reach E_c. Given $\beta = ln2N_\pi/ln3N_\pi$ (β=0.85 for N_π=5)

$$N_\mu = (\frac{E_0}{E_c})^\beta \tag{2.5}$$

Unlike the electron number, the muon one does not grow linearly with the primary energy, but at a slower rate. The value β depends on the average pion multiplicity used and on the inelasticity of the hadronic interactions.

The determination of the maximum is more complicated in the case of hadronic cascades. However, it is possible to treat an hadronic shower generated by a nucleus of mass A like the superposition of the showers produced by A nucleons, each of them with energy E_0/A (*superposition model*).

As a first approximation, it is reasonable to consider nucleons independently, since their binding energy is much smaller than the primary energy.

As a result, one can directly see that:

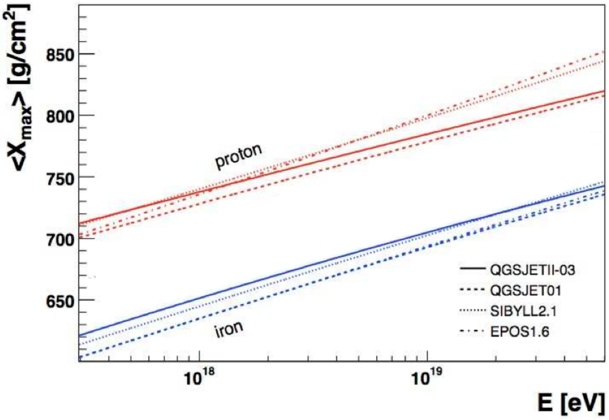

Figure 2.4: Evolution of X_{max} as a function of energy for iron and proton induced air showers. Shown here are the results of detailed simulation performed by the Auger collaboration using various interaction models.[Letessier-Selvon & Stanev (2011)]

- showers from heavy nuclei will develop higher in atmosphere (see Figure 2.3).

$$X^A_{max} = X^p_{max} - \lambda_r lnA \tag{2.6}$$

- showers from heavy nuclei will have a larger number of muons at ground

$$N^A_\mu = N^p_\mu A^{1-\beta} \tag{2.7}$$

- the evolution of the primary cross-section with energy is the same for protons and heavier nuclei. Therefore protons and irons showers will have similar elongation rates (see Figure 2.4).
- the shower-to-shower fluctuations of X_{max} position are smaller for heavy nuclei than for light ones.

All above properties have been validated by simulations and all interaction models share those basic principles. The offset in X_{max} from iron to proton showers is more than 100 g/cm^2, and iron showers have 1.5 the muon content of proton showers. The reproduction of these trends is of particular importance in the attempt to relate experimentally measured quantities to mass composition.

2.2 EAS Simulations

The simulation of EAS is performed with CORSIKA (COsmic Ray SImulations for KAscade), a physics computer software which may be used up to and beyond the highest energies of 100 EeV [Heck (1998)].

The most important uncertainties in simulations arise from modeling of high-energy hadronic interactions:

- The inelastic hadron-air cross sections;

- The energies occurring in EAS may extend far above the energies available in man-made accelerators, and when extrapolating towards higher energies one has to rely on theoretical guidelines;
- In collider experiments which are used to adjust the interaction models the very forward particles are not accessible, but just those particles carry most of the hadronic energy, and in the EAS development they transport a large energy fraction down into the atmosphere.

CORSIKA is coupled alternatively with 6 high-energy hadronic interaction codes (DPMJET, HDPM, neXus, QGSJET, SIBYLL, VENUS). Currently the uncertainty in the prediction of shower observables for different primary particles and energies is dominated by differences between hadronic interaction models.

The Large Hadron Collider (LHC) at the CERN laboratory allows to access, for the first time, the energy region above the knee in the laboratory. The LHC data can thus be used to test Monte Carlo generators and these new constraints will help to reduce the uncertainties in air shower predictions. The two high energy models which were updated to take into account LHC data at 7 TeV are: QGSJetII-03 [Ostapchenko (2006)] changed into QGSJetII-04 [Ostapchenko (2011)] and EPOS-1.99 [Pierog & Werner (2009)] replaced by EPOS-LHC.

QGSJetII is based on quark-gluon string model while EPOS is based on parton and hydrodynamical models. See [Ostapchenko (2011)] and [Pierog & Werner (2009)] respectively for a detailed review.

The updated model versions are characterized by some technical improvements and some parameters were changed to reproduce TOTEM [Csorgo et al. (2012)] cross sections [Pierog (2013)].

2.3 The muon component at ground

The muon content of air showers contains information about the primary mass and also about high energy interactions. For this reason, air shower muons have been studied in depth exploiting CORSIKA air showers.

As seen before, the number of muons at ground increases with the mass (Equation 2.7). and with the primary energy, following approximately a power law:

$$N_\mu \propto E^\beta \tag{2.8}$$

where $\beta \sim 0.88$ for proton and iron primaries, and $\beta \sim 1.07$ for photon showers (see Figure 2.5-left).

The ratio of muon numbers is almost constant with energy and it is equal to

$$\frac{N_\mu(Fe)}{N_\mu(p)} \simeq 1.5 \simeq const \tag{2.9}$$

Besides, due to the $cos\theta$ dependence, the number of muons decreases with the zenith angle, as it is visible in Figure 2.5 (right) for three different zenith angle values and in the case of proton showers.

The number of muons at ground depends also on the distance from the shower core, i.e. the impact point of the shower axis at ground. Generally proton and iron showers have a similar muon lateral distribution, while photons are characterized by a steeper one, mostly at low zenith angle.

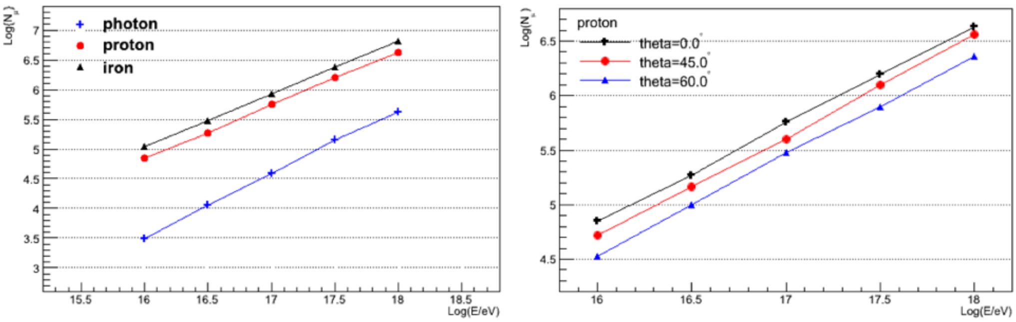

Figure 2.5: Left) The number of muons in different showers as a function of energy [Erfani et al. (2013)]. Right) The number of muons in proton showers as a function of energy for different incident angles. QGSJetII-03 simulations [Erfani et al. (2014)].

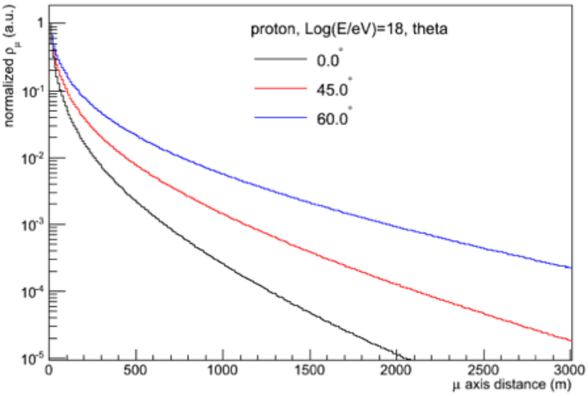

Figure 2.6: Lateral distribution for protons showers with $E = 10^{18}$ eV, at different zenith angles. QGSJetII-03 simulations [Erfani et al. (2014)].

Figure 2.6 shows the lateral distribution for proton showers arriving at ground with $\theta = 0°, 45°, 60°$. As the zenith angle increases, the LDF becomes flatter. Indeed, muons from vertical showers are produced closer to the ground and they are concentrated over a smaller area around the core due to their limited angular distribution. On the contrary, muons arriving farther from the core are mostly produced higher above the ground because those produced at lower altitudes cannot land at larger distances from the core.

Arrival times of muons at ground have also been studied, being fundamental for the estimation of the muon production depth that will be described later. The arrival times, estimated in the shower plane (the plane transverse to the shower axis), are similar for the different primaries and zenith angles. The distributions for hadronic showers are very similar to each other, and most of the muons arrive at ground within few microseconds.

If the arrival time of first muons as function of distance is studied, differences between primaries arise, as it is visible in Figure 2.7 (left). In particular, the first muons arrive later for larger distances and the delay (time delay as a function of distance) is

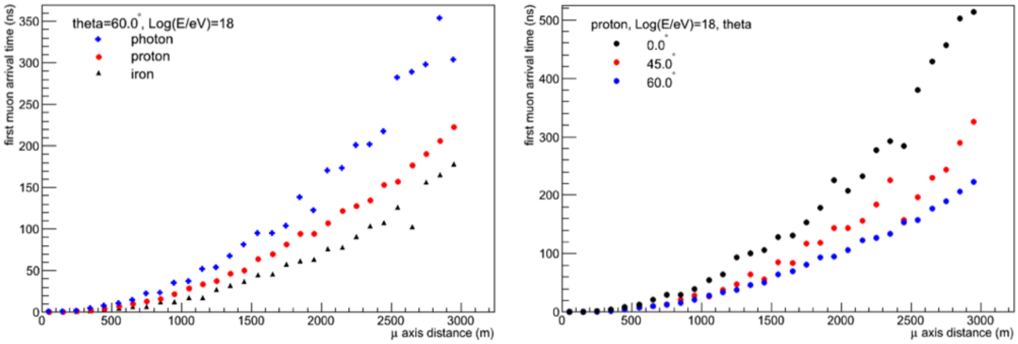

Figure 2.7: Left) Arrival time of first muon as a function of distance from the core for different primaries with $E = 10^{18}$ eV and $\theta = 60°$ eV. Right) Arrival time of first muon as a function of distance for proton showers with $E = 10^{18}$ eV and $\theta = 0, 45, 60°$. QGSJetII-03 simulations [Erfani et al. (2014)].

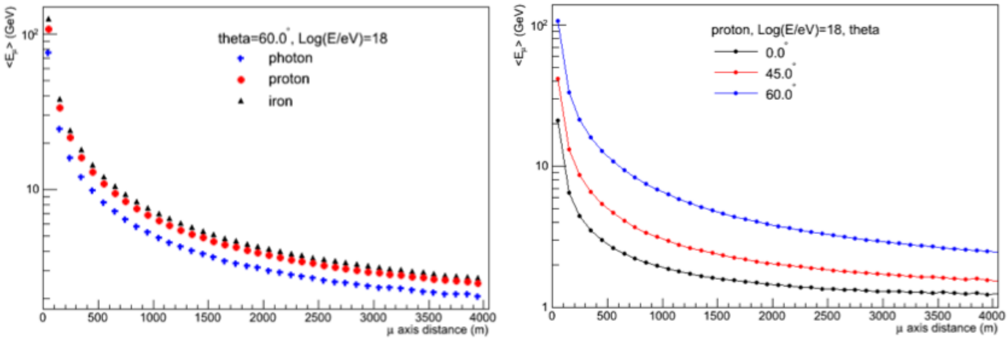

Figure 2.8: Mean muon energy as a function of distance from the core for different primaries with $E = 10^{18}$ eV and $\theta = 60°$. Right) Mean muon energy as a function of distance for proton showers with $E = 10^{18}$ eV and $\theta = 0, 45, 60°$. QGSJetII-03 simulations [Erfani et al. (2014)].

larger for proton showers than for iron ones. This effect is expected for geometrical and sampling reasons (far from the core the muon density is smaller) and is larger for proton showers because the latter develop deeper in atmosphere. Besides, the effect is larger at low zenith angles, and this happens for all primaries.

Finally, the muon energy distribution at ground has also been investigated. The mean muon energy is similar for hadronic showers (being slightly greater for iron primaries), and decreases as a function of distance from the core as it is visible in Figure 2.8. The mean energy depends on the zenith angle too: inclined events are characterized by more energetic muons at ground with respect to vertical events. Indeed, in the case of inclined showers low energy muons decay before reaching ground. This effect is the same for all primaries.

It is thus straightforward that the characteristics of air shower muons depend on primary mass, zenith angle, energy and distance from the core. As a consequence, when muons are sampled with ground detectors, all these dependences have to be taken into

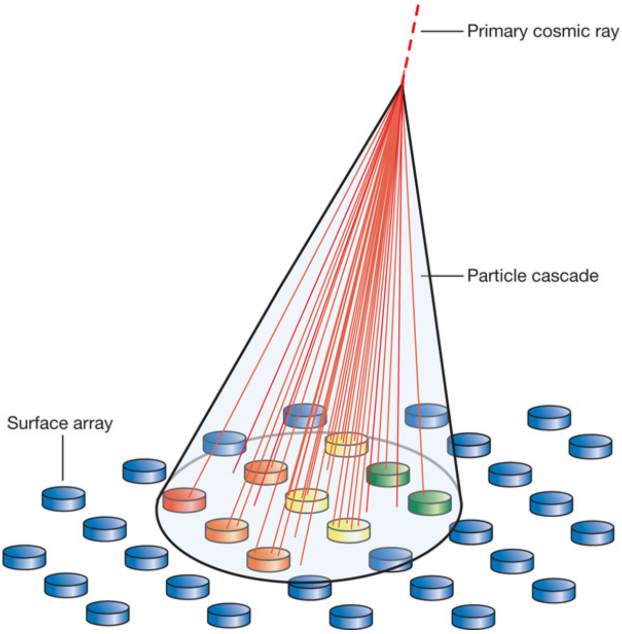

Figure 2.9: Sketch of EAS detection with ground array [Bauleo & Martino (2009)].

account with care.

2.4 EAS detection techniques

The main detection methods exploited to study EAS are the sampling of particles at ground with detector arrays and the measurement of the light emitted by shower particles with atmospheric light detectors.

2.4.1 Ground arrays

The most used technique to study UHECRs physics is to build an array of ground detectors (scintillators, water Cherenkov tanks, etc.) spread over a large area, in order to sample the shower front.

Depending on the energy range under study, different size and sampling distances can be chosen.

The study of UHECR needs arrays of thousands km^2 and spacing of about 1 km, while at lower energies the array size can be smaller and with a reduced spacing in order to sample enough particles.

The detectors of the array sample the shower at one single atmospheric depth and measures the particles which cross the detectors as a function of time. The altitude of the ground detector is chosen as close as possible to the maximum longitudinal development of the showers in the range of energy under study. In particular the study of UHECR requires ground arrays located between 500 m and 1500 m above the sea level.

The reconstruction of the primary particle properties is based on timing and on the distribution of particle densities as a function of the lateral distance to the shower axis.

In particular, through ground detectors we can derive:

- **shower geometry**: from the positions of the different triggered detectors and the signals recorded in them, it is possible to estimate the shower core location, i.e. the intersection point of the shower axis with the ground level. Then, through the analysis of the arrival time of the shower front in the different detectors, the shower axis is reconstructed, and hence the arrival direction of the cosmic ray. The accuracy in the shower geometry reconstruction depends on the time resolution of detectors and on the detector spacing.

- **primary energy**: the energy of the cosmic ray can be estimated by measuring the particles distribution at ground and comparing it with MC simulations. In particular, the detector positions are projected onto the plane transverse to the shower axis and a *Lateral Distribution Fuction* is adjusted to the measured signals. Once the LDF is measured, the signal at an optimal distance r_{opt} [Hillas (1984)] can be related, through Monte Carlo simulations, to the primary energy. The r_{opt} depends on the energy range and the array spacing and it is chosen as the distance at which the sum of the shower-to-shower fluctuations and of the statistical fluctuations from particle counting is minimum.

- **primary mass**: ground arrays do not have direct access to the position of X_{max}, which is related to the primary mass. However, the muon component at ground is a mass-sensitive observable too and it can be measured directly, by means of buried detectors, or indirectly, by processing the recorded signals in the detectors with appropriate algorithms (see Chapters 4 and 5).

2.4.2 Atmospheric light detectors

The charged particle component of air showers produces Cherenkov light and excites the nitrogen molecules of the atmosphere, which de-excite by emitting fluorescence light.

While the Cherenkov light is strongly beamed along the shower axis, the fluorescence light is emitted isotropically and hence can be detected away from the shower axis.

The Cherenkov light intensity is proportional to the primary energy, while the Cherenkov light lateral distribution is sensitive to primary mass. Indeed, the slope of the lateral distribution can be used to estimate X_{max} [Fowler et al. (2001)]. However, simulations have shown that only near the core, i.e. at distances smaller than 150 m, the slope can be related to the shower maximum. Therefore, the consequently small spacing required within detectors make Cherenkov light detectors unsuitable to study cosmic rays with $E > 10^{17}$ eV.

The fluorescence efficiency of photons, that is the ratio of the energy emitted in fluorescence by the excited gas to the energy deposited by the charged particles, is very low, of the order of $5 \cdot 10^{-5}$. Only above $\sim 10^{18}$ eV, the enormous number of particles allows this light to be detected; this has contributed to the decline of Cherenkov telescopes at the highest energies.

The fluorescence detection technique exploits the atmosphere as a huge scintillator detector. While crossing the atmosphere, shower particles excite the nitrogen molecules, which in turn emit photons isotropically in the spectral band between 300 and 420 nm.

The fluorescence yield is about 4 photons per electron per meter at ground level pressure. The fluorescence light can thus be measured only during clear moonless nights, using square-meter scale telescopes and sensitive UV detectors. In these conditions, the UV emission from UHECR showers can be observed at distances up to 20 km from the

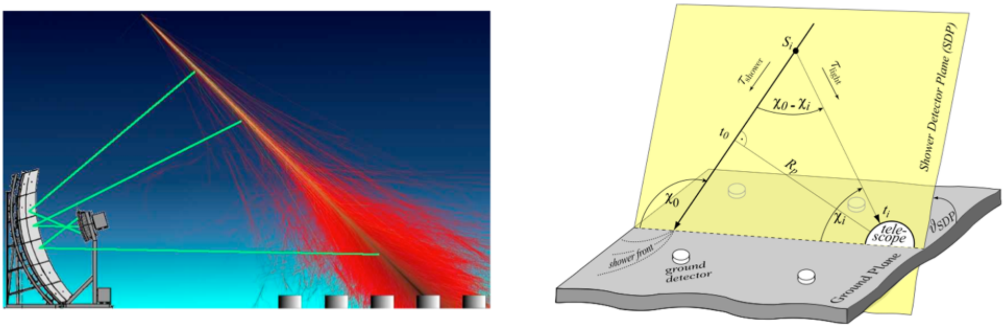

Figure 2.10: Sketch of the detection principle of a fluorescence detector. Credit: Auger Collaboration (left). Geometry reconstruction of the detection of an air shower by a fluorescence detector (right). [Kuempel et al. (2008)]

shower axis. Therefore, despite the low duty cycle, this technique is a very attractive alternative to ground arrays.

Figure 2.10 (left) depicts the detection principle of a fluorescence detector. Fluorescence photons arrive to the telescopes following direct line, except if they are scattered, from their sources. The collected light gives a measurement of the longitudinal development of the electromagnetic cascade.

However, in order to estimate the position of X_{max} and the primary energy, a number of corrections has to be done, in order to account for the scattering and the absorption of the fluorescence light. Moreover, it is necessary to continuously monitor the atmosphere and its optical quality, and to evaluate the Cherenkov contamination.

The shower geometry as viewed from a fluorescence telescope is shown in Figure 2.10 (right). It is given by the shower/detector plane (SDP), the minimum distance between the shower axis and the telescope R_p, the time t_0 along the shower axis at R_p and the angle within SDP between the shower axis and the ground level, χ_0.

The geometry reconstruction is done in two steps. First, the SDP is determined. Second, the arrival time of the signal in each pixel in the direction of SDP is used to determine χ_0, R_p and t_0 [Kuempel et al. (2008)].

The characteristic parameters which can be measured with the fluorescence technique are:

- **primary arrival direction (zenith and azimuth angle)**: the measurement is performed with high accuracy if two or more telescopes observe the shower.

- **primary energy**: once the geometry is determined, the energy of the incident cosmic ray is estimated by integrating the measured longitudinal profile. In the energy estimation, the *missing energy* due to the energy transported by neutral particles, hadrons interacting with nuclei and penetrating muons is also taken into account.

- **primary mass**: the maximum of the measured longitudinal profile, X_{max}, is directly measured by the fluorescence telescopes. Although being directly related to the primary mass, as discussed in section 2.1.2, the separation of hadronic primaries can be done using statistical methods, since the intrinsic fluctuations of the parameters do not allow to perform mass composition studies on a shower by shower basis.

2.4.3 UHECR detectors

Before the construction of the Pierre Auger Observatory, the largest ground array was AGASA (Akeno Giant Air- Shower Array), located in Japan. It was composed by 111 scintillators for the electromagnetic component detection, positioned on a 100 km^2 area, and by 27 scintillators for muon detection, having sizes from $2.4\ m^2$ to $10\ m^2$.

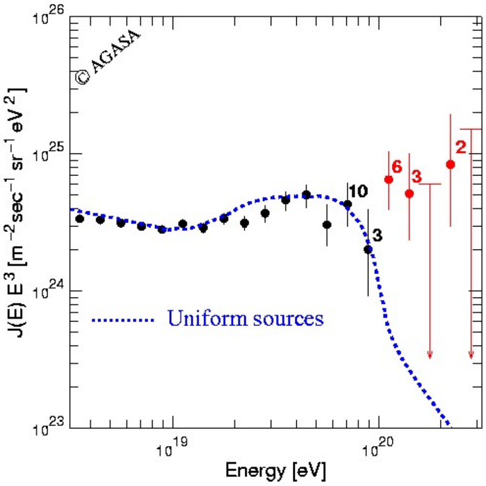

Figure 2.11: The energy spectrum measured by AGASA collaboration. Numbers attached to points show the number of events in each energy bin. The dashed curve represents the spectrum expected for extragalactic sources distributed unifomly in the Universe, taking into account the energy determination error. Credit: AGASA collaboration.

AGASA has been operating from 1990 to 2004. It measured the energy spectrum of cosmic rays up to 10^{20} eV. As shown in Fig. 2.11, no flux suppression was seen at the highest energies.

As regarding fluorescence detectors, after the successful experience of Fly's Eye [Baltrusaitis (1985)], the HiRes observatory [Abbasi et al. (2005)] was built, composed of two air fluorescence detector sites separated by 12.6 km. The observatory was located in Utah (USA), and was completed in 1999. Even if the two telescopes could trigger and reconstruct events independently, the observatory was designed to operate stereoscopically. In stereo mode, HiRes reconstructed events with high angular resolution (about $0.4°$). Unlike AGASA, the energy spectrum measured by HiRes showed a suppression in the cosmic ray flux above 10^{19} eV, although with low significance.

The need to confirm or disprove the existence of a suppression of the cosmic ray flux was one of the reasons to conceive the Pierre Auger Observatory, which is the largest Cosmic Rays Observatory ever built. Auger is the first large UHECRs array to use both ground and fluorescence detectors for the measurement of EAS.

By combining measurements done independently by the two type of detectors, systematic errors are reduced, and the small duty cycle of fluorescence telescopes can be compensated by the surface detector.

Another hybrid experiment currently underway is Telescope Array (TA), the largest CR observatory in the northern emisphere, located in the former HiRes site in Utah (USA). It is composed by 607 scintillators distributed over an area of 762 km^2 and by 3 fluorescence detectors. The surface array reaches full efficiency at $10^{18.7}$ eV for showers with zenith angle less than $45°$ [Nonaka et. al (2009)].

Most informations about the UHECR physics are currently obtained by Auger and TA Collaborations. The two Collaborations are working together, in a joint effort to understand the different systematics affecting the results and to reach a common view of the UHECR spectrum, composition and anisotropy.

CHAPTER 3

The Pierre Auger Observatory

The Pierre Auger Observatory is the largest operating cosmic ray observatory ever built. The main goal of the observatory is to answer the unsolved questions about UHECR physics $E > 10^{18}$ eV), as discussed in Chapter 1.

The Observatory is located in Argentina near the town of Malargue ($\sim 69°$ W, $\sim 35°$ S, 1300-1400 m a.s.l.), in the Pampa Amarilla region, and it is composed by two types of detectors: a surface array of water Cherenkov Detectors (WCD), to which we refer from now on with SD, and fluorescence detectors (FD). The use of two complementary detection techniques make it an hybrid experiment.

The data taking started at the beginning of 2004 even if the completion of the array was reached in 2008.

More recently, new detectors were added to the Observatory, in order to extend the energy range down to about 10^{17} eV. The extensions include an infill surface array with 750 m spacing [Varela (2013)], with muon detection capabilities (AMIGA), and three additional fluorescence telescopes with a more elevated field of view (HEAT). The 750 m infill array (covering about 24 km^2) and the new telescopes are now operational. Their aim is the measurement of cosmic rays from below the second knee of the spectrum up to the ankle, where data from the enhancement overlap those from the main observatory. For further details see [Varela (2013)].

In this chapter we will describe the characteristics of the surface and the fluorescence detectors and we will discuss the shower observables which can be measured by them. We will focus on the standard array of Auger, since the topic addressed by the present thesis is the measurement of UHECR mass composition.

3.1 Fluorescence Detector

The fluorescence detector is composed of 24 telescopes placed at 4 different locations in groups of 6. The FD observes the atmosphere above the surface detector, allowing for a hybrid detection of EAS. Each telescope has a field of view of 30° x 30° in elevation and azimuth. This allows full efficiency in detecting events with energy above 10^{19} eV.

In each telescope the optical system is composed by an UV filter selecting the fluorescence light (300-400 nm), an aperture and corrector ring, and a 3.6 m diameter spherical mirror illuminating a 20x22 pixels camera composed by 440 photomultipliers. Each PMT has a sky coverage close to $1.5°$. The ring maintains a large aperture while it reduces spherical aberrations and eliminates coma ones.

A schematic view of the Auger fluorescence detector is shown in Figure 3.3.

The FD duty cycle is rather low, about 15%, since observation periods are limited to clear nights with a limited moon light contamination.

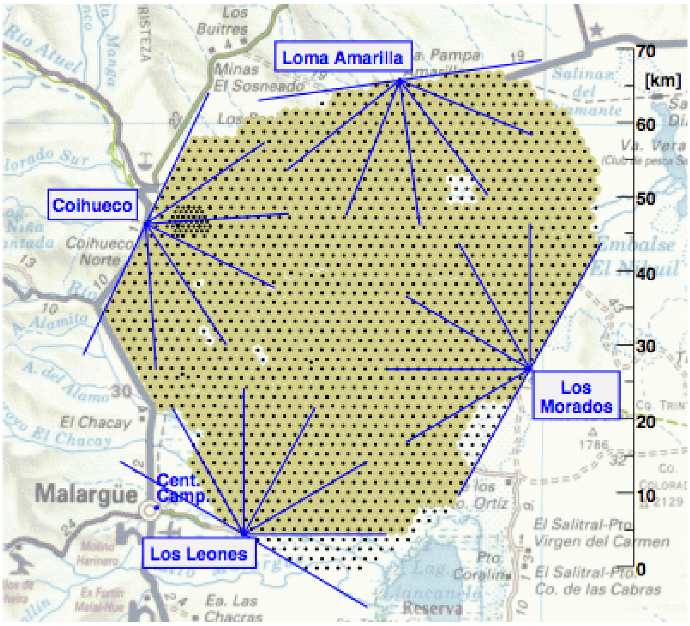

Figure 3.1: The Pierre Auger Observatory. Each black dot represents a WCD of the SD, while blue lines represent the field of view of the fluorescence telescopes positioned at four different locations.

The calibration of the telescopes and the monitoring of the atmosphere conditions are crucial for the determination of the shower parameters. Therefore, an accurate characterization of the aerosol content, clouds and suspended dust and smoke is needed. In this context, many devices and methodologies have been developed in order to study the atmosphere above the observatory [Abreu et al. (2012)].

3.1.1 FD Calibration

There are two types of calibration which are performed on the fluorescence detector: the absolute calibration and the relative one.

The *drum calibration* is designed to provide an end to end calibration of the FD using a diffuse light source. The latter consists of 2 UV LEDs (375 nm), and illuminates each PMT in the camera with a known intensity. This allows to transform the integrated electronic signal to the number of photons collected by every single pixel.

The relative calibration is formed by three routines, calA, calB and calC, running on a nightly base with the aim of monitoring the response and stability of the detectors. Light sources are mounted at each FD buildings, and light is distributed through optical fibers to different sections of each telescopes: the center of the mirror, the edges of the PMT camera and the inner side of the shutters. The total charge collected by each PMT is then compared to that obtained in the absolute calibration procedure.

Finally, a cross-check of the calibration procedures is done by exploiting the Central Laser Facility (CLF), deployed at the center of the SD array [Fick et al. (2006)]. The distance of the telescope sites from CLF ranges from 26 km to 39 km. The CLF sends

Figure 3.2: The Auger fluorescence detector sited at Los Leones. Two of the six bays that contain the telescopes are visible.

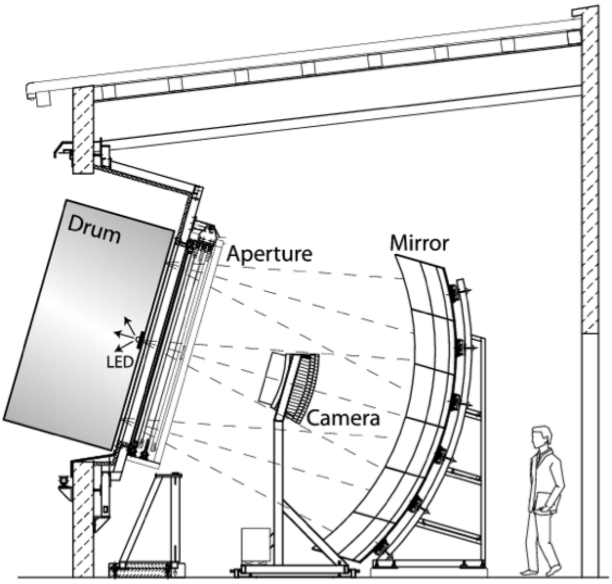

Figure 3.3: The FD optical system.

laser shots of known energy and direction in the atmosphere: the light from thise shots scatters in the air and a fraction of it is collected by fluorescence detectors. The signal produced is similar to the one relative to 10^{20} eV showers. The observed difference between the reconstructed energy and the laser one is 10-15%, consistent with the uncertainties in the absolute calibration and in the knowledge of atmosphere conditions.

3.1.2 FD Trigger

An FD telescope sees a cosmic ray as a straight track in the 20x22 pixel matrix. An hardware trigger system recognizes these tracks by means of a pattern recognition algorithm. The trigger logic has three levels and it is optimized to reach maximum efficiency at energy above 10^{19} eV.

The first level trigger (FLT) operates at the level of each single pixel. A threshold is chosen in order to keep the event rate close to 100 Hz. The requirement is that the sum of the last 10 bins in the PMT trace be above the threshold value.

The second level trigger (SLT) identifies track segments and shorter tracks. In particular, SLT searches for 5 adjacent pixels, with at most one of the them below the threshold value. This requirement allows to include events detected with at most one bad pixel. The SLT event rate is close to 0.1 Hz.

Finally, a third level trigger (TLT) is performed: process loops through all SLT events, rejecting tracks of wrong time order, created by noise, and merges track segments by software. The event rate is reduced by an order of magnitude after this process.

3.1.3 Geometric reconstruction with the FD

The geometry of the event is completely determined by three parameters: the impact parameter R_p, i.e. the distance of the closest approach to FD, the time t_0 at which this distance is reached, and the angle χ_0 between the shower axis and the horizontal vector (see Figure 2.10).

In order to reconstruct the arrival direction, it is necessary to determine the Shower Detector Plane (SDP), which is defined as the best fit to the pattern of triggered pixels in the fluorescence detector camera. Next, the timing information of the pixels is used to reconstruct the shower axis.

The light at the *i*th pixel is detected at the time t_i determined by

$$t_i = t_0 + \frac{R_p}{c} tan[\frac{\chi_0 - \chi_i}{2}] \tag{3.1}$$

where χ_i is the direction of the *i*th pixel on the SDP. This formula assumes istantaneous emission of the fluorescence light and straight line propagation with vacuum speed of light. A more realistic treatment of the emission and propagation of the fluorescence light on the geometry reconstruction has been discussed in [Kuempel et al. (2008)].

The determination of the shower arrival direction can be greatly improved if the event is observed in at least two telescope sites (stereo events) or the timing information of at least one SD tank is present (hybrid events). Figure 3.4 (right) shows the uncertainty in R_p and χ_0 for the monocular reconstruction and the hybrid one. It is visible that, by using the timing information of the tanks, the geometry uncertainties are highly reduced and the detector resolution is thus improved.

Indeed, hybrid events achieve the best geometric accuracy: the resolution on core location is 50 m, while the typical angular resolution is $0.6°$.

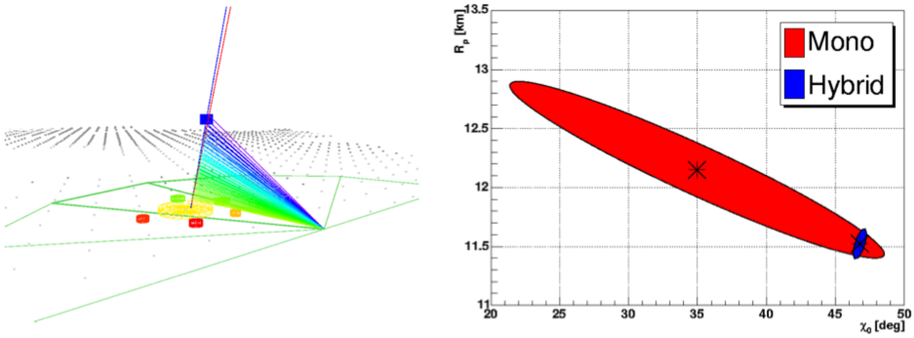

Figure 3.4: Left) 3D display of a real event. The FD pixels directions and the SD triggered tanks are shown. Color code reflects trigger time, tank size indicates particle density. Right) FD monocular reconstruction uncertainty (red) vs. hybrid uncertainty (blue) [Mostafa (2007)].

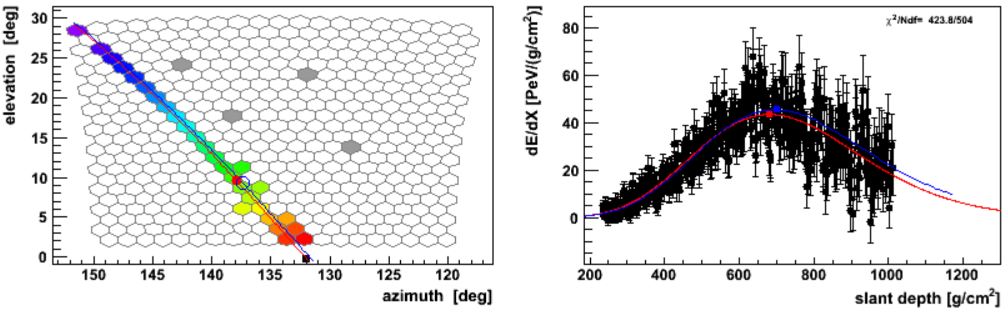

Figure 3.5: Left) A real event seen by the telescope sited in Loma Amarilla. The timing of the pixel pulses is denoted by color code (early =violet, late =red). Right) The reconstructed longitudinal profile (dots) fitted with the Gaisser-Hillas function.

3.1.4 The longitudinal profile and the energy reconstruction with the FD

As discussed in Chapter 2, the amount of fluorescence light emitted at the track element is proportional to the energy dissipated by the charged particles in that track. By fitting the measured longitudinal profile, is thus possible to derive the electromagnetic energy of the primary particle and to infer the primary mass.

In order to do that, the light attenuation in the atmosphere has to be estimated, as well as all contributing light sources. In particular the fluorescence light has to be disentangled from the direct Cherekov light, the scattered one and the multiple-scattered light. Then, the primary energy and X_{max} can be estimated by fitting the profile with the Gaisser-Hillas function [Gaisser & Hillas (1977)]. The latter is a function with four parameters that describes correctly the number of electromagnetic particles as a function of the atmospheric depth X:

$$N_e(X) = N_{X_{max}} \left(\frac{X - X_0}{X_{max} - X_0}\right)^{(X_{max}-X_0)/\lambda_r} e^{\frac{X_{max}-X}{\lambda_r}} \tag{3.2}$$

where X_0 is the first interaction point and λ_r is the interaction length characteristic of the electromagnetic cascade.

An example of a reconstructed longitudinal profile is shown in Figure 3.5.

The electromagnetic shower energy is then obtained as

$$E_{em} = \frac{E_c}{\lambda_r} \int N_e(X)dX \tag{3.3}$$

where E_c=80 MeV is the critical energy and $\lambda_r = 37\ g/cm^2$.

Finally, the total energy is estimated by correcting for the invisible energy carried away by neutrinos and high energy muons. The invisible energy is estimated using experimental data above $3 \cdot 10^{18}$ eV, for which the SD array is fully efficient [Aab et al. (2013)]. In particular high-quality hybrid events that trigger the SD and the FD independently are used. This significantly reduces the dependence on the hadronic interaction models and mass composition. The systematic uncertainties on the invisible energy decreases with energy from 3% to 1.5%. Due to the stochastic nature of air showers, the invisible energy is also affected by shower-to-shower fluctuations. These are parametrized according to [Unger et al. (2008)] and an uncorrelated uncertainty of about 1.5% is introduced.

The resolution in the measurement of the energy achieved by the FD depends also on the uncertainties associated to variations in the atmosphere, ranging from 4.5% at $3 \cdot 10^{18}$ eV to 6.9% at 10^{20} eV, and to the geometry reconstruction, which range from 5.2% to 3.3% for the same interval. The resulting overall energy resolution is almost constant with energy in the range [3, 100] EeV, and lays between 7% and 8% [Aab et al. (2013)].

The systematic uncertainties in the determination of E_{FD} have to be propagated to the determination of E_{SD} in order to obtain the systematic uncertainty of the energy scale. The systematics in the determination of the fluorescence yield (3.6%), the aerosol profile (about 5%), the FD calibration (10%), the FD profile reconstruction (about 6%) and the invisible energy (about 3%) contribute to an uncertainty of about 13%. When this value is combined with the uncertainty of the calibration fit (about 1%) and its stability over time (5%), the resulting systematic uncertainty of the energy scale ends up being 14% [Aab et al. (2013)].

The position of the shower maximum X_{max} is also inferred from the fit to the longitudinal profile, and the uncertainty associated with this estimate is less than 20 g/cm^2.

3.2 Surface Detector

The SD is an array of 1600 water Cherenkov tanks (WCD), covering an area of about 3000 km^2. The detectors are deployed on a triangular grid with 1.5 km spacing, allowing the study of cosmic rays with energy greater than $3 \cdot 10^{18}$ eV (energy at which the trigger efficiency is 1). Each water tank is readout by 3 photomultipliers (PMTs) and it is equipped with a data acquisition (DAQ), with a front-end electronic (FE) card for control and trigger, a solar panel with two batteries for power, a GPS receiver for the time tagging, and a custom radio emitter/receiver for trigger and data transfer to the Central Data Acquisition System (CDAS) [Allekotte et. al (2008)]. The signals from the three PMTs are obtained using Flash Analog to Digital Converters (FADC) that process them at 40 MHz sampling rate.

The Cherenkov water tanks are filled with 12 tons of water each, they are 1.2 m heigh and have a 1.8 m radius, for a collection area at 0° of about 10 m^2. They detect the Cherenkov light produced by particles crossing the water at ground level, mainly muons,

Figure 3.6: A SD tank in the Pampa Amarilla region.

electrons and positrons.

The SD has an almost 100% duty cycle.

3.2.1 SD Calibration

The measurement of the average charge produced by a vertical and central through-going muon, (Q_{VEM} where VEM=Vertical Equivalent Muon) and collected by a photomultiplier tube is essential for the calibration of the SD stations. It allows an in situ calibration with atmospheric muons, whose rate is approximately 2500 Hz.

The SD detector cannot select vertical muons. However, the distribution of light of atmospheric muons produces a peak in charge distribution, Q^{peak}_{VEM}, proportional to that of vertical muons. In particular, $Q^{peak}_{VEM} = 1.03 \pm 0.02$ VEM for each PMT, and approximately 1.09 VEM for the sum of the three PMTs, measured with a muon telescope providing the trigger in a reference tank [Aglietta et al. (2005)]. Atmospheric muons also produce a peak in a pulse height histogram. The gain in each PMT is set to have I^{Peak}_{VEM} at 50 ch. This choice translates in a mean gain of $\sim 3.4 \cdot 10^5$ for a mean $n_{p.e.}/VEM \sim 94$ p.e. The peak I^{Peak}_{VEM} is also used as the reference value for determining the trigger threshold levels for each station.

A continuous local calibration is performed to determine I^{peak}_{VEM}, mainly because of the day-night temperature variation, which can be larger than $20°C$ and can induce variations of the order of 2 ADC counts for the muon peak.

More details on the SD calibration procedure can be found in [Bertou (2006)].

3.2.2 SD trigger and event selection

Several triggers are used, either at local or central level. The signal background in the surface array is mainly produced by surviving muons from low energy showers that died out in the atmosphere. In order to select high energy showers over the background, a set of conditions has been arranged in a trigger hierarchy formed by five levels.

T1: two first level triggers are applied locally at WCD: a simple threshold trigger (ThT) and a time-over-threshold trigger (ToT).

The ThT is a 3-fold coincidence trigger with a threshold of 1.75 VEM on each PMT, and its rate is about 100 Hz.

The ToT requires 12 FADC bins with signals greater than 0.2 VEM in a sliding window of 120 bins in at least 2 of the 3 PMTs. This trigger is quite effective in eliminating the signals produced by lonely muons from small showers which are not absorbed.

T2: it is a local trigger, reducing the T1 rate to 20 Hz. ThT are promoted to T2 if a higher threshold of 3.20 VEM is reached with a 3-fold coincidence of the PMTs. ToT triggers are all automatically promoted to T2.

T3: The third level trigger, formed at CDAS level, is designed to select real showers triggering the stations, checking for relatively compact configurations. In particular T3 requires that at least 3 stations pass the ToT or 4 stations have a T2 in particular time space configurations.

The next trigger levels, T4 and T5, are applied offline to recorded data and are intended to select physics events from the stored data set.

T4: it defines spatial and timing criteria to ensure the subsequent reconstruction of the event.

T5: it selects high-quality events, reconstructed with a known energy and good angular accuracy, with the core inside the array. Indeed, events with the core located at the border of the array may have biased estimate of the core position and energy. Therefore, the T5 trigger requires that the tank with the highest signal has at least 5 working tanks among its 6 closest neighbors at event time. In addition, the reconstructed core must be inside an equilateral triangle of working stations.

3.2.3 SD aperture and exposure

The aperture of the SD array is given by the effective area integrated over solid angle. The latter is equal to the geometrical one if the trigger and event selection have full efficiency. Indeed the acceptance does not depend on the mass of the primary, arrival direction and energy.

When the SD array is fully efficient, he calculation of the exposure is based solely on the determination of the geometrical aperture and the observation time. The aperture of the array is obtained as a multiple of the aperture of an elemental hexagon cell, defined as an active detector surrounded by six active neighbors. In this context, the stability and uniformity of the trigger rates is crucial.

The response of the surface detector array was simulated using Geant4 [Agostinelli et al. (2003)] within the framework provided by the Offline Software [Argiro et al. (2007)].

The resulting trigger probability as a function of the Monte Carlo energy for proton, iron and photon primaries is shown in Figure 3.7 for showers with zenith angle up to 60° . Due to their larger muon content, at low energies iron primaries are slightly more efficient at triggering the array than protons. However, the trigger becomes fully efficient at $3 \cdot 10^{18} eV$, both for proton and iron primaries, in different intervals of zenith angles. It is important to notice that the trigger efficiency for photons is much lower. This is because photons tend to produce deeper showers that are poor in muons. The trigger efficiency versus energy has been checked with data too [Abraham et al. (2010)].

For the determination of the observation time, dead times are taken into account: bad periods are evaluated through an empirical technique based on the distribution of arrival times of events [Bonifazi & Ghia (2006)].

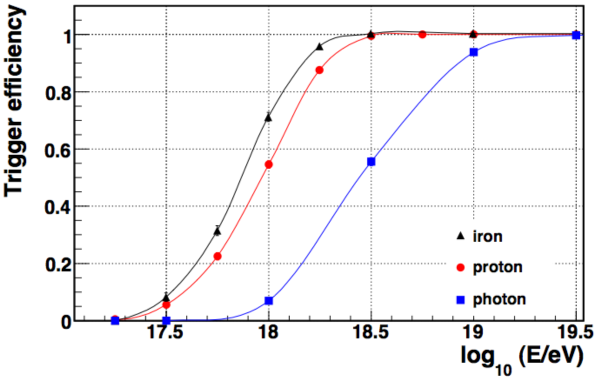

Figure 3.7: The SD trigger efficiency as a function of Monte Carlo energy for proton (circles), iron (triangles) and photon primaries (squares) and zenith angle integrated up to 60°. [Rivera Bretel (2014)].

The current Auger exposure reaches nearly 40.000 km^2-sr and provides an unprecedented quality data set [Letessier-Selvon (2013)].

3.2.4 Geometric reconstruction with the SD

The geometric reconstruction of the event is based on timing information from stations. The timing information is obtained from the GPS receiver, and the absolute time resolution is 10 ns. As a first step, the shower front is assumed to be flat and an angular resolution of few degrees for both zenith and azimuth angle is reached. Then, it is possible to refine the approximation using a curved shower plane geometry, but the knowledge of the shower core position is needed.

The latter is estimated by fitting the lateral distribution function (LDF), which describes the transverse development of the EAS and is constructed by the particle densities measured in each station. Then, the core position is used to apply a spherical fit to the shower front and improve the determination of the arrival direction. The angular resolution as function of the zenith angle is shown in Figure 3.8(left). For events with energy above 10^{19} eV, for which 6 or more stations are triggered, the angular resolution is better than 1°, in the whole angular range.

3.2.5 Energy reconstruction with the SD

As seen in Chapter 2, the density of particles at a fixed distance r_{opt} gives a reliable estimation of the energy of the primary cosmic ray. Different attenuation characteristics of the electromagnetic and muonic shower components lead to different reconstruction methods for different zenith angle ranges.

The energy reconstruction of vertical events, i.e. with a zenith angle smaller than 60°, is based on the estimation of the lateral distribution of secondary particles of an air shower reaching ground at an optimal distance to the shower core. Due to the discrete sampling at ground, the particle density at the desired distance can only be obtained through a fit to the distribution of the particle densities at ground (the LDF). As was discussed in Section 2.4, the optimal distance at which the sum of the shower-to-shower

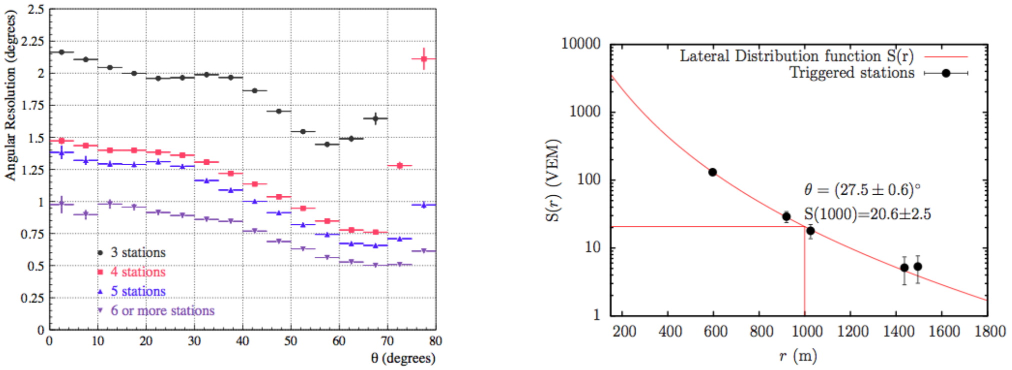

Figure 3.8: Left) The angular resolution as a function of the zenith angle and for events with 3 stations (circles), 4 stations (squares), 5 stations (up-triangles), and 6 or more stations (down-triangles). Right), the lateral profile of a shower as reconstructed with the SD [Rivera Bretel (2014)].

fluctuations and of the statistical fluctuations from particle counting is minimum, is conditioned by the geometry of the array and is determined empirically. For the main array of the SD, $r_{opt} = 1000\ m$ [Newton et al. (2006)], while for the infill is $r_{opt} = 750\ m$.

The lateral dependence of signals is

$$S(r) = S_{1000} f_{LDF}(r) \tag{3.4}$$

where $f_{LDF}(1000\ m) = 1$. S_{1000} is called the size parameter and it is used to estimate the primary energy. An example of a fitted LDF is shown in Figure 3.8(right).

S_{1000} cannot be used directly as the estimator of the shower energy. Indeed it must be corrected for their zenith angle dependence due to air shower attenuation in the atmosphere. The correction is done by means of an attenuation curve (see Figure 3.9),

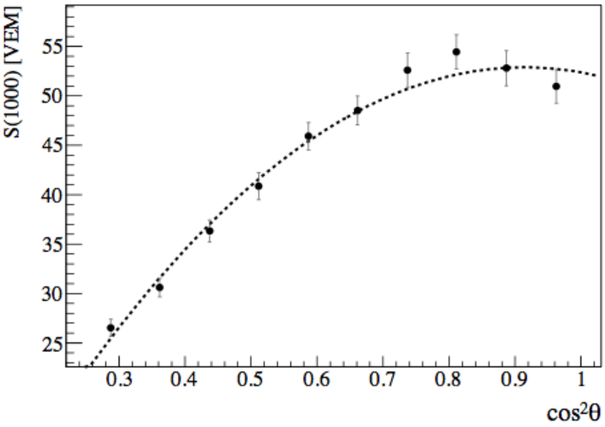

Figure 3.9: The attenuation curve for showers detected by the main array of the SD. The solid line represents the fit described by a polynomial of second order [Rivera Bretel (2014)].

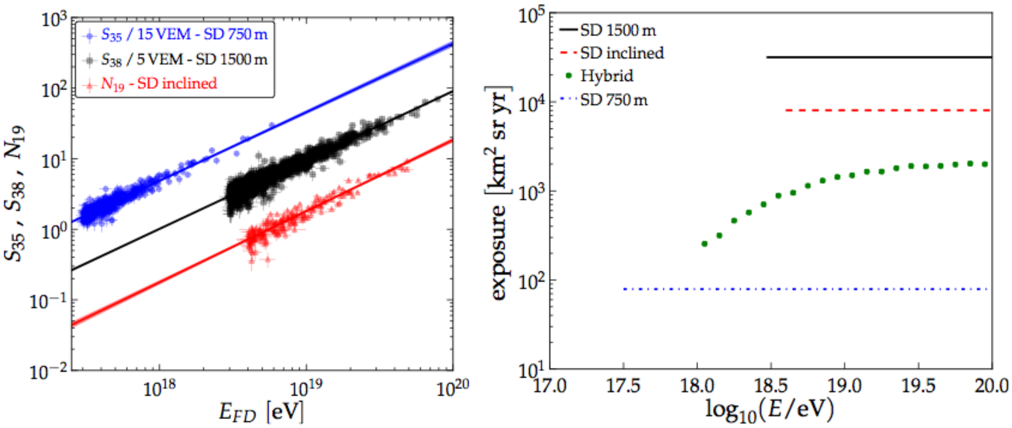

(a) S_{38}, S_{35} and N_{19} vs. E_{FD}. (b) Exposure of the different datasets.

Figure 3.10: Left) Energy calibration in the Pierre Auger Observatory. Correlation between S_{38}, S_{35} and N_{19} with the energy measured by the FD. Right) Exposure for the different methods of measuring the energy [Letessier-Selvon (2013)].

derived by means of the Constant Intensity Cut (CIC) method [Hersil et al. (1961)] in the hypotesis that the flux of cosmic rays is isotropic above a certain primary energy threshold. The assumption means that the number of particles per unit area is independent of arrival direction, and that spectral features are shared among all particles. Even though anisotropies have been measured by a number of different instruments over a wide energy range, the effect is very small.

The energy estimator independent on the zenith angle is

$$S_{38} = S_{1000}/p(x) \tag{3.5}$$

which is the S_{1000} that the shower would have produced arriving at the median zenith angle, 38°. In Equation 3.5 $x = cos^2\theta - cos^2 38°$ and p is the third order polynomial obtained from the CIC analysis [Aab et al. (2013)].

A set of hybrid events, for which both S_{38} and E can be measured, is then used to derive the correlation between these two variables, exploiting a maximum likelihood method [Aab et al. (2013)] which takes into account the evolution of uncertainties with energy, as well as event migrations due to the finite resolution of the SD.

The energy associated to each event is

$$E_{FD} = A \cdot S_{38}^{B} \tag{3.6}$$

where the coefficients A and B are determined by a fit applied to the correlation between S_{38} and the energy estimated by FD. In Figure 3.10(left), the calibration curve is shown for the different energy estimators: S_{38}, S_{35} for the infill array and N_{19} for the inclined events, i.e. with a zenith angle greater than 60°.

Inclined air-showers are characterized by the dominance of secondary muons at ground, as the electromagnetic component is largely absorbed in the large atmospheric depth traversed by the shower Therefore, the reconstruction is based on the estimation of the relative muon content N_{19} with respect to a simulated proton shower with energy

10^{19} eV. In particular, the measured signals are fitted to muon density distributions predicted with atmospheric cascade models to obtain the relative shower size as an overall normalization parameter. The method is evaluated using simulated showers in order to test its performance and the energy of the cosmic rays is calibrated using a sub-sample of events reconstructed with both the fluorescence and surface array techniques. The independent measurement of the energy spectrum of ultra-high energy cosmic rays using very inclined events collected by the Pierre Auger Observatory provides the basis of complementary analyses [see Aab et al. (2014) for details].

Using the calibration curve, it is thus possible to derive the energy for each of the (many more) events recorded by the SD. From the ratio E_{SD}/E_{FD}, and considering that the E_{FD} energy has a resolution of 7.6%, the resulting SD energy resolution goes from 16% at the lower energy edge to 12% at the highest energies.

The exposure estimated for the different methods of measuring the energy is shown in Figure 3.10(right). The SD exposure in the three cases is flat above the energy corresponding to full trigger efficiency for the surface arrays.

CHAPTER 4

Overview of Mass Composition Studies at Auger

Measuring the cosmic ray composition at the highest energies, along with other measurements such as the flux and the arrival direction distribution, is crucial to separate the different scenarios of origin and propagation of cosmic rays.

On a shower to shower basis, compositions studies are difficult because of the intrinsic shower to shower fluctuations which characterize shower properties. These fluctuations come from the random nature of the interaction processes, in particular the position of the first interaction, and from the discrete sampling at ground. However, showers originating from different primaries can, at least statistically, be distinguished, given the different cross section with air nuclei.

In this chapter we will briefly discuss the different observables sensitive to primary mass that the Pierre Auger Observatory can measure. Firstly the FD observables will be described, then we will focus on the SD ones.

4.1 FD observable sensitive to mass

The atmospheric depth at which the shower reaches its maximum development, X_{max}, carries information about the primary mass and the hadronic interaction properties at very high energy, as we have seen in Chapter 2.

For a given shower, X_{max} is determined by the depth of the first interaction of the primary in the atmosphere, plus the depth the cascade takes to develop (see Equation 2.2).

The depth of the first interaction is expected to be a decreasing function of the logarithm of the primary energy, while the depth of the shower development rises as the logarithm of the energy, as shown in Section 2.1.1.

The measured distribution of X_{max} is therefore the result of the folding of the first interaction depth distribution, the shower to shower development fluctuations, and the detector resolution.

Under the assumption of the superposition model, X_{max} is linear with $ln(E/A)$ where A is the primary mass [Matthews (2005)]. Therefore, showers generated by heavier primaries develop faster than those generated by lighter ones. For a given primary energy, heavier primary showers are characterized by smaller fluctuations, which makes the whole longitudinal development distribution sensitive to the mass composition.

The fluorescence telescopes can be used to measure the depth of the shower maximum with high precision (20 g/cm^2). The small systematic uncertainties on X_{max} measurement (less than 10 g/cm^2) makes it the most reliable source of information in composition studies at the Pierre Auger Observatory.

4.1.1 X_{max} and RMS(X_{max}) measurement

The updated results for X_{max} and the width of its distribution, i.e. RMS(X_{max}), are shown in Figure 4.1.

The total uncertainty in the reconstruction of X_{max} is calculated including the uncertainties due to the geometry reconstruction and to the atmospheric conditions. There are several sources of the systematic uncertainties: calibration, atmospheric condition, reconstruction, event selection and the uncertainty of the FD energy scale. All contribute at the same level and independently of energy.

Quality cuts related to the geometry reconstruction, to the atmosphere condition and to the uncertainty in the measurement of X_{max} are applied. In particular the selection cuts have been determined using Monte Carlo simulations of the showers and of the telescopes with the goal of selecting events in which the uncertainty in the measurement of X_{max} is less than 40 g/cm^2 (for details see [Aab et al. (2014)]).

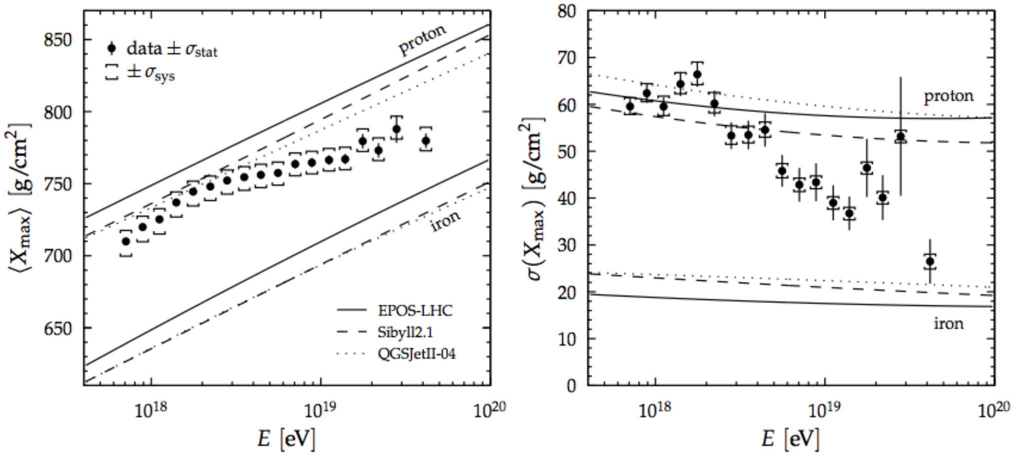

Figure 4.1: X_{max} (left) and RMS (X_{max}) (right) as a function of the energy. Data (points) are shown with the predictions for proton and iron for several hadronic interaction models. 19872 high-quality FD events are considered in the analysis [Aab et al. (2014)].

The evolution of X_{max} with energy, shown in Figure 4.1 (left), is different from the one expected for either a pure-proton or pure iron composition. In particular, the results show an evolution of the average composition of cosmic rays towards lighter nuclei up to energies of $10^{18.27}$ eV. Above this energy, the trend reverses and the composition becomes heavier.

It is notable that the energy of the first data point in Figure 4.1 corresponds to a center-of-mass energy that is only 4 times larger than the one currently available at the LHC ($\sqrt{s}$ = 8 TeV). Therefore, the uncertainties due to the extrapolation of hadronic interactions to the lower energy threshold of this analysis should be small. On the contrary, the last energy bin at $\langle log(E/eV)\rangle = 19.62$ corresponds to a center-of-mass energy that is a factor of about 40 higher than the LHC energies and the model predictions have to be treated more carefully.

A similar behavior is visible for the width of the X_{max} distribution, the RMS (X_{max}), shown in Figure 4.1 (right). The latter decreases gradually with energy, as it would be expected for showers induced by heavy nuclei.

MC predictions are more uncertain for X_{max} than for RMS (X_{max}), since the profile maximum depends also on the multiplicity in hadronic interactions [Ulrich et. al (2011)].

Assuming that the modeling of hadronic interactions gives a fair representation of the actual processes in air showers at ultra-high energies, data suggest a very light or mixed composition at around $10^{18.3}$ and a heavier composition (CNO or heavier nuclei) at higher energies, up to $10^{19.6}$.

4.1.2 $\langle lnA \rangle$ measurement

The two observables X_{max} and RMS(X_{max}) are often used as different and independent aspects of the same phenomenon. However, they do not reflect the cosmic ray composition to the same extent.

According to the superposition model, $\langle X_{max} \rangle$ is linear in $\langle lnA \rangle$, measuring the primary mass for both pure and mixed compositions.

On the other hand, the relation between RMS($\langle X_{max} \rangle$) and the primary mass is not straightforward, as different combinations of average compositions can give rise to the same value of RMS($\langle X_{max} \rangle$). Only in the case of pure composition is this correspondence unique.

Assuming the generalized Heitler model of extensive air showers, $\langle X_{max} \rangle$ is given by

$$\langle X_{max} \rangle = X_0 + D\ log_{10}(\frac{E}{E_0 A}) \tag{4.1}$$

where X_0 is the mean depth of proton showers at energy E_0 and D is the elongation rate. For nuclei of the same mass A, the shower maximum is expected to be on average

$$\langle X_{max} \rangle = \langle X_{max} \rangle_p + f_E lnA \tag{4.2}$$

while its dispersion

$$\sigma^2(X_{max}) = \sigma^2_{sh}(lnA) \tag{4.3}$$

is influenced by shower-to-shower fluctuations only [Abreu et al. (2013)]. Here $\langle X_{max} \rangle_p$ is the mean depth at maximum of proton showers, and $f_E = \xi - D/ln10 + \delta log_{10}(E/E_0)$, where ξ, δ, D depend on the specific interaction model.

In the case of a mixed composition, the mean and variance of X_{max} depends on lnA distribution. The two equations above become

$$\langle X_{max} \rangle = \langle X_{max} \rangle_p + f_E \langle lnA \rangle \tag{4.4}$$

$$\sigma^2(X_{max}) = \langle \sigma^2_{sh} \rangle + f_E \sigma^2_{lnA} \tag{4.5}$$

where $\langle \sigma^2_{sh} \rangle$ is the average shower-to-shower variance of X_{max} weighted according to the lnA distribution, and σ^2_{lnA} is the variance of the lnA distribution.

Using measurements of X_{max} and RMS(X_{max}), Equations 4.4 and 4.5 can be inverted to get the first two moments of the lnA distribution.

From equation 4.4

$$\langle lnA \rangle = \frac{\langle X_{max} \rangle - \langle X_{max} \rangle_p}{f_E} \tag{4.6}$$

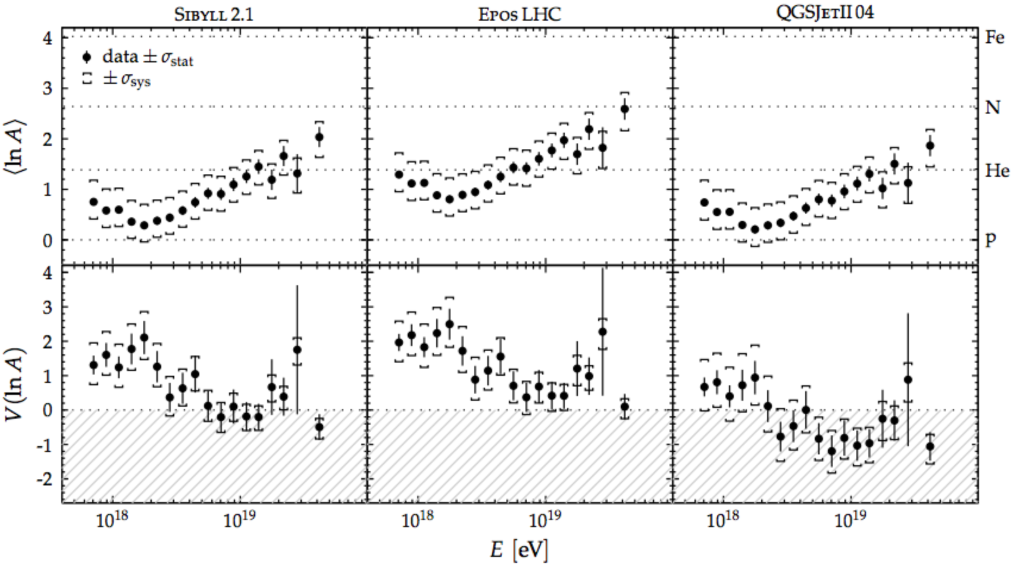

Figure 4.2: $\langle lnA \rangle$ (top) and the variance V(ln A) (bottom) as a function of energy obtained from Auger data are shown for different hadronic interaction models. Error bars show statistical errors, while in the bottom plots the non-physical region of negative variance is indicated as the gray dashed region [Aab et al. (2014)].

By parametrizing $\sigma^2_{sh}(lnA)$ with a quadratic law

$$\sigma^2_{sh}(lnA) = \sigma^2_p[1 + alnA + b(lnA)^2] \tag{4.7}$$

and averaging it, one obtains

$$\langle \sigma^2_{sh} \rangle = \sigma^2_p[1 + a\langle lnA \rangle + b\langle (lnA)^2 \rangle] \tag{4.8}$$

Substituting in eq. 4.5 and solving in σ^2_{lnA} one finally obtains

$$\sigma^2_{lnA} = \frac{\sigma^2(X_{max}) - \sigma^2_{sh}(\langle lnA \rangle)}{b\sigma^2_p + f^2_E} \tag{4.9}$$

Equations 4.8 and 4.9 have been used to interprete the Pierre Auger Observatory data in terms of mass composition. Since the procedure depends on the hadronic model, one gets a plot for each different model.

The evolution of $\langle ln\ A \rangle$ and of the variance σ^2_{lnA}, called V(ln A) from now on, are shown as a function of the energy in Figure 4.2. Proton-pure, mixed and iron-pure composition correspond to $\langle ln\ A \rangle = 0$, $\langle ln\ A \rangle \sim 2$ and $\langle ln\ A \rangle = 4$ respectively.

The behavior of the two variables with energy is similar for all hadronic models, despite the different uncertainties and mass offsets: the data imply an increasing $\langle ln\ A \rangle$ above $10^{18.3}$ eV from light to intermediate masses and a decreasing of $V(lnA)$ as the energy increases.

The highest masses are obtained for EPOS-LHC while Sibyll-2.1 and QGSJetII-04 show intermediate values.

Another important point to note is that, while $\langle ln\ A\rangle$ is always positive, $V(lnA)$ is negative in a wide energy range. Considering equation 4.9, this happens when the shower fluctuations corresponding to the mean log mass are greater than the measured X_{max} ones.

Figure 4.2(bottom) shows that data points relative to V(lnA) are within the allowed physical regions only for EPOS-LHC and Sibyll-2.1 while they are partially outside above $10^{18.4}$ eV for QGSJetII-04. The interpretation with EPOS-LHC leads to the heaviest average composition that is compatible with the ln A of nitrogen at the highest energies. The variance of ln A derived with EPOS-LHC and SIBYLL2.1 suggests that the flux of cosmic rays is composed of different nuclei at low energies and that it is dominated by a single type of nucleus above $10^{18.7}$ eV where V(ln A) is close to zero. The interpretation with QGSJetII-04 leads to unphysical variances and it is thus disfavored by the data.

The systematic uncertainties are large and do not allow to establish stringent tests to the models. However, the common energy evolution suggests that the average mass increases as a function of energy, with a decreasing log mass dispersion.

4.2 SD observables sensitive to mass

The number of events detected by FD at high energy is low, due to the small FD duty cycle (about 15%); the stringent cuts imposed to avoid a biased data sample in the analysis, such as the field of view cut, further reduce the available statistics.

The Pierre Auger Collaboration has thus developed different methods to infer composition through SD measurements. Indeed, the 100% duty cycle allows the SD to provide a large statistical sample even at the highest energies. Different properties measurable through the SD , like the total signal rise time or the curvature of the shower front, can be also used to indirectly study to the composition. In the Subsection 4.2.1, we will briefly describe the risetime correlation with the primary mass.

The muon component is one of the most sensitive observables to the primary mass. As seen in Section 2.1.2, an air shower induced by a nucleus with A nucleons contains about $A^{1-\alpha}$ ($\alpha \simeq 0.9$) more muons that a proton shower with the same energy.

In addition, since muons come from the decay of pions and kaons which form the hadronic core and suffer a small energy losses and angular deflections on their way to ground, they are sensitive to hadronic interactions.

In Subsections 4.2.2 and 4.2.3 we will present the most important methods used to measure the muon component of the shower through the SD signals at ground.

In Section 4.3 we will describe the Muon Production Depth (MPD) analysis which reconstruct the muon longitudinal profile by means of the muon arrival time measurement at ground.

4.2.1 Risetime Asymmetry

For each SD event, the water Cherenkov detectors record the signal produced at ground by charged particles as function of time. The first part of the trace is dominated by the muon component, which arrives earlier and over a shorter time period than the electromagnetic one. Indeed muons travel almost in straight lines, while electromagnetic particles suffer multiple scattering on their way to ground.

As a consequence, the time profile of particles at ground is sensitive to the cascade development and to the primary mass. The time distribution of the SD signal can be characterized by means of the risetime $t_{1/2}$, i.e. the time needed to go from 10% to

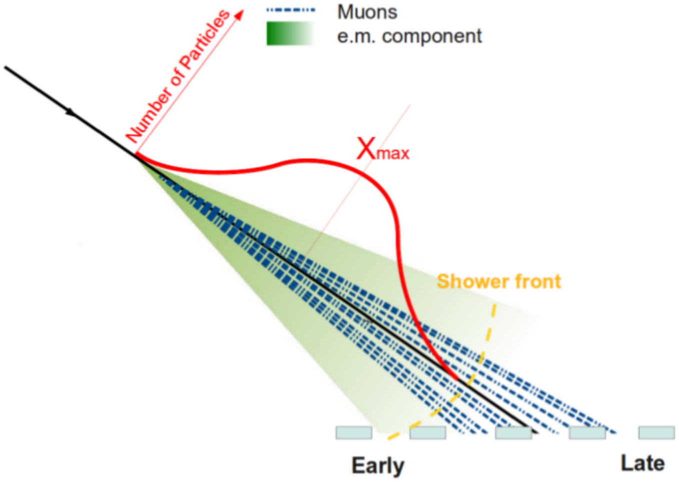

Figure 4.3: A sketch to show the risetime asymmetry in non-vertical showers.

50% of the total integrated signal. The risetime depends on the distance to the shower maximum, the zenith angle and the distance to the core.

Besides, the risetime of non-vertical showers is characterized by an azimuthal asymmetry, as it is depicted in Figure 4.3. Indeed *early* stations, located upstream with respect to the air shower axis, are characterized by a greater risetime than *late* stations, located downstream, due to the absorption of the EM component and to geometry. The amplitude of the asymmetry varies with zenith angle (0 for vertical and nearly 0 for horizontal) and thus goes through a maximum. The position of the maximum is a function of the average shower depth at that particular energy and is therefore a mass indicator.

For a given (E, $sec\theta$) bin, a fit of $\langle t_{1/2}/r \rangle = a + bcos\zeta$ provides the asymmetry amplitude, *a/b*. ζ is the azimuth angle in the shower plane. The value of $sec\theta$ for which *a/b* is maximum is called Θ_{max}.

The evolution of Θ_{max} with energy is shown in Figure 4.4. The results are relative to events with energy greater than 3.16 EeV and zenith angle smaller than $60°$ detected by Auger between January 2004 and December 2010 [Abreu et al. (2011)].

The evolution of Θ_{max} with energy is similar to the one of X_{max}, despite the fact that the two analyses come from completely independent techniques. In particular, at the highest energies both analyses consistently show that Auger data resemble more the simulations of heavier primaries than pure protons.

4.2.2 Measurement of the muon signal using vertical events

In vertical events, i.e. events with zenith angle $\theta < 60°$, the signal at ground is produced by both electromagnetic particles and muons. The two components produce signals with different time distribution, and this feature can be exploited to disentangle them. In particular two different filtering techniques, the smoothing and the multivariate method, have been applied to signals measured with the SD detectors, demonstrating the ability to separate the two components.

The two methods have been tuned on 10 EeV proton and iron showers, at the reference distance of 1000 m from the shower core. This will allow to compare the methods

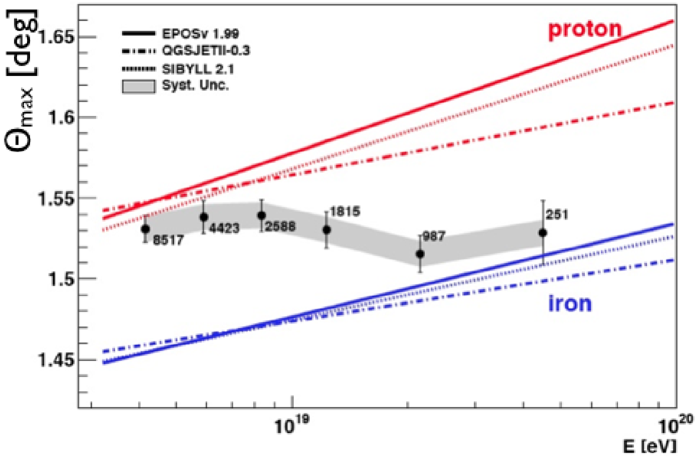

Figure 4.4: Results on risetime asymmetry compared with models prediction. The error bars correspond to the statistical uncertainty. The systematic uncertainty is represented by the shaded bands. The number of events in each energy bin is also quoted [Abreu et al. (2011)].

results evaluating the muon number at energies where the mass composition is quite well known.

Smoothing method The smoothing technique exploits the smoothed nature of the electromagnetic trace to extract it from the total trace of each tank. The technique consists in a low-pass filter applied to the signal few times, in order to gradually separate the low-frequency smooth electromagnetic signal from the high-frequency component which is assigned to muons.

Since the smoothing method is part of the thesis work, it will be described in detail in Chapter 5. In particular the method accuracy and the systematics will be discussed, together with the background.

Multivariate method The multivariate technique exploits the muon-content sensitive characteristics of the FADC signal to measure the muon fraction [Aab et al. (2013)].

The muon fraction is estimated by

$$f_{mu} = a + b \cdot \theta + c f_{0.5}^2 + d\theta P_0 + er \tag{4.10}$$

where θ is the reconstructed zenith angle, r is the distance of the station from the reconstructed core and $f_{0.5}$ is the portion of signal in FADC bins larger than 0.5 VEM.

P_0 is the normalized zero-frequency component of the power spectrum:

$$P_0 = \frac{S^2}{N\sum_{j=1}^{N} x_j^2} = \frac{<x>^2}{<x^2>} = [1 + \frac{\sigma^2(x)}{<x>^2}]^2 \tag{4.11}$$

where $<x>= S/N$ is the mean of the signal vector $x = (x_1, ..., x_N)$, $\sigma^2(x)$ is the variance of the signal vector and $<x^2>$ is its second moment. Both $f_{0.5}$ and P_0 are sensitive to large relative fluctuation and short signals, which are the signatures of high muon content. The fit parameters (a, b, c, d, e) in Equation 4.10 have been estimated using simulations.

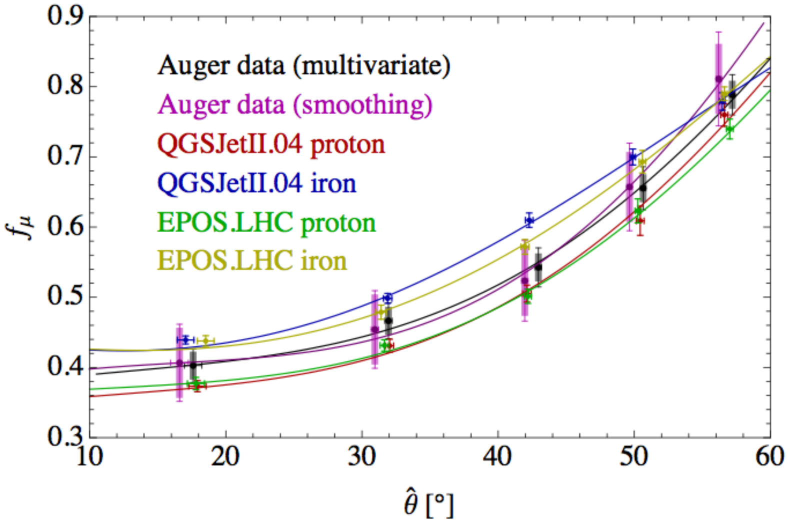

Figure 4.5: The muon fraction for primary energy E = 10^{19} eV in a SD station at 1000 m from the shower axis, as a function of the reconstructed zenith angle θ. For Auger data, the rectangles represent the systematic uncertainties, and the error bars represent the statistical uncertainties added to the systematic uncertainties. The points for Auger data are artificially shifted by $\pm 0.5°$ for visibility. [Aab et al. (2013)]

4.2.2.1 The Muon fraction and the muon signal

The muon fraction

$$f_\mu = S_\mu / S_{tot} \tag{4.12}$$

has been evaluated using both techniques at 1000 m from the core, for primary energies of 10 EeV.

In Figure 4.5, f_μ is shown as function of the zenith angle. The muon fractions obtained with the two analysis methods are in agreement, and the model predictions from proton and iron showers bracket the measured muon fractions within uncertainty.

By combining the estimated muon fraction with the total signal at 1000 m from the shower core, it is possible to estimate the muon signal.

Even if the considered energy and zenith angle ranges are narrow, the total signal must be corrected for the distance and energy dependence, introducing:

- a correction to recover the total signal at 1 km from the core, since the muon signal is basically constant in the considered distance range, but the total one changes with respect to S(1000) by about $\pm 10\%$ in the considered range [950-1050] m:

  $$S(1000) = S(r) \cdot LDF(1000)/LDF(r) \tag{4.13}$$

  where $LDF(r) = r^\beta$ is the Lateral Distribution Function of the total signal and $\beta = -3.45$ has been chosen from the data (although a different choice would not affect the result significantly).

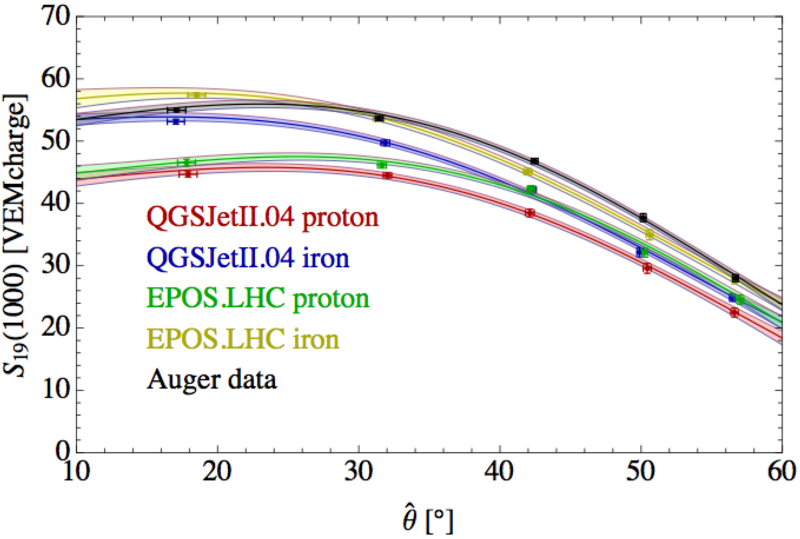

Figure 4.6: The mean total signal for primary energy E = 10^{19} eV in a detector at 1000m from the shower axis, as a function of the reconstructed zenith angle θ. [Aab et al. (2013)]

- a correction of the order of few % in the considered range $log_{10}E = [18.98 - 19.02]$ to rescale the total signal at 10 EeV, evaluated using the calibration

$$S_{19}(1000) = S(1000) \cdot C(E) \tag{4.14}$$

  where $C(E) = (E/10^{19}eV)^{-0.996}$, whose exponent comes from the slope of the energy dependence of S(1000) as derived from [Pesce (2011)].

Before applying eq. 4.14 the reconstructed energy is multiplied by a factor of 0.984, in order to correct for the migration effect due to the steep slope $\gamma = -2.26$ of the energy spectrum and the 12% energy resolution.

Figure 4.6 depicts the mean total signal $S_{19}(1000)$ as a function of the reconstructed zenith angle. The mean signal in data is greater than the one of QGSJetII-04-proton simulations and somehow exceeds the one of QGSJetII-04-iron simulations. The observed discrepancy is possible since the function which relates the ground signal to the primary energy is calibrated to E_{FD} and not determined by MC simulations. The same conclusion comes from the analysis of horizontal events ($\theta > 62°$), that will be discussed in Section 4.2.3.

4.2.2.2 The muon signal scaling

The results from the two different muon analyses pointed to a clear muon deficit in the simulations, being the experimental muon signal much larger than that predicted by QGSJet hadronic interaction model. The ratio between the estimated muon signal and the one expected from simulations of proton showers based on the QGSJet hadronic interaction model has been estimated at 1000 m from the core and at 10 EeV.

This ratio is shown in Figure 4.7 as a function of the zenith angle. The angular bins have been chosen such to include almost the same number of events. The rectangles

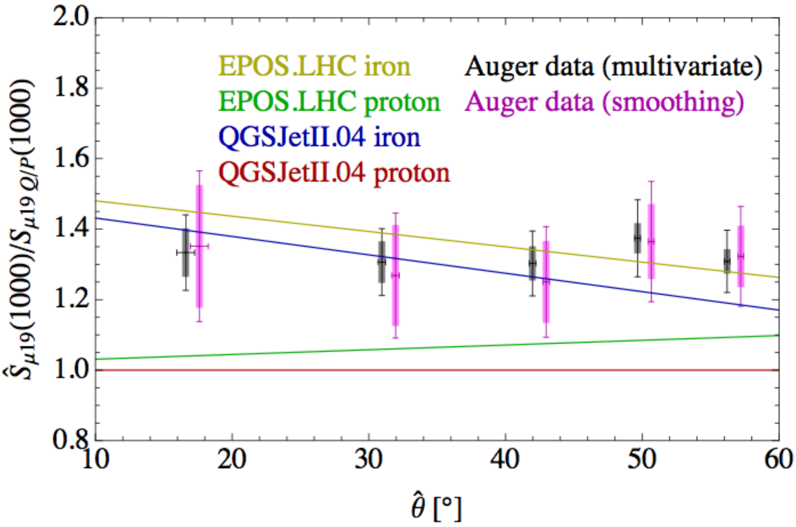

Figure 4.7: The measured muon signal rescaling at E = 10^{19} eV and at 1000 m from the shower axis vs. zenith angle, with respect to QGSJETII-04 proton as baseline. The small rectangles represent the systematic uncertainties, and the error bars represent the statistical uncertainties added to the systematic uncertainties. The points for Auger data are artificially shifted by $\pm 0.5°$ for visibility. [Aab et al. (2013)]

correspond to the systematic uncertainties, while the error bars represent the statistical errors.

The results from the the smoothing technique and the multivariate method are in good agreement and, on the basis of MC predictions, suggest an heavy composition. In particular, the measured *muon scale*, the ratio of the muon signal in data to the predicted one in QGSJetII-04, at 10^{19} eV and 1000 m from the core, in the angular range $[0° - 60°]$ is

$$\begin{aligned} 1.33 \pm 0.02(stat) \pm 0.05(sys) \qquad (multivariate) \\ 1.31 \pm 0.02(stat) \pm 0.09(sys) \qquad (smoothing) \end{aligned} \tag{4.15}$$

Since the results on X_{max} are not compatible at these energies with an iron dominated composition (see Figure 4.2), it seems reasonable to conclude that both the overall detector signal and the muon one are not reproduced well by the shower simulations. Similar results have been found from the analysis of hybrid events of Auger [Aab et al. (2013)]. In particular the analysis, aimed to test the leading, LHC-tuned, hadronic interaction models, have shown that the ground signals of simulated events have a factor 1.3-1.6 deficit of hadronically-produced muons relative to observed showers.

It is thus clear that comparing simultaneously the measured longitudinal profile and the surface detector signals to simulation provides constraints on hadronic models.

4.2.3 Measurement of the muon signal using horizontal events

Both electromagnetic particles and muons produce signals that can be recorded in the SD stations. However, the induced extensive air showers produced by horizontal events, i.e. events with zenith angle greater than $62°$, are characterized mostly by secondary energetic muons at ground.

Indeed, in horizontal events the electromagnetic component is largely absorbed by the atmosphere before reaching ground. Therefore, the study of these events provide an almost direct measurement of the muon content at ground level.

The method is discussed in depth in [Aab et al. (2014)]. We reported here a summary of the analysis and the results achieved.

Once the shower direction is established, the shower size parameter N_{19} is defined as:

$$\rho_\mu = N_{19} \cdot \rho_{\mu,19}(x, y, \theta, \phi) \tag{4.16}$$

where ρ_μ is the model prediction for the muon signal density at ground used to fit the signals recorded in the stations and $\rho_{\mu,19}$ is the refererence profile corresponding to the inferred arrival direction. $\rho_{\mu,19}$ comes from a parametrization of the muon density at ground for 10 EeV proton showers, simulated with CORSIKA and QGSJetII-03.

The electromagnetic contamination, although small, has to be taken into account. Indeed, before performing the fit of the estimated ρ_μ, the muonic signal is obtained from the total one by subtracting the average contribution of the electromagnetic component. The latter is about the 20% of the muonic signals and has been parametrized from simulations [Aab et al. (2013)].

Given $N_\mu(N_{\mu,19})$ as the total number of muons reaching ground as predicted by the integral of Equation 4.16, we obtain:

$$N_{19} = N_\mu / N_{\mu,19} \tag{4.17}$$

which depends on the primary energy and mass.

The N_{19} parameter has been compared with the true ratio $R_{mu}^{MC} = N_\mu^{MC}/N_{\mu,19}$ in order to test its effectiveness as estimator of the total number of muons.

Only events with energy greater than $10^{18.5}$ eV have been considered, in order to assure a trigger efficiency of 100% for both FD and SD detectors. Besides, only events with zenith angles between 62° and 80° have been selected.

The reconstruction bias results to be smaller than 5% for showers with $R_{mu}^{MC} > 0.6$, value above which the SD array is more than 95% efficient. For this result, we can conclude that N_{19} provides a direct measurement of the relative number of muons with respect to the reference distribution with a little bias. The latter is parametrized and the value of N_{19} after the correction for the bias is called R_μ in the following.

R_μ depends on energy and it is thus scaled to E_{FD} in order to compare the measured number of muons with predictions.

In Figure 4.8 the average scaled quantity $R_\mu/(E_{FD}/10^{19}eV)$ is shown as function of energy, together with the model predictions. The measured number of muons is marginally comparable to iron showers predictions between $4 \cdot 10^{18}eV$ and $2 \cdot 10^{19}eV$ only if the FD energy scale is increased by its systematic uncertainty (+14%). This is effective for both QGSJetII-04 and EPOS LHC.

Since the results on X_{max} are not compatible at these energies with an iron dominated composition (see Figure 4.2), it seems reasonable to conclude that the number of muons is not reproduced well by the shower simulations. This result is compatible with those obtained for vertical showers ($\theta < 60°$) shown in Section 4.2.2.

For this reason, it is important to study different kind of observables sensitive to both mass composition and hadronic interaction in order to improve the hadronic interaction models.

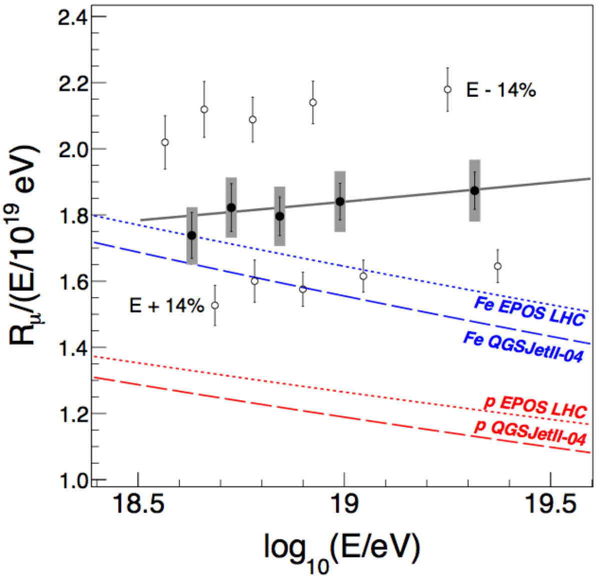

Figure 4.8: Average value of $R_\mu/(E_{FD}/10^{19}eV)$ as a function of shower energy. Reference curves for proton and iron showers simulated with QGSJetII-04 and EPOS LHC are shown for comparison. Open circles indicate the result if the FD energy scale is varied by its systematic uncertainty. The black line represents the calibration fit done with E_{FD}. The gray thick error bars indicate the systematic uncertainty of R_μ [Aab et al. (2013)]. See text for details.

In this context, additional informations are provided by the muon production depth reconstruction, which is attained through the reconstruction of the arrival time of muons at ground. We present below the muon time distribution model, and the MPD analysis performed for inclined events. The MPD profile properties, and the extension of the MPD analysis to lower zenith angles will be discussed in Chapters 6 and 7, since the latter is the main topic of the thesis.

4.3 Muon production depth reconstruction

The reconstruction of the MPD is a promising method developed by the Pierre Auger Collaboration in order to study the primary cosmic rays composition, with the aim of extending the energy range covered by the measurement of the depth of shower maximum performed through the Fluorescence Detectors, i.e. log(E/eV)=[17.8,19.6] eV.

The Surface Detector provides information about the longitudinal development of the hadronic component of extensive air showers in an indirect way, through the time distribution of the traces recorded by the FADC in each station.

A phenomenological model for muon time distributions in EAS has been developed by [Cazon et al. (2012)] and can be exploited to reconstruct the MPD profile.

4.3.1 The muon time distributions model

Muons mainly come from the decay of pions and kaons and are produced with a characteristic transverse momentum distribution inside a narrow cylinder around the shower axis (for a 50 GeV pion, the muon deflection angle is about 2°).

Since the muon radiation length is much larger than the whole atmospheric depth, even in the case of inclined events, bremsstrahlung and pair production are improbable, and multiple scattering effects are negligible.

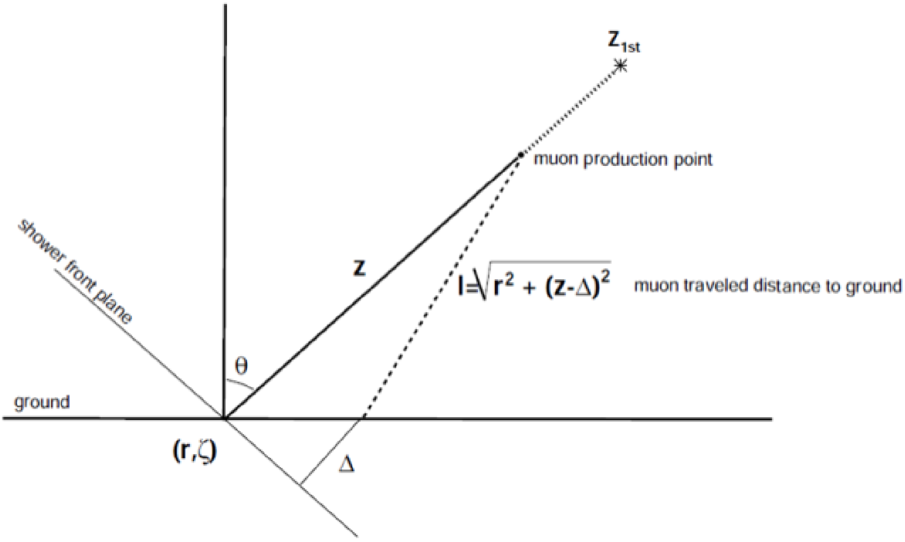

Figure 4.9: A scheme of the geometry used to obtain the muon geometrical delay with respect to the shower plane.

As a first approximation, muons are assumed to travel following straight lines, from the point where they are produced. The travelled distance is simply

$$l = \sqrt{r^2 + (z - \Delta)^2} \tag{4.18}$$

where Δ is the distance from the point at ground to the shower front plane, i.e. the plane front moving at the speed of light perpendicular to the shower axis, r is the distance at ground with respect to the shower core, and z is the muon production height (as shown in Figure 4.9).

The geometrical delay t_g is defined as the difference between the time that a muon spends to reach ground, and the time the shower front plane takes to reach the point of interest at ground:

$$ct_g = \sqrt{r^2 + (z - \Delta)^2} - (z - \Delta) \tag{4.19}$$

The delay can be approximated by

$$ct_g \approx \frac{r^2}{2(z - \Delta)} \tag{4.20}$$

when $z - \Delta >> r$.

Therefore, the geometrical delay results greater when muons are produced nearer to the ground and far from the core.

From equation 4.19, the production distance z is then given by:

$$z = \frac{1}{2}(\frac{r^2}{ct_g} - ct_g) + \Delta \tag{4.21}$$

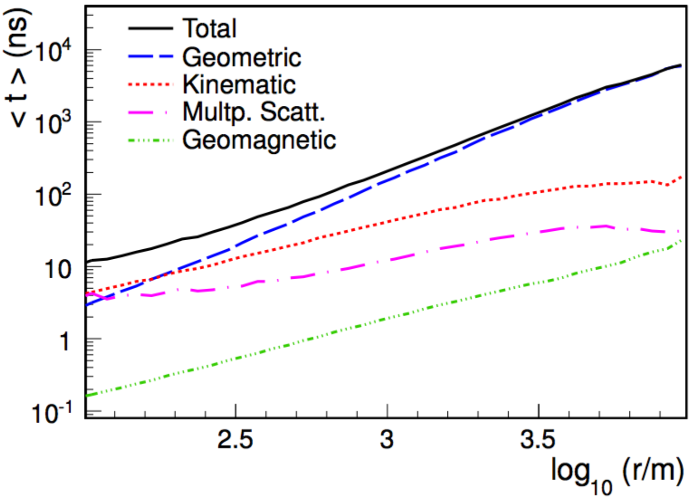

Figure 4.10: Average delays as a function of distance from the core for 10 EeV proton showers at 60°. The total delay and its contributions are shown [Aab et al. (2014)].

However, the measured muon delay is not due to the geometrical delay only. Indeed, muons do not travel at the speed of light and they loose energy on their way to ground, mainly because of inelastic collisions with atomic electrons in the air. Therefore, there will be a contribution to the total delay, called *kinematic delay*, due to the finite energy of muons. In order to estimate it, the muon energy has to be measured. Since such a measurement is not possible with SD detectors, a parametrization of the kinematic delay has to be studied.

The mean kinematic delay for a given z is

$$t_\epsilon = \frac{1}{2c}\frac{r^2}{l}\epsilon(r, z - \Delta) \tag{4.22}$$

where ϵ has been parametrized as follows:

$$\epsilon(r, z) = p_0(z)(\frac{r}{[m]})^{p_1} \tag{4.23}$$

To obtain this parametrization, the muon energy distributions have been modeled by means of several assumptions. All details can be found in [Cazon et al. (2012)].

Two other sources that contribute to the muon delay are the multiple scattering and the geomagnetic field, which deflect muons trajectories and whose contribution is of the order of a few percent.

The evolution of the total delay and its sources as a function of distance from the core is shown in Figure 4.10. As it is visible, all delays increase with distance r.

The geometrical delay dominates far from the shower core while the kinematic delay is larger near the core. Indeed, in this region the spread in muon energy is larger and the mean time delay is dominated by low-energy muons. At distances greater than 1000 m the kinematic delay is less than 30% of the geometrical delay, and this is effective for events with different zenith angles.

A correction which takes into account the path traveled by the parent mesons has also to be applied. Indeed, muons are not produced in the shower axis, but collinear with the trajectory followed by the parent pions. The muon path starts deeper in the atmosphere by an amount which is simply the decay length of the pion [Cazon et al. (2012)]:

$$z_\pi = ct_\pi E_\pi/(m_\pi c^2)cos\alpha \tag{4.24}$$

This correction introduces an average time delay of $\sim\ 3ns$.

Equation 4.21 becomes then:

$$z = \frac{1}{2}(\frac{r^2}{c(t-t_\epsilon)} - c(t-t_\epsilon)) + \Delta - z_\pi \tag{4.25}$$

where the geometrical delay has been approximated by $t_g = t - t_\epsilon$.

The equation above provides the muon production height z for each muon arrival time t at ground. The production depth X_μ, i.e. the total amount of traversed matter in g/cm^2, is obtained using

$$X_\mu = \int_z^\infty \rho(z')dz' \tag{4.26}$$

where ρ is the atmosphere density. The X_μ distribution is referred as MPD.

The MPD contains information about the longitudinal development of the hadronic cascade. In particular the MPD maximum, X^μ_{max}, is sensitive to the primary mass, as the maximum of the electromagnetic longitudinal profile measured with FD detectors.

4.3.2 The MPD analysis for inclined events

We have seen that the signal in SD stations results from a mixture of muons and electromagnetic particles. In order to reconstruct the muon production depth from SD signals, the electromagnetic component has to be removed.

One way to proceed is to consider only inclined events, for which the electromagnetic component is heavily absorbed by the atmosphere. In particular this analysis is performed for events with zenith angle between 55° and 65°.

The residual electromagnetic contamination can be removed by exploiting a simple threshold cut. Indeed, electromagnetic signals are broader in time and characterized by small amplitudes. A threshold S_{thr} equals to 15% of the maximum peak of the recorded signal allows to diminish the contamination and guarantees muon fractions above 85% regardless of the energy and mass of primary.

A selection on the range of distances from the shower core is also needed. Indeed, the time uncertainty of the detector, i.e. $\delta t = 25/\sqrt{12}\ ns$ translates into an uncertainty of the production distance z according to equation 4.21

$$\frac{\delta z}{z} \simeq -\frac{\delta t}{t} \simeq 2\frac{z}{r^2}c\delta t \tag{4.27}$$

By assuming an exponential atmospheric density, $\rho(z) = \rho_0 e^{-zcos\theta/h_0}$, the uncertainty in X_μ is then

$$\delta X_\mu = \frac{Xh_0}{cos\theta}\frac{2}{r^2}log^2\frac{Xcos\theta}{h_0\rho_0}c\delta t \tag{4.28}$$

where $h_0 = 7270$ m is the average height at which the first muon is produced, $\rho_0 = 1.24 \cdot 10^{-3} g\ cm^{-2}$ is the atmosphere density at that height and r is the distance from the core.

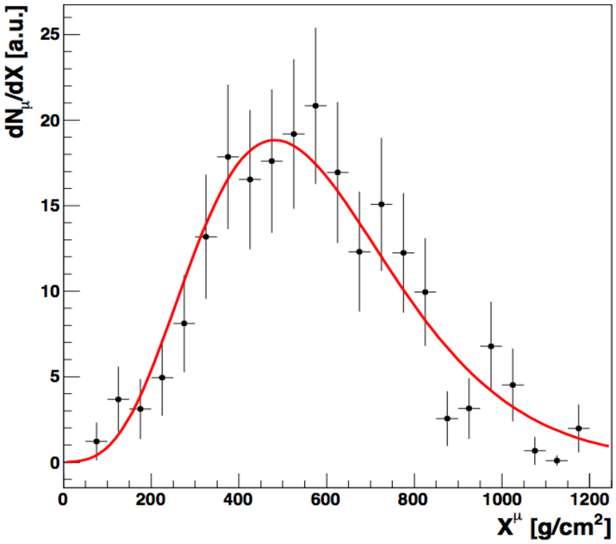

Figure 4.11: Real reconstructed MPD distribution at $E = (33 \pm 1) EeV$. The fit with a Gaisser-Hillas function is also shown [Aab et al. (2014)].

The uncertainty in X_μ decreases quadratically with r, and for a given zenith angle, is smaller far from the core.

On the contrary, the distance cut diminishes the efficiency of reconstruction and the resolution since it reduces the number of muons sample at ground. The selection of r_{cut} must thus be a compromise between the resolution of the reconstructed MPD and the selection bias. Using MC simulations, it has been found that $r_{cut} = 1700$ m is the optimal value, regardless of the shower energy.

Due to this cut, only events with energy greater than 20 EeV can be used in the analysis, in order to sample tens of muons at distances greater than 1700 m.

Another issue to be taken into account is that the light propagation inside the detector and the electronic response smears the muon arrival times. To compensate for this detector effect, a time offset t_{offset} has to be subtracted to each time bin. The offset value depends on S_{thr} and the optimal value, i.e. $t_{offset} = 73\ ns$, has been found by minimizing the reconstruction bias.

Finally, the MPD is obtained by adding the MPD distributions reconstructed in each detector. An example of real reconstructed MPD is shown in Figure 4.11.

The maximum X^μ_{max} of the MPD profile is obtained by fitting it with a Gaisser-Hillas function:

$$\frac{dN}{dX} = \frac{dN_{max}}{dX} \left(\frac{X - X_0}{X^\mu_{max} - X_0}\right)^{\frac{X^\mu_{max} - X_0}{\lambda}} \cdot e^{\frac{X^\mu_{max} - X}{\lambda}} \tag{4.29}$$

where X_0 and λ are shape parameters which do not have physical interpretation as the Gaisser-Hillas is a phenomenological function. Indeed, the preferred values for X_0 are generally negative. As hinted before, the number of collected muons is not large since only stations far from the core are used. This muon under-sampling does not allow to perform the fit leaving all parameters free and the parameter X_0 is thus fixed during the fitting procedure. X_0 depends on primary mass, and therefore the average value between proton and iron one is used: $X_0 = -45\ g/cm^2$.

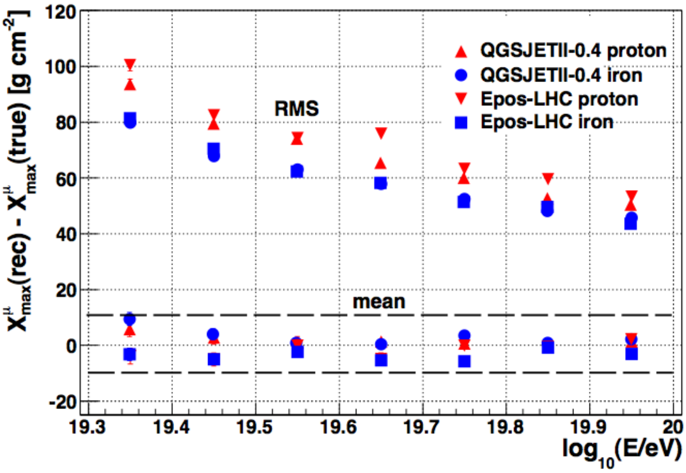

Figure 4.12: Evolution with energy of the mean and the RMS of the distribution $X^{\mu}_{max}(Rec) - X^{\mu}_{max}(MC)$ for events with zenith angle in the range $[55°, 65°]$ [Aab et al. (2014)].

Source	Systematic Uncertainty ($g\ cm^{-2}$)
Reconstruction + Hadronic model + Primary	10
Seasonal effects	12
Time Variance Model	5
Total	17

Table 4.1: The different contributions to systematic uncertainty in X^{μ}_{max}.

The reconstruction bias $X^{\mu}_{max}(Rec) - X^{\mu}_{max}(MC)$ and its RMS are shown in Figure 4.12. The mean bias is within 10 g/cm^2, regardless of the primary, the hadronic model and the energy. The resolution spans from 100 g/cm^2 at the lower energy to 50 g/cm^2 at the highest energies.

The systematic uncertainty and its sources are summarized in Table 4.1, while the measured X^{μ}_{max} is shown in Figure 4.13 as a function of the primary energy. The size of the error bars represents the standard deviation of the mean, while the brackets represent the systematic uncertainty.

While the evolution of X^{μ}_{max} with energy is similar for both QGSJetII-04 and EPOS-LHC, the absolute values of X^{μ}_{max} are considerably different. The evolution of X^{μ}_{max} with energy suggests a change in composition as the energy increases, from light to heavy. However, while Auger data are bracketed by QGSJetII-04, they fall below the Epos-LHC prediction for iron. As in the case of muon fraction analysis, the data are not well reproduced by simulations, and the study of the MPD profile is a further tool to constrain hadronic interaction models.

As for X_{max}, X^{μ}_{max} is correlated with the primary mass [1]. It is then possible to convert X^{μ}_{max} into $\langle lnA \rangle$ as explained in Section 4.1.2. Figure 4.14 shows the results obtained with QGSJetII-04 (left) and EPOS-LHC (right). While for QGSJetII-04 both measurements transform into coherent mass values, for Epos-LHC the results are incompatible,

---

[1] X_{max} and X^{μ}_{max} are strongly correlated, mainly by the depth of the first interaction

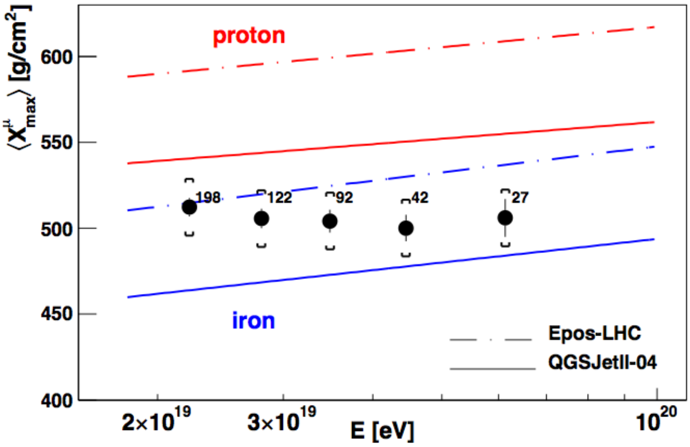

Figure 4.13: Evolution of the reconstructed $\langle X^{\mu}_{max} \langle$ with energy for events with zenith angle in the range $[55°, 65°]$.The predictions of QGSJetII-04 and EPOS-LHC for proton and iron showers are shown. Numbers indicate the number of events in each energy bin [Aab et al. (2014)].

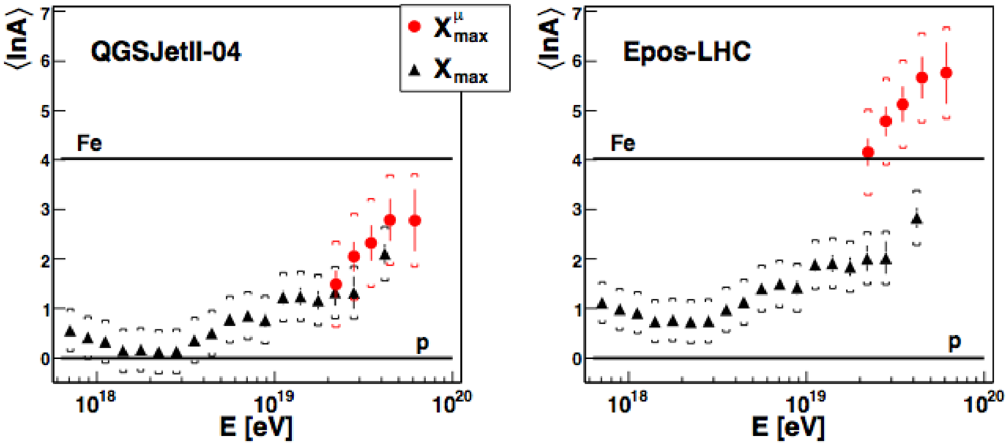

Figure 4.14: Conversion of $\langle X^{\mu}_{max} \rangle$ (circles) and $\langle X_{max} \rangle$ (triangles) to $\langle lnA \rangle$, as a function of energy. On the left (right) plot QGSJetII-04 (EPOS-LHC) is used as the reference hadronic model. Brackets correspond to the systematic uncertainties [Aab et al. (2014)].

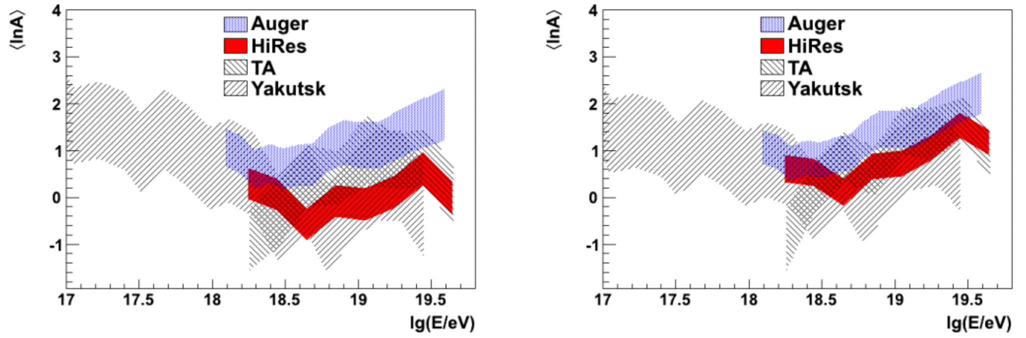

(a) using QGSJet-II model.

(b) using SIBYLL model.

Figure 4.15: Comparing the average composition $\langle lnA \rangle$ estimated using Auger, HiRes , TA and Yakutsk data. The shaded regions correspond to the systematic uncertainty ranges. To infer the average composition from $\langle X_{max} \rangle$, QGSJet-II and SIBYLL models have been used.[Barcikowski et al. (2013)].

predicting primaries heavier than iron nuclei ($lnA_{Fe} \approx 4$) in the case of X^{μ}_{max}. However, EPOS-LHC has been tuned to better represent the rapidity-gap distribution of proton-proton collisions at the LHC, compared to previous versions and to QGSJetII-04. Those changes translate into a deeper development of the muonic component, as seen in Figure 4.13, while the EM development is almost unchanged [Pierog (2013)]. Indeed, a modification in the elasticity has a relatively small effect on the electromagnetic development of the shower since only the first hadronic interaction is dominant. On the contrary, many hadronic interactions take place before the production of muons and thus there is a cumulative effect that shows up in the muon development.

4.4 Current status of the measurements of mass composition of UHECRs

As seen before, the small systematic uncertainties on X_{max} measurement makes it the most reliable source of information in composition studies at the Pierre Auger Observatory. Assuming that the modeling of hadronic interactions gives a fair representation of the actual processes in air showers at ultra-high energies, the results of FD data suggest a very light or mixed composition at around $10^{18.3}$ eV and a heavier composition (CNO or heavier nuclei) at higher energies, up to $10^{19.6}$ eV.

The results obtained with Auger can be compared to the ones achieved by other UHECRs experiments. Since the various detectors have very different selection cuts and systematic uncertainties, the most straightforward way to make sensible comparisons between experiments is inferring the average logarithmic mass, $\langle lnA \rangle$, from $\langle X_{max} \rangle$

$$\langle lnA \rangle = \frac{\langle X_{max} \rangle_p - \langle X_{max} \rangle_{data}}{\langle X_{max} \rangle_p - \langle X_{max} \rangle_{Fe}} ln56 \tag{4.30}$$

Only an un-biased measurement of $\langle X_{max} \rangle$ will correlate directly with $\langle lnA \rangle$. This is not the case for the measured $\langle X_{max} \rangle$ from HiRes and TA collaborations, since they do not apply field-of-view cuts. However, on a first approximation the biased $\langle X_{max} \rangle$ can

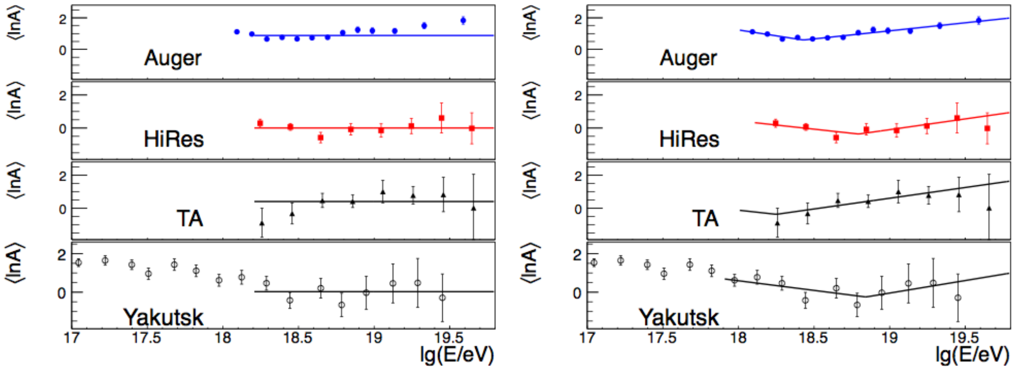

(a) Fit to a constant value.

(b) Fit to a broken line.

Figure 4.16: Evaluation of the average composition $\langle lnA \rangle$ estimated using SIBYLL as a function of energy. Two composition models are evaluated, a constant composition (as suggested by HiRes and TA) and a changing composition with a break (as suggested by Auger) [Barcikowski et al. (2013)].

be trasformed to $\langle lnA \rangle$ and it can be assessed whether all experiments yield compatible results [see Barcikowski et al. (2013) for details].

Figure 4.15 shows the $\langle lnA \rangle$ estimated with QGSJetII and SIBYLL, for Auger, TA [Jui et al. (2011)], HiRes [Abbasi et al. (2010)] and Yakutsk. The latter is a ground array experiment which measures charged particles at ground via 58 ground-based and 6 buried scintillation detectors and atmospheric Cherenkov light via 48 light detectors located above the ground ones. The experiment, located in Yakutsk (Russia), is operative since 1970 and it measures cosmic ray showers above 10^{15} eV. For details see [Berezhko & Knurenko & Ksenofontov (2012)].

At ultra-high energies, Auger data suggest a heavier composition than all other experiments. However, the results are consistent with TA and Yakutsk within uncertainties. There is some discrepancy between Auger and HiRes at the highest energies when QGSJET-II is used (Figure 4.15a), which almost disappears with SIBYLL (Figure 4.15b).

In order to establish if the different experiments are inferring the same composition scenario, i.e. a constant composition or a mixed composition, a fit to a constant and to a broken line can be performed [Barcikowski et al. (2013)].

Figure 4.16 shows the results for SIBYLL. All experiments obtain data that are consistent with a constant light composition, while Auger data clearly disfavour a constant composition scenario ($\chi^2/ndf = 137/10$ for the horizontal line fit). However, the Auger energy and $\langle lnA \rangle$ for the break point is not statistically compatible with the break points fitted by HiRes, TA or Yakutsk. Therefore further studies (exploring the effect of different interaction models) and more statistics in the Northern Hemisphere are required to establish the level of compatibility between Southern and Northern Hemispheres.

As we have seen in the previous sections, the Auger Collaboration has studied the mass composition by means of SD observables, as the risetime asymmetry (see Section 4.2.1) and the MPD (see Section 4.3.2). In this context, the Yakutsk collaboration uses an array of muon detectors to measure the muon signals at ground level. From these ground level observables, by means of MC simulations, it is possible to estimate $\langle lnA \rangle$. The results are shown in Figure 4.17. Despite some differences between measurements from Auger and Yakutsk, all observations suggest a trend to heavier composition above

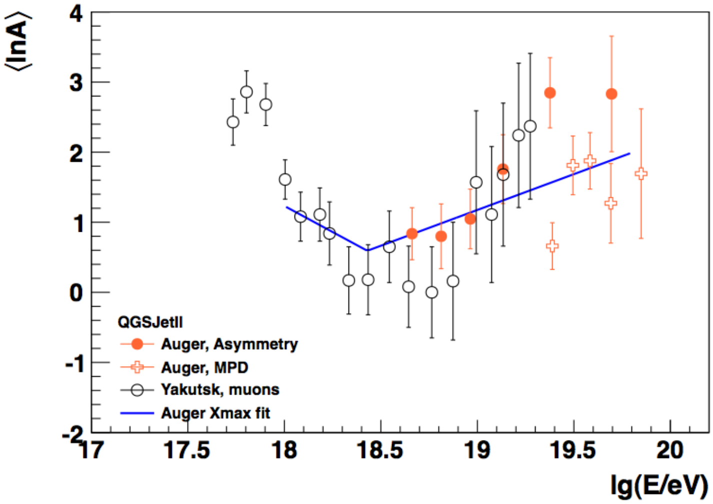

Figure 4.17: Average composition for ground level observables, using QGSJetII. The blue line is the fit to $\langle lnA \rangle$ obtained with Auger data using X_{max} [Barcikowski et al. (2013)]

$10^{18.5}$ eV. Measurements from Auger MPD only expand within a narrow energy range, and they do not provide much information regarding the evolution of the composition as a function of energy.

It is clear that the systematic differences between different type of measurements are very sensitive to the particular interaction model used for the interpretation. We have seen in Sections 4.2.2 and 4.2.3 that a muon deficit in the simulations has been pointed out by Auger data. Besides, the MPD analysis results, shown in Section 4.3.2, are difficult to accomodate with the description of EPOS-LHC. It is therefore of utmost importance to further constrain the hadronic models coming from accelerators in order to clarify the current picture.

CHAPTER 5

The Smoothing Method

The muon content of the showers is measured at the Pierre Auger Observatory in several ways:

- direct methods, either studying the temporal distribution of the total trace in the Surface Detectors or selecting horizonal showers, the latter being formed basically only by muons.
- indirect methods, either exploiting universality features of the showers or fitting individual hybrid events, in both cases relying on Monte Carlo simulations.

Indirect methods go beyond the aim of this thesis. For a detailed discussion of universality see [Schmidt et. al (2007)]. As regarding the hybrid events analysis, details can be found in Aab et al. (2013).

The direct methods have been already described in the previous chapter. In this chapter we will discuss in depth one of them, the smoothing technique, which exploits the different time distributions of muon and electromagnetic signals. We will show that the method can be optimized by using only one parameter directly linked to the measured signals and we will discuss the accuracy of the estimators of both the electromagnetic and muonic components as a function of different shower parameters, spanning the whole simulated ranges of primary energy, angle and mass for two different hadronic interaction models.

5.1 The smoothing

In order to separate the electromagnetic and the muonic components, many methods have been implemented, most of them relying on the different temporal structure of the FADC traces.

In particular the electromagnetic signal smoothly changes as a function of time, while the muon one is characterized by high narrow peaks (see Figure 5.1). Indeed the time distribution of the trace is related to the height of the shower development above the detecting surface while the signal structure depends on the energy with which particles hit the Cherenkov tank and on their number density. In the case of muons, the spread of arrival times at ground is narrow since, once produced, muons no longer interact and follow more or less a straight trajectory. Moreover, because of their low number density, and the high energy (about 1 GeV/muon at ground for UHECRs), muons produce peaked signals. On the contrary, elecromagnetic particles are a part of a cascade and the time spread at ground is large. Besides, the high number density together with a mean energy of about 10 MeV/particle give rise to smooth signals.

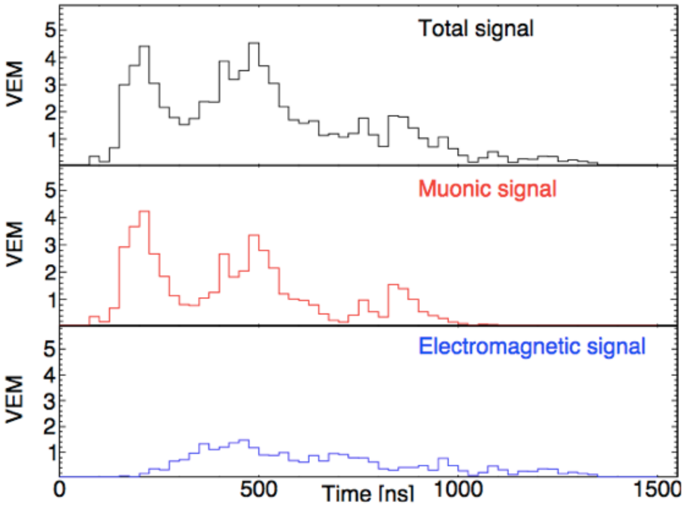

Figure 5.1: A typical example of FADC trace (top) and the different time structure of the muon signal (center) and the electromagnetic one (bottom) at 1000 m from the core. MC simulations.

These two kinds of signal can be separated by using a smoothing technique, which exploit the smoothed nature of the electromagnetic trace to extract it from the total trace of each tank.

Many kinds of smoothing techniques exist. One simple way of smoothing consists of using symmetric polynomial filters applied to equidistant measured steps [Dinnebier (2003)]. An interval, called convolute range, is moved stepwise through the pattern and the central point of the interval is replaced by the value of a least square polynomial calculated from the other points in the interval. When using a polynomial of first degree, this is just the so called moving average.

Moving average are the most common filters used in digital signal processing. It is easy to show that the smoothing through a moving average is equivalent to the convolution of the input signal with a kernel given by a rectangular pulse having unit area. Despite its simplicity, the moving average is most effective (and by the way the best filter) in the time domain, when the idea is to separate ”noise” from sharp steps.

In the frequency domain, this kind of filter is much less effective, having a slow step response and stop band attenuation and thus being a quite bad low pass filter.

As an illustration, the filter kernel (top) and the corresponding discrete Fourier transform (bottom) are shown in Figure 5.2 for a moving average window of 7 (left panel) or 15 (right panel) time bins, two windows which will be used in the following. The black curves correspond to filtering data only once, while the red ones are obtained with 4 iterations. The use of iterations produces a smooth step function and a multiplication of the frequency spectra. Considering a 40 MHz sampling as in the case of Auger, the frequency cuts (for 3 dB attenuation) go from 1.4 MHz for the 7 bins window case to 0.8 MHz when using 15 samples.

The procedure to derive the electromagnetic and the muonic component in a time interval T divided in N_{bin} equidistant bins is the following:

- the total signal $S_{tot}(i)$ in the i_{th} is averaged over 3 well behaving PMTs;

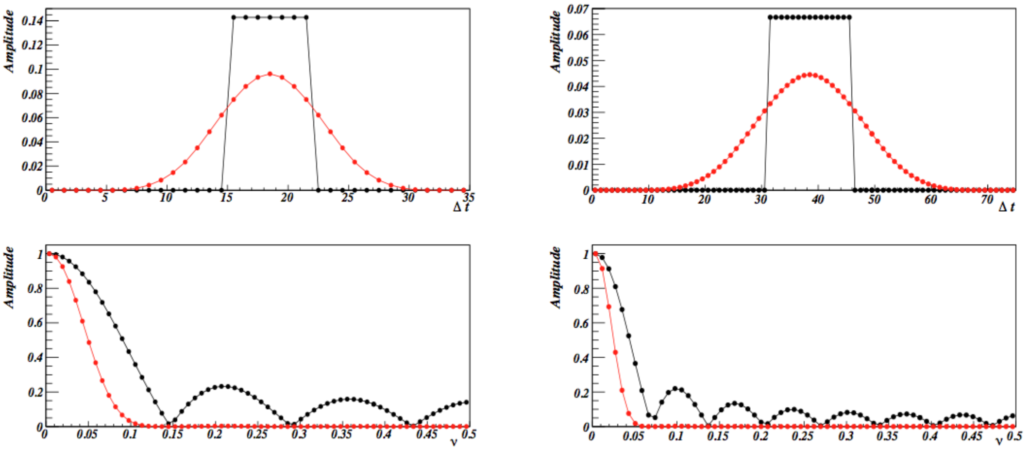

Figure 5.2: Top panels: filter kernel for an N points moving average filtered over data, either once (black) or 4 times (red); in the left panel, N=7, in the right one, N=15. Bottom plots: the corresponding DFT [Castellina & Collica (2012)].

- the smoothed trace is derived, by substituting each bin content with the average value $S_{tot}^{Smoo}(t_i) = \sum_k S_{tot}(t_k)/(2N_{bin}+1)$ with k running in the range $[i - N_{bin}, i + N_{bin}]$, and assigned to the electromagnetic component;
- the muon trace of the considered bin is given by the positive difference (if any) $S_{\mu}^{Smoo}(t_i) = [S_{tot}(t_i) - S_{tot}^{Smoo}(t_i)]$.

N_{bin} is the convolute range, which depends on zenith angle and will be discussed later. The procedure is repeated N_{iter} times: each time, the starting signal is the original one after subtraction of the non electromagnetic contribution obtained in the previous iteration. Finally

$$\begin{aligned} S_{EM}^{Smoo} &= \sum_k S_{EM}^{Smoo}(t_i) \\ S_{\mu}^{Smoo} &= \sum_k S_{\mu}^{Smoo}(t_i) \end{aligned} \tag{5.1}$$

Any contribution coming from the electromagnetic components is assumed to go to the smoothed trace. Therefore we have:

$$S_{EM}^{smoothed} = S_{EM}^{primary} + S_{EM}^{halo} \tag{5.2}$$

$$S_{nonEM}^{smoothed} = S_{\mu}^{primary} + S_{hadrons} \tag{5.3}$$

where S_{EM}^{halo} is the electromagnetic signal produced by the muon interactions and decay in the water Cherenkov tank and $S_{hadrons}$ is the hadronic signal from protons and neutrons; the fraction of the latter is always less than 2% in the angular and energy range considered here, as evaluated by means of Monte Carlo simulations (see Figure 5.3).

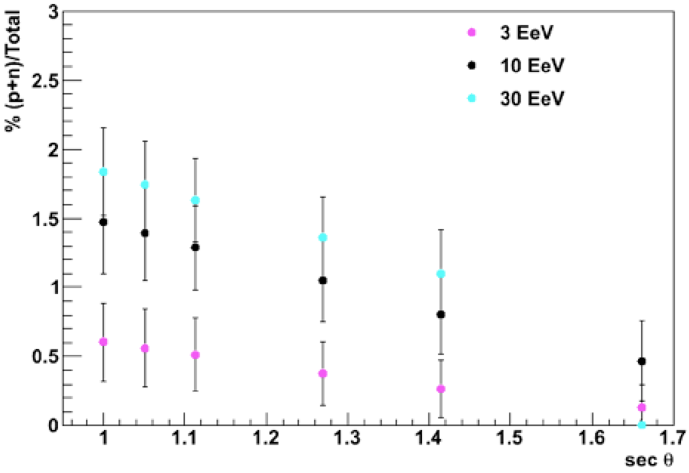

Figure 5.3: Fraction of hadrons with respect to the total signal. QGSJetII-03 simulations.

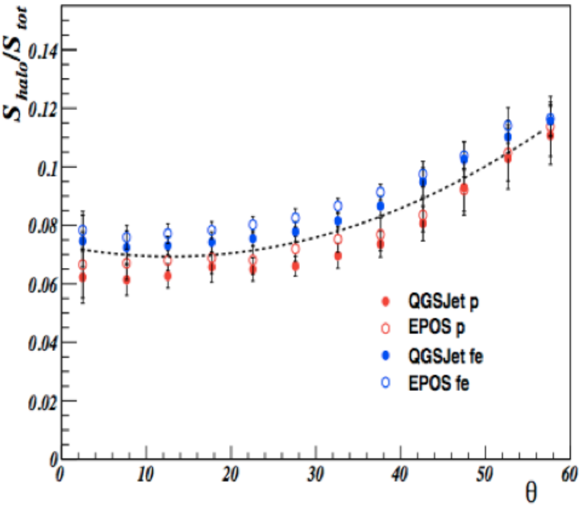

Figure 5.4: Halo from muons with respect to the total signal as a function of zenith angle [deg] for 10 EeV proton and iron showers in a station at 1000 m from the core, for different hadronic models.

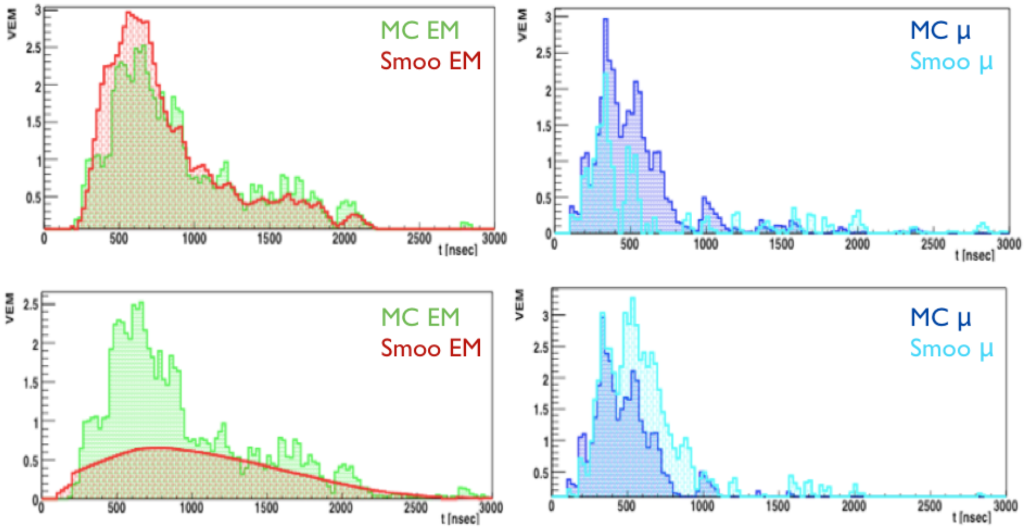

Figure 5.5: Example of smoothing in a single station when a too small (top row) and a too large (bottom row) convolute range is applied. Left column: EM component (in green the original simulated one, in red the result from smoothing); right column: the "non EM" component (in dark blue, the original one, in cyan the result from smoothing). Simulated proton shower: 10 EeV, 30°. [Castellina & Collica (2012)]

The halo signal is correlated to the muon one, since it is produced by muons. However with its smoother shape is for the most part embedded in the primary electromagnetic trace. Indeed, by performing the smoothing technique on the simulated halo trace we have found that about the 70% of the halo signal is "em-like".

Figure 5.4 shows the fraction of the halo signal with respect to the total one. The fraction increases with the zenith angle since in inclined showers the total signal is given mostly by muons.

5.2 Optimization of the convolute range

The method has been optimized using a library of QGSJetII-03 simulations: 15000 showers from proton and iron primaries were generated with CORSIKA [10] for an energy spectrum $\propto E^{-1}$ between 3 and 30 EeV and with an angular distribution up to 60° uniform in $cos^2(\theta)$. The Monte Carlo data were selected with the usual quality cuts applied to SD data: T5 events with at least one station at distance [950 m,1050 m] from the core are required, since the signal at this distance will be our observable to be related to the muon component. Indeed, as seen in Chapter 3, the optimal distance, at which the sum of the shower-to-shower fluctuations and of the statistical fluctuations from particle counting is minimum is 1000 m for the Auger Observatory.

The trigger efficiency is about 100% for both primaries above $10^{18.5}$ eV [Abraham et al. (2010)].

The convolute range has to be chosen with care. Indeed, as it is shown in Figure 5.5 a too small or too large convolute range can give rise to under or oversmoothing.

The choice of the optimal convolute range is driven by the variations of the electro-

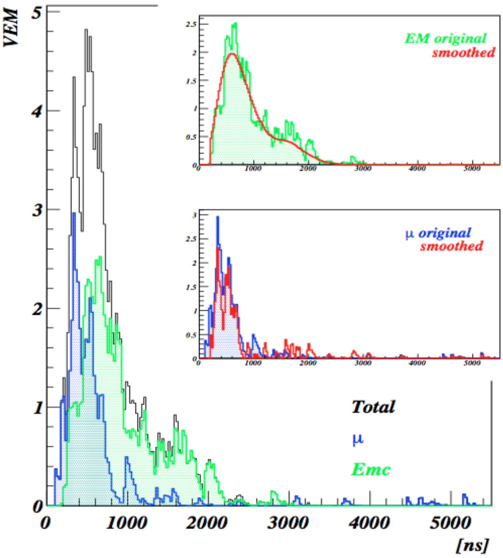

Figure 5.6: Signal in a station at 1 km from the core for a proton shower with 10 EeV.

magnetic and muonic component with air showers properties.

Indeed, considering the smoothing average in the frequency domain as a low pass filter, a large convolute range will be enough to follow the small electromagnetic signal in inclined showers. On the contrary, in vertical showers we will be able to estimate correctly the smoothed component with a narrow window only.

We decided then to use a variable smoothing range, obtained by minimizing the relative difference between the original electromagnetic signal from the simulation and the one obtained from the smoothing for each angle, in the whole range $0° - 60°$. The best fit is given by

$$N_{bin} = 7.27 + 0.14 \cdot \theta \tag{5.4}$$

for each zenith angle θ, this value is reduced to the nearest odd integer in order to use it as width of the moving average in the analysis.

Besides, the choice of the optimal convolute range depends on the bin width of FADC traces. The convolute range given above is tuned with the bin width of the standard water Cherenkov tank, i.e. 25 ns. With the fast electronic upgrade [1] the bin width will be 8 ns and a retuning of the convolute range must be done.

Finally, the smoothing filter converges to the best value after few iterations: the optimal number of iterations turned to be 4.

An example application of the smoothing technique is shown in Figure 5.6, where the temporal distribution of a trace in a station close to 1000 m from the core is shown, together with its components. In the inset, the two original components are compared to the result of the smoothing procedure.

---

[1] The Auger Collaboration is planning an upgrade of the SD electronics, as will be described in Chapter 9.

5.3 Evaluation of the physical background

We have seen that the smoothing technique assigns to the muon component any positive difference between the smoothed and the original trace. Therefore, the smoothing method efficiency is affected by fake spikes, either artificial of physical.

Artificial spikes have been studied in [Billoir (2008)] and they can be produced by the unthinning procedure: in fact, pile-up can arise if the resampled particles are assigned times which are different by less than the FADC sampling (25 ns) from one another. However, a smearing procedure is now applied at software level to make their presence negligible [Billoir (2008)].

The physical background is the most important and unavoidable, and can include accidental muons, hadrons, HE photons.

- atmospheric muons have a rate of about 2.5 kHz. In about 5 μs from the starting time of a trace, the probability that any one of the FADC bins contains an accidental muon is thus of the order of 1% and we can neglect them.

- the hadronic background is negligible since the average contribution to the total amplitude of the signal at 1 km from the shower core is below 0.1% for both iron and proton showers, arriving at ground with $\theta = 10 - 60°$ and about 2% and 1% when they arrive at ground with $\theta < 10°$ respectively.

- high energy EM particles, $E > 300\ MeV$, produce structures which are indistinguishable from those from true muons and generate an overestimation of the muonic component.

The last source of background is significant, and has to be quantified.

Some work has been devoted to determine the significance of electromagnetic spikes, by comparing the number of electromagnetic Spike Producing Particles (SPP) with the number of SPP from muons, which we call the Spike Producing Particles density:

$$SPP\ density = \frac{em\ SPP}{muon\ SPP} \tag{5.5}$$

In [Allen & Farrar (2009)] the SPP density in the case of 10 EeV proton showers with zenith angle of 26° for tanks at 1000 m from the core was studied by means of QGSJetII simulations and turned out to be about 10% in that particular conditions.

We followed the same approach to extend the evaluation of this background at different zenith angles, energies and distances from the core.

As SPP, we have taken muons with energy above 400 MeV and photons and electrons with energy above 300 MeV, since at these energies electrons and photons produce traces that are indistinguishable from those produced by muons.

In Figure 5.7, the SPP density is shown as a function of the zenith angle, for showers initiated by 10 EeV proton and iron primary, at 1000 m from the shower core. In order to increase the statistics, we have considered six zenith angle intervals in the range $[0°, 60°]$: the data points are given by the mean over each samples, with the corresponding statistical errors. The latter are given by $\sigma_{rms}/\sqrt{N}$, where N is the number of events.

The SPP density relative to proton is greater than the one relative to iron, at all zenith angles, since showers produced by iron primary are richer in muons. The SPP densities relative to iron and proton showers differs more for vertical events, while they are similar for inclined events. This is due to the fact that the EM SPP density decreases as the zenith

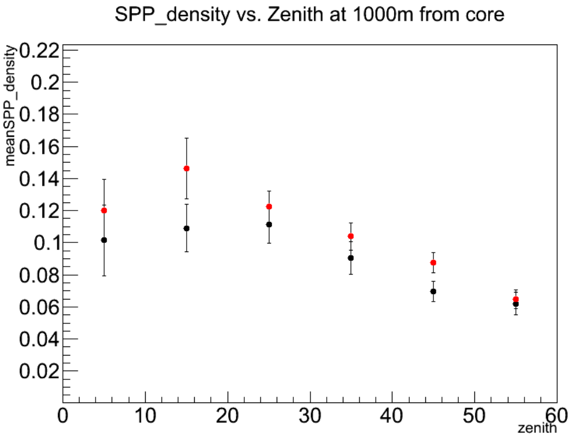

Figure 5.7: SPP density for 10 EeV proton (red) and iron (black) showers at 1000 m from core, as a function of zenith angle.

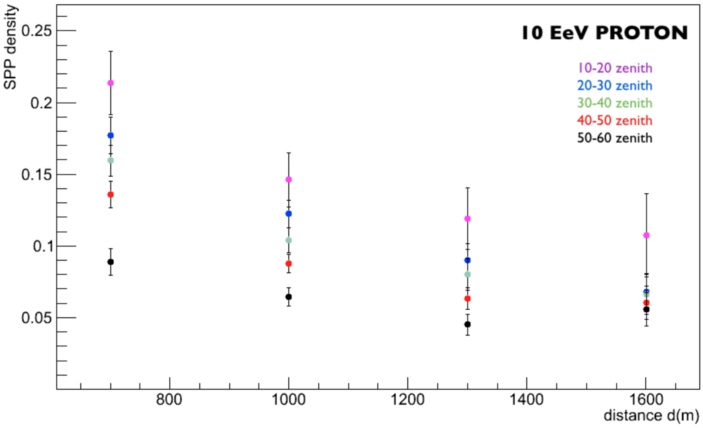

Figure 5.8: SPP density for 10 EeV proton showers as a function of distance from core for different zenith angles.

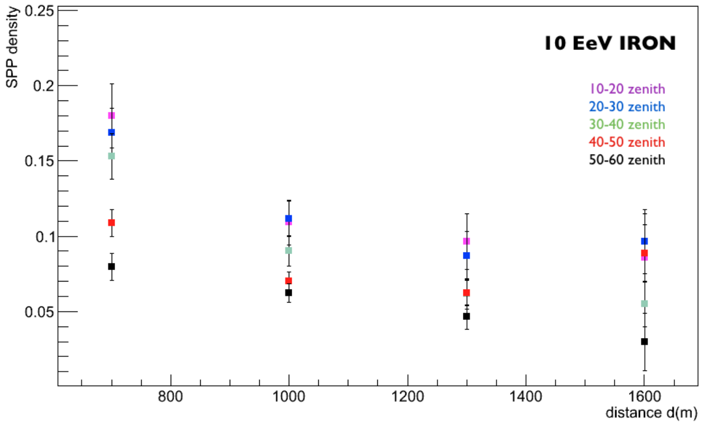

Figure 5.9: SPP density for 10 EeV iron showers as a function of distance from core for different zenith angles.

Zenith angle	proton primary	iron primary
5	0.120±0.019	0.102±0.022
15	0.146±0.019	0.110±0.015
25	0.122±0.010	0.111±0.012
35	0.104±0.008	0.090±0.010
45	0.087±0.006	0.070±0.006
55	0.065±0.006	0.062±0.007

Table 5.1: SPP density for 10 EeV proton and iron showers at different zenith angles, for stations near 1000 m from shower core.

angle increases because EM particles cross a longer pathlength in the atmosphere, and thus they are increasingly absorbed before reaching the ground.

In Figure 5.8 and 5.9 the SPP density is shown as a function of distance from the core, for different zenith angles, in the case of 10 EeV proton and iron primaries respectively.

Only zenith angles between 10° and 60° are considered because of the poor statistics for smaller angles. As expected, the SPP density decreases with distance, since the EM component is smaller as the distance from the core increases.

In Figure 5.10, the SPP density is shown as a function of the primary energy, for stations located at 1000 m from the shower core, and for events characterized by a zenith angle of 38° The horizontal bars represent the energy bins, while the vertical bars are the error bars, obtained as before. As before, the error bars increase as the energy increases because of the lack of statistics.

We can conclude that the electromagnetic SPP density is smaller than 15% and 12% for proton and iron showers respectively in the energy range between 10 and 25 EeV and for zenith angles from 20° to 60°, at 1000 m from the core. Since this background is present both in data and in Monte Carlo, an average correction to the estimated muon signal is applied.

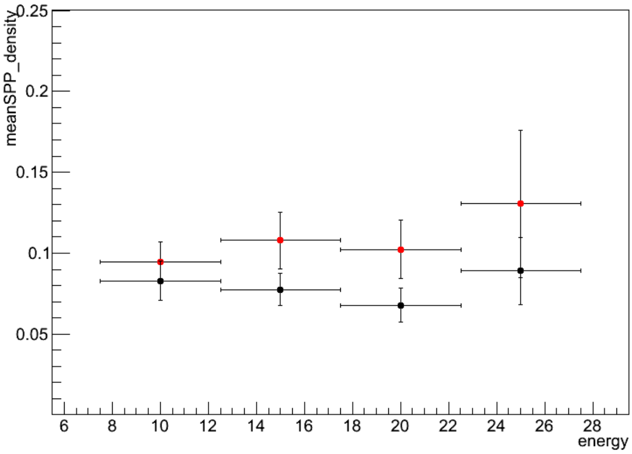

Figure 5.10: SPP density for proton (red) and iron (black) showers at 1000 m from core, as a function of primary energy (given in EeV), at 38°.

5.4 Method accuracy

The smoothing method accuracy has been studied by means of Monte Carlo simulations of showers from proton and iron primaries. All the results shown below are obtained with QGSJetII-03 simulations.

The relative difference between the simulated electromagnetic component S_{EM}^{MC} and the one estimated by applying the smoothing S_{EM}^{Smoo} is defined as

$$\Delta_{EM} = \frac{S_{EM}^{Smoo} - S_{EM}^{MC}}{S_{EM}^{MC}} \tag{5.6}$$

is shown in Figure 5.11 as a function of different shower parameters. Since S_{EM}^{Smoo} shown a small dependence with energy, a correction factor $\eta(E) = 1/(1 + \Delta_{EM})$ is introduced:

$$S_{EM}^{Smo} \rightarrow \eta(E) \cdot S_{EM}^{Smo} \tag{5.7}$$

$\eta(E)$ can be fitted as a function of the energy as $\eta(E_{FD}) = p_0 + p_1/\sqrt{(}E_{FD})$. The parameters p_i depends on the core distance, as shown in Figure 5.12.

The electromagnetic component is basically unbiased for stations in a range of core distances between 700 m and 1300 m, for both protons and iron showers. We see a bias above 1300 m and for zenith angle greater than $55°$, most probably due to a too small contribution of the electromagnetic component and to the increasing importance of the muonic one.

The muon signal estimated by the smoothing technique is not just a tracer of the total signal S_{tot} but it is correlated to the simulated muon signal, as it is shown in Figure 5.13.

However we can consider the muon signal relative to the total one in order to avoid

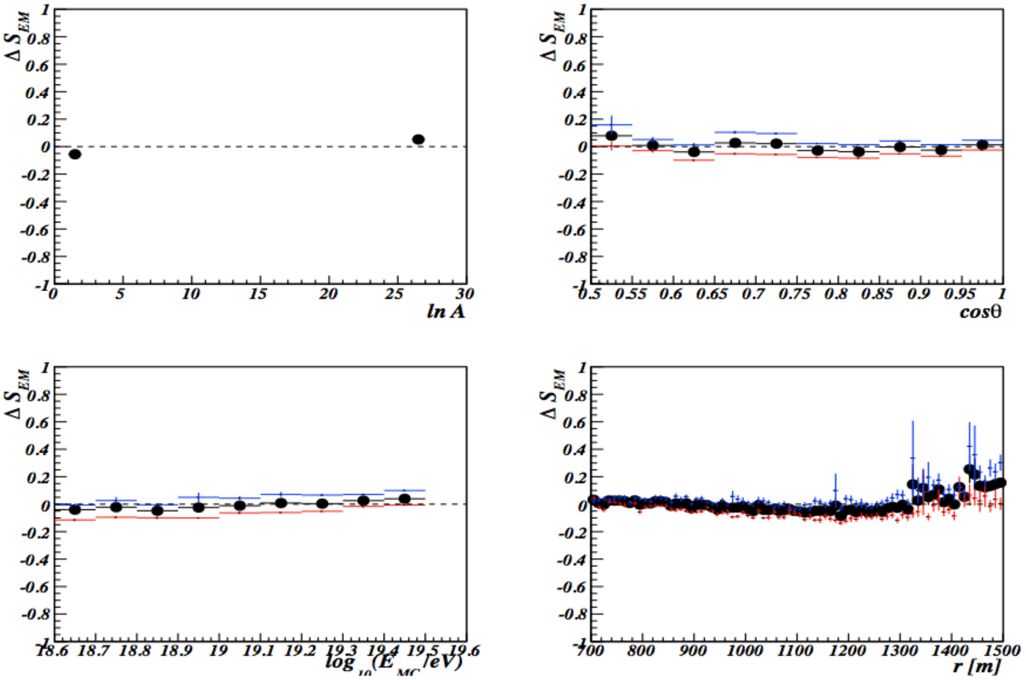

Figure 5.11: Relative difference between smoothed and original EM signals as a function of primary mass and zenith angle (top panels), input energy and core distance (bottom panels). Color code: red (proton showers), blue (iron showers). QGSJetII-03 simulations.

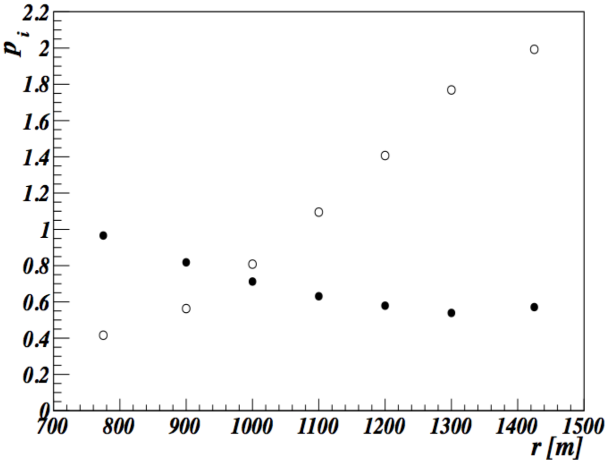

Figure 5.12: The parameters p_0(r) (full circles) and p_1(r) (empty circles) of the fuction $\eta(E)$ as a function of the core distance.

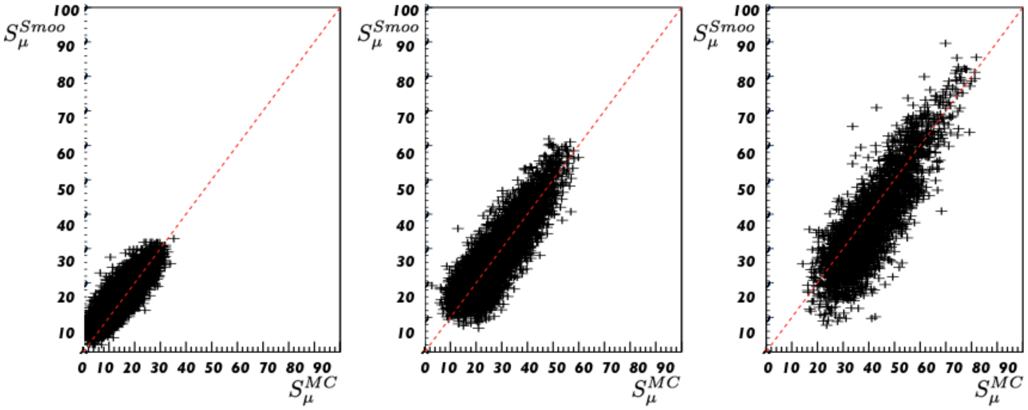

Figure 5.13: Estimated vs Monte Carlo muon component for different $\langle S_{tot}^{MC} \rangle$= 25, 60, 100 VEM for all stations between 700 and 1500 m from the core; the correlation factors are 0.91, 0.87, 0.85 respectively.

any residual rescaling. The evolution of

$$\Delta f_\mu = \frac{S_\mu^{Smo}}{S_{tot}} - \frac{S_\mu^{MC}}{S_{tot}} \tag{5.8}$$

with different shower parameters is shown in Figure 5.14. It results to be unbiased in the whole considered range of energies, distances and zenith angle independently of the primary mass.

Figure 5.15 shows the distribution of the relative difference between the estimated and simulated components at 1000 m from the core, for 10 EeV iron and proton showers. The difference between the estimated and original muon fraction is plotted in the rightmost panel of the same figure.

The estimates are unbiased, and in the case of the EM component their RMS is of the order of 17%, while they are larger for the muonic component where the spread reaches 21%. The widening in the estimation of the muon component for the proton case (the red points in the center plot) is due to the higher percentage of events in which $S_\mu^{MC}/S_{tot} \leq 0.3$ (about 11% for the proton events, 2% in the case of iron).

We also note that, as regards the resolution of single events, the systematic and statistical errors on the muon signal are smaller than the Poisson and shower to shower fluctuations. For example, at 10 EeV the muon signals at 1 km from the core show Poisson and shower to shower fluctuations of the order of 27% and 33% respectively for proton showers (and 23% and 27% for iron primaries).

5.4.1 The dependence on the hadronic model

It is important to check the dependence of the method on the hadronic interaction model. We therefore applied the method to a set of Monte Carlo simulations based on the EPOS 1.6 model.

Although not used anymore, this model produces a muon number much higher than the QGSJet one, thus allowing to look for the presence of systematic uncertainties in applying the smoothing technique to different models.

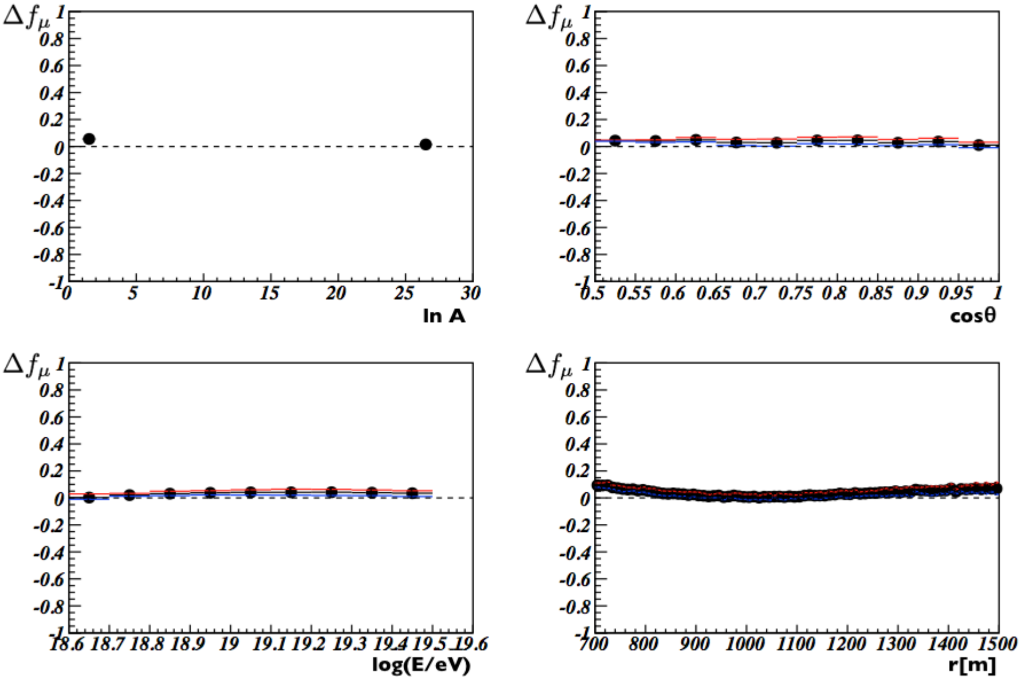

Figure 5.14: Difference between smoothed and original muon fraction as a function of primary mass and zenith angle (top panels), input energy and core distance (bottom panels) for QGSJetII-03. Color code: red (proton showers), blue (iron showers).

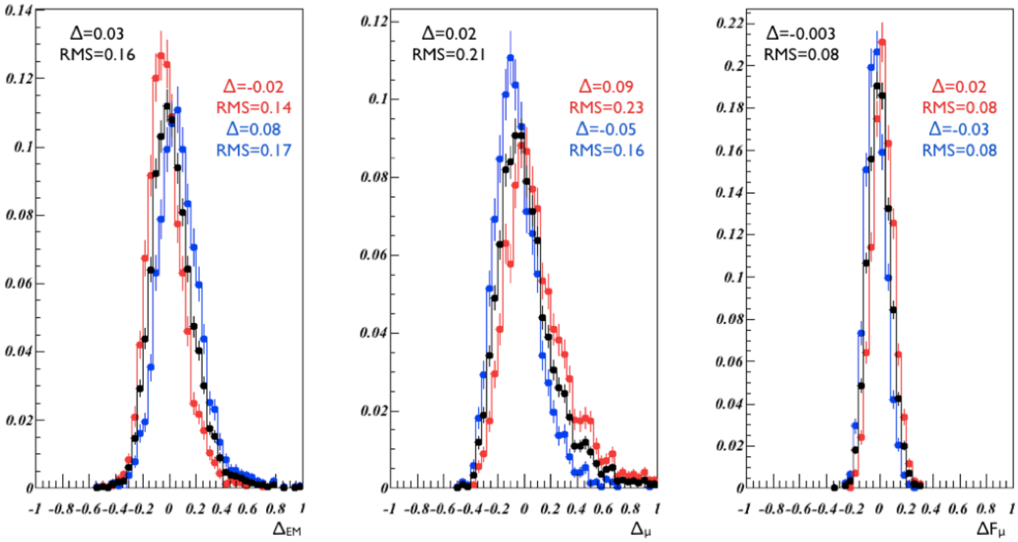

Figure 5.15: The relative difference between estimated and simulated EM (left) and μ (center) components at a core distance of 1 km, for primaries with 10 EeV energy. The difference between the estimated and original muon fractions is plotted in the rightmost panel. Same color code as previous figures.

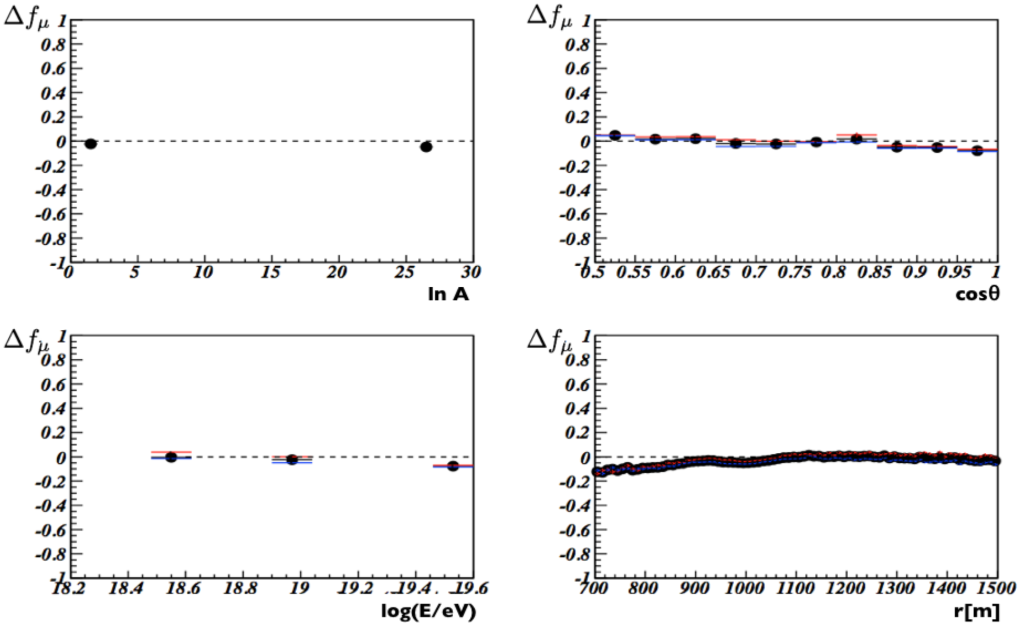

Figure 5.16: Difference between the smoothed and the original muon fraction as a function of the primary mass (top left), the zenith angle (top right), input energy (bottom left), core distance (bottom right) for EPOS-1.6.

In Figure 5.16, the difference between the smoothed and the original muon fraction is shown with respect to different shower parameters for the EPOS-1.6 showers. The systematic uncertainty due to the chosen hadronic interaction model stays below 10-15% considering the whole energy and angular range, and all stations between 700 and 1500 m from the core. The uncertainty lowers below 10% when the considered intervals are restricted.

The smoothing technique could thus be exploited to estimate the electromagnetic content of showers and, by difference, the muonic one. The method works in the region between 700 and 1500 m from the core, energies at least up to 30 EeV and zenith angles up to 60°. As seen in Section 4.2.2, the smoothing has been exploited together with the multivariate method to derive the fraction of the signal due to muons and to study the well known muon deficit appearing in the simulations of showers. The results obtained with the two techniques are in very good agreement, and the smoothing has demonstrated to be a robust method to evaluate the muon signals in WCD.

We will show in Chapter 7 that the method can be used to estimate the time distribution of the muon signal in a wider range of energies and distances from the core, thus allowing to extend the MPD analysis range.

CHAPTER 6

Extension of the Muon Production Depth Analysis: MC studies

In Section 4.3 we have discussed the reconstruction of the Muon Production Depth for inclined events and the interpretation of the results in terms of mass composition.

As shown, the standard analysis is limited to high energy inclined events and the reconstruction is performed far from the core, i.e. $r > 1700\ m$, because of the electromagnetic contamination and the detector effects. Indeed the former is removed through a simple threshold cut while the detector response to muons is taken into account only on average [Aab et al. (2014)].

In order to extend the analysis range to lower energy and zenith angle ranges, it is thus necessary to find a method able to efficiently estimate the electromagnetic component and correct for the detector effects. Besides, once that these two issues are solved, it would be worth performing the analysis closer to the core, in order to increase the muon statistics.

Before investigating the extension of the MPD reconstruction with SD detectors, we studied the MPD profile properties without the detector reconstruction, in order to define the explorable ranges in energy, zenith angle and distance from the core.

6.1 The apparent MPD profile: reconstruction limit at ground

The *true* MPD profile, i.e. the one relative to all muons produced in air showers, cannot be reconstructed at ground level since part of them will be absorbed when reaching ground.

The *apparent* MPD profile is instead the one regarding those muons that reach the ground and can be reconstructed using the SD. From now on, we will always refer to the apparent profile.

We have studied the MPD properties on different MC simulations, and the summary of the considered hadronic models and the relative statistics are given in Table 6.1.

	QGSJetII-03 p — Fe	QGSJetII-04 p — Fe	EPOS-LHC p — Fe
energy range	10-30 EeV	10-100 EeV	10-100 EeV
angular range (deg)	$0° - 65°$	$45° - 65°$	$45° - 65°$
events	4500 (0-40)	800 (45-55)	800 (45-55)
events	5000 (40-65)	5200 (55-65)	5200 (55-65)

Table 6.1: Simulation libraries used for the CORSIKA studies.

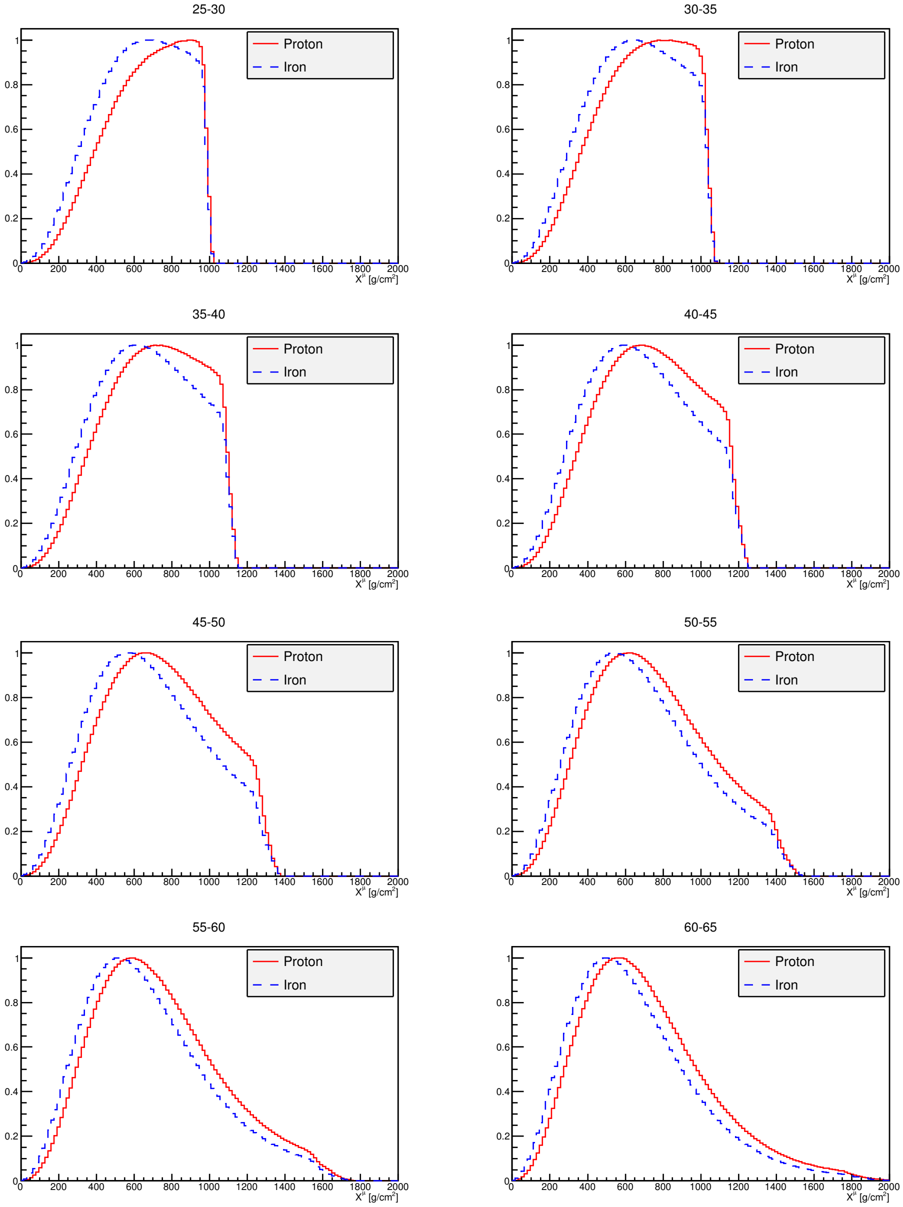

Figure 6.1: The average MPD profiles of 20-30 EeV proton (red line) and iron (blue dotted line) showers for zenith angle between 25° and 65° in bins of 5° from top left to bottom right. All muons reaching the ground are taken into account. QGSJetII-03 simulations.

Muon production in EAS is mostly due to charged pions decay, as seen in Chapter 2. The critical energy of $\pi^{\pm}$ depends on the atmospheric density: the decay probability of $\pi^{\pm}$ is greater than the interaction one when air density is low.

The MPD profile thus depends on the zenith angle of the shower: inclined events develop at higher depths than vertical one since the average density seen by the former is smaller.

Figure 6.1 shows the average apparent MPD profiles for events induced by protons and iron nuclei, in different zenith angle ranges. The muon production depth is directly given in CORSIKA from the position of the muon production point. While at high zenith angles the MPD profile is well defined, at low angles it undergoes an abrupt truncation since the shower arrives at ground [1] before reaching the shower maximum, X^{μ}_{max}. This is especially true for protons, whose showers develop deeper in the atmosphere with respect to iron ones.

We thus focuse the analysis on events with zenith angle greater than $40°$, for which the profile maximum is well defined for both primaries on an event-by-event basis.

As seen in Section 4.3.1, the time model algorithm estimates the muon production depth from the arrival time of muons at ground and it takes into account the finite muon energy by including the kinematic delay t_{ϵ}, which acts like a correction far from the core.

Since the t_{ϵ} parametrization has been done by assuming a given muon energy spectrum at ground and tuned on an old hadronic model, it is the greater source of uncertainty in the model and it is thus better to keep its contribution below 20%. In particular, while at 500 m from the shower core t_{ϵ} is comparable to the geometrical delay t_{geo}, at 1200 m t_{ϵ} is about 20% of t_{geo} (see Figure 4.10). This is true not only for inclined showers, but also for vertical ones. Therefore a cut on the core distance at 1200 m is introduced. Moreover, we will consider only muons reaching ground in the distance range [1200, 4000 m] since in the reconstruction with SD we will not have triggered stations farther than 4000 m from the core. For simplicity, we will refer to the cut $r_{cut} > 1200\, m$, implying the upper cut at 4000 m.

The cut in distance affects the MPD profile shape since all muons that arrive close to the core are cut off.

Figure 6.2 shows the effect of the cut on the MPD profile for different zenith angles. In particular the distance cut suppresses the tail of the profile, since the latter is mostly populated by low energy muons produced close to ground which arrive near the core.

The distance dependence is stronger for vertical events which develop deeper in the atmosphere: while at $55° - 60°$ of zenith angle the position of the maximum is not altered and the shape is only slightly distorted, at lower angles the MPD profile tail is highly suppressed and the muon maximum is "shifted" towards smaller depths.

It is therefore necessary to compare the reconstructed maximum to the simulated one in the same measurements conditions, i.e. same distance, energy and zenith angle range.

6.2 Universal Shower Profile Function

The muonic shower maximum can be estimated by a fit to the whole profile. A simple Gaisser-Hillas function was extensively used in the past; however, the non symmetric shape of the longitudinal profile is found to be more precisely described by the Universal Shower Profile function, as studied in [Cazon et al. (2012)].

This function has three free parameters, all related to the physics of the shower: the maximum of the profile X^{μ}_{max}, the profile width L and a parameter related to the distri-

---

[1] the ground level simulated is the Pierre Auger Observatory one

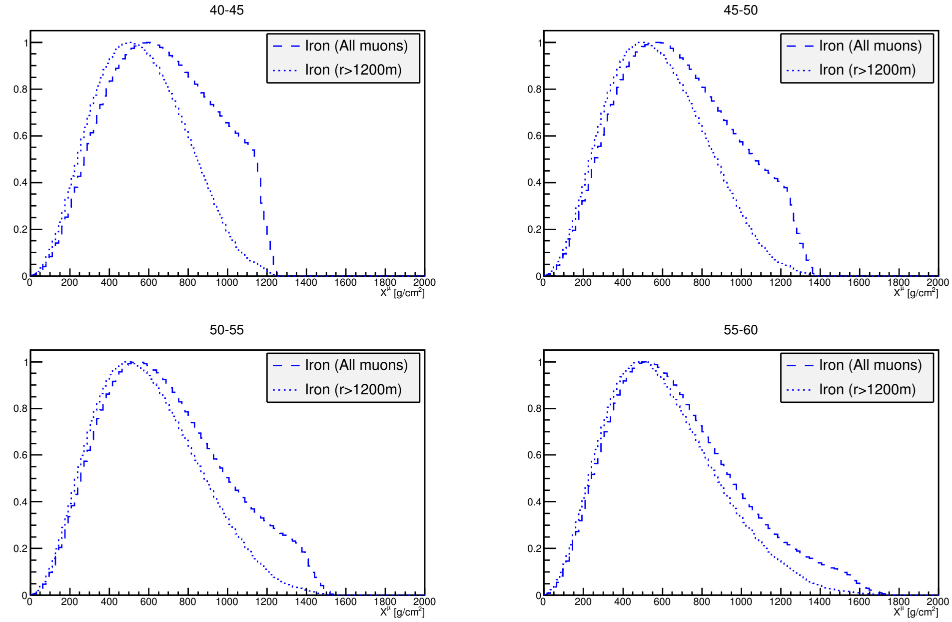

Figure 6.2: The average MPD shape for the apparent profile without any distance cut (broken line) and for the apparent one considering only muons reaching groud at a distance greater than 1200 m (dotted line). Four zenith angle bins are considered here: $40^\circ - 45^\circ$ (top-left), $45^\circ - 50^\circ$ (top-right), $50^\circ - 55^\circ$ (bottom-left), $55^\circ - 60^\circ$ (bottom-right). 20-30 EeV iron showers. QGSJet03 simulations.

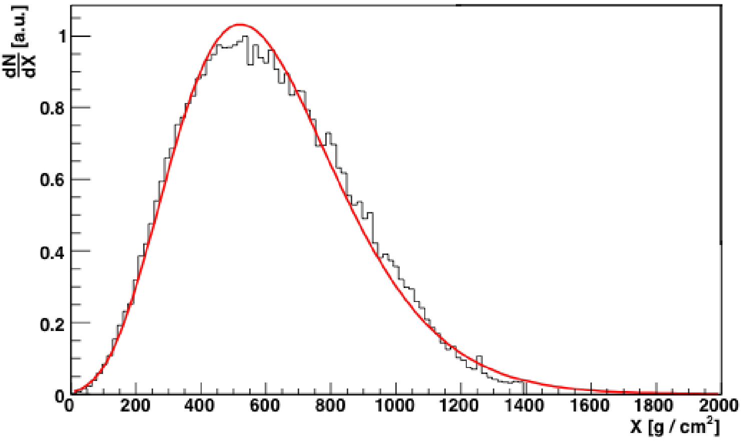

Figure 6.3: An example of MPD profile fitted with the USP function. Iron shower with a zenith angle of 50°.

bution asymmetry, R, which quantifies the deformation of the profile with respect to a Gaussian distribution.

The USP function is defined as:

$$\frac{dN}{dX} = (1 + \frac{R}{L}(X - X^{\mu}_{max}))^{R^{-2}} \cdot e^{-\frac{X - X^{\mu}_{max}}{LR}} \tag{6.1}$$

and an example of the MPD profile fitted with USP function is shown in Figure 6.3.

The USP fit is performed leaving all parameters free, and requiring that all of them be positive.

The full sample of simulated proton and iron showers with the QGSJetII-03 model was used to study the evolution of the parameters L and R as a function of zenith angle. The result is shown in Figure 6.4, for the apparent MPD profiles with and without the distance cut. As expected, the parameters L and R obtained in the two cases show a different behaviour. When the profile is reconstructed taking into account all the muons reaching ground, R results to be almost flat with zenith angle, while L decreases with it since the profile becomes narrower as the zenith angle increases (see Figure 6.1).

On the contrary, when the profile is reconstructed farther from the core, both L and R decrease with zenith angle θ. Indeed, as θ decreases a greater part of the tail is cut away, making the profile more symmetric and narrower.

Accordingly, it is not possible to fix one parameter to a single value in the whole zenith angle range. Furthermore, we found after several tests that the fit performance is better if all parameters are left free and no boundary limits are imposed.

6.3 The apparent MPD profile: dependence on primary zenith angle and energy

As seen in a qualitative way previously, the MPD profile maximum depends on zenith angle and the distance cut affects its position.

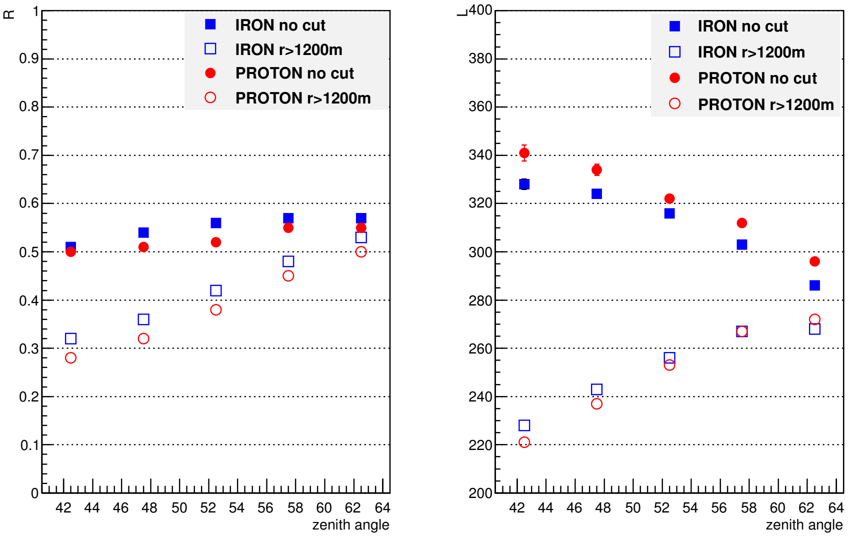

Figure 6.4: The L (left) and R (right) parameters are plotted as a function of the zenith angle for both primaries, with and witout the distance cut. E=20-30 EeV, QGSJetII-03 simulations.

Once that the MPD maximum X^{μ}_{max} is estimated by fitting the profile with the USP function, we can study its evolution with the zenith angle and the primary energy.

Figure 6.5 (top) shows the evolution of X^{μ}_{max} with the zenith angle with and without the distance cut. When the distance cut is applied, the maximum is underestimated for both proton and iron primaries, especially at low zenith angles. It is also notable that the distance cut strongly reduces the zenith angle dependence.

Another important observable sensitive to mass is the RMS of X^{μ}_{max} distribution.

Indeed shower-to-shower fluctuations are smaller for heavy primaries (as seen in Chapter 4) and this property can be exploited to infer additional information about the primary mass.

Figure 6.5(bottom) shows the evolution of RMS(X^{μ}_{max}) with the zenith angle with and without the distance cut. The distance cut affects the RMS of X^{μ}_{max} distribution as well since it makes the profile more gaussian, reducing the uncertainty in the maximum estimation. The effect is stronger in the case of proton showers, for which shower-to-shower fluctuations are greater, and for lower zenith angles where the effect of the distance cut is greatest.

The MPD maximum X^{μ}_{max} depends also on energy, as shown in Figure 6.6 (top). The distance cut makes the maximum smaller but does not affect the energy dependence. Indeed in both cases the maximum increases with the logarithm of energy, as expected from the Heitler model.

The evolution of RMS(X^{μ}_{max}) with energy with and without the distance cut is shown in Figure 6.6(bottom). The distance cut makes the RMS smaller but, differently to the maximum, the RMS does not strongly depend on energy.

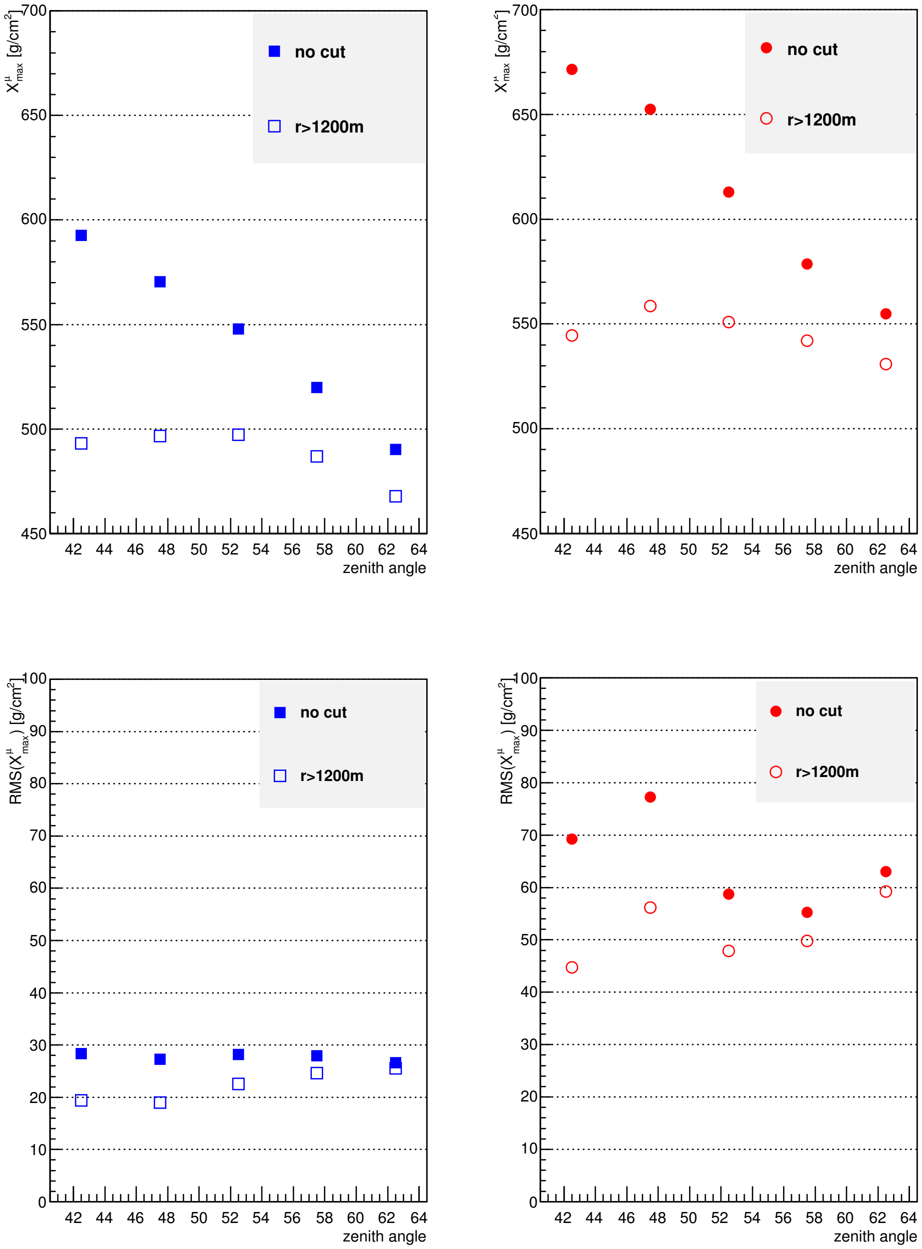

Figure 6.5: X^{μ}_{max} (top) and RMS(X^{μ}_{max}) (bottom) as a function of zenith angle for MPD profile with and without the distance cut ($r > 1200\ m$): *left*) 20-30 EeV iron showers, *right*) 20-30 EeV proton showers. QGSJet03 simulations.

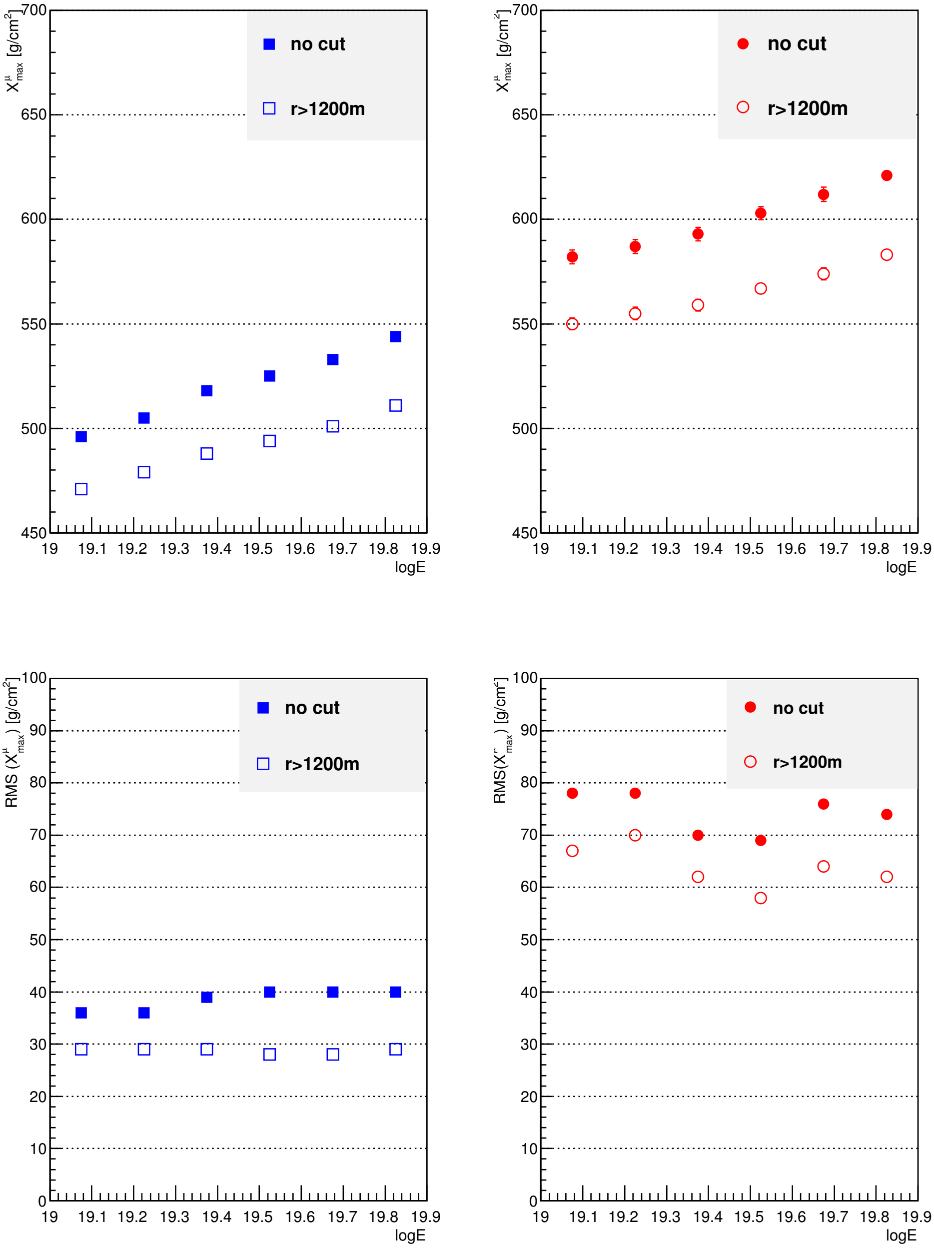

Figure 6.6: X^{μ}_{max} (top) and RMS(X^{μ}_{max}) (bottom) as a function of primary energy for MPD profile with and without the distance cut: *left*) iron showers, *right*) proton showers, with zenith angle between 45° and 65°. QGSJet04 simulations.

6.4 The apparent MPD profile: dependence on hadronic models

The cross sections which characterize the hadronic showers produced by UHECRs are not known with precision, since such energies are inaccessible to nowadays accelerators. Moreover, our knowledge concerns p-p interactions in the center of mass system, instead of p-nucleus or nucleus-nucleus (where the nucleus is the target) which are the ones of interest in cosmic rays physics.

The predictions of EAS simulations are thus affected by systematic uncertainties related to the model used to describe ultra-high energy interactions. The maximum explored energy today reaches about 10^{17} eV in the case of p-p. The heavy nuclei interactions are studied at much lower energies (one to two orders of magnitude less).

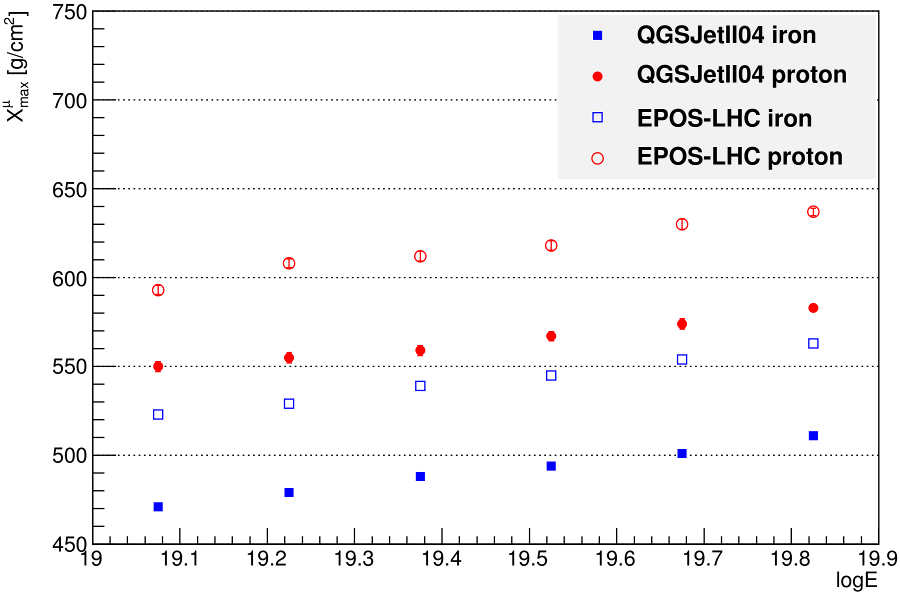

Figure 6.7: X^{μ}_{max} as a function of logE for the two different primaries and hadronic models.

Since muons come from the decay of pions and kaons, the MPD profile contains informations about the evolution of the hadronic cascade. We thus expect that the maximum and its RMS will depend on the hadronic interaction models used in EAS simulations.

Figure 6.7 and Figure 6.8 show the evolution of X^{μ}_{max} and RMS(X^{μ}_{max}) with energy for iron and proton primaries, in the case of the two most recent hadronic models: QGSJetII-04 and EPOS-LHC. These models do not assume new physics effects in hadronic interactions and are based on cross-sections extrapolated from LHC data (see Section 2.2). The two models predict a similar muonic elongation rate but show considerable differences in the absolute value of X^{μ}_{max}. Indeed the difference in $\langle X^{\mu}_{max} \rangle$ is almost comparable to the expected one from proton-iron separation.

On the contrary, the two models predict similar value of RMS(X^{μ}_{max}), and the same evolution with energy. Therefore, the RMS is an optimal observable to study the primary mass, since it does not strongly depend on hadronic models. However, in order to ex-

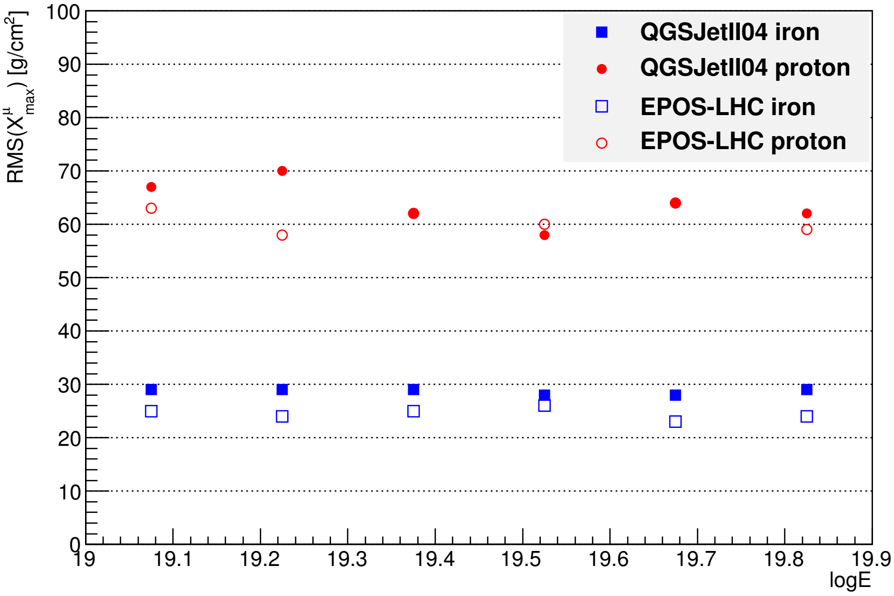

Figure 6.8: RMS(X^{μ}_{max}) as a function of logE for the two different primaries and hadronic models.

ploit it as a mass composition observable, the whole MPD profile must be reconstructed correctly.

The reconstruction of the MPD profile at ground is thus a useful tool to constrain hadronic interaction models, besides giving informations about the mass of primary particles.

In the following chapters we will see how to reconstruct the MPD with the SD in the distance and zenith angle ranges discussed above, and the issues which has to be addressed.

CHAPTER 7

Extension of the Muon Production Depth Analysis: SD reconstruction

In Chapter 6 we have discussed the MPD reconstruction limits related to the shower physics and to the muon time distribution model. In particular, we have seen that the reconstruction at ground has to be performed for events with zenith angle greater than 40° and that the time model has to be exploited with stations far from the shower core.

The two main problems related to the extension of the analysis to lower zenith angles and energies are the distortion induced on the MPD profile by the detector effects, i.e. muon arrival times are smeared by light propagation inside the detector and the electronics response, and the electromagnetic contamination.

New analyses have been performed within the Auger Collaboration, based on an average subtraction of the electromagnetic component and the correction of the muon production depth distortion based on MC simulations and they give promising results [Zamorano (2014)].

Another possible approach is to combine the smoothing method, which estimates the electromagnetic component from the total signal as discussed in depth in Chapter 5, with a deconvolution algorithm, which as we will show is able to correct for the detector effects. This approach allows to correctly reconstruct the MPD profile in a wide zenith angle and energy range and has the advantage of being free of MC-based corrections.

	QGSJetII03 p — Fe	QGSJetII04 p — Fe	EPOS-LHC p — Fe
energy range	10-30 EeV	10-100 EeV	10-100 EeV
angular range	$40° - 60°$	$45° - 60°$	$45° - 60°$
events	17500	9600	9500

Table 7.1: Simulation libraries used for the interaction models.

The MPD reconstruction can be done on an event-by-event basis only for energies greater than 10 EeV, such that tens of muons or more are collected and the muon longitudinal profile is reconstructed well.

We have tuned the method using iron and proton shower simulations with energies between 10 and 100 EeV and zenith angle between 40° and 60°. The smoothing method has been studied in depth in the considered zenith angle range while it has never been tested at energies greater than 30 EeV. It will thus be necessary to study its performance in the whole energy range.

In order to test the method on different hadronic interaction models, we have performed the analysis on simulations based on QGSJetII-03, QGSJetII-04 and EPOS-LHC (see Table 7.1 for details). The simulations used are the one exploited to study the MPD properties in Chapter 6, but with the addition of the SD array simulation implemented in the Offline Sofware [Argiro et al. (2007)].

In the following sections we will discuss the detector effects and the electromagnetic contamination treatment. Then we will present the method accuracy and the different contributions to the total resolution.

7.1 Detector Effects and Electromagnetic contamination

As shown in Section 4.3.2, it is possible to reconstruct the MPD profile from the signals recorded in each station. Until now, the Auger Collaboration has performed the MPD analysis for inclined events (zenith angle in the range $[55^\circ, 65^\circ]$), for which only stations far from the core are used. Indeed for large zenith angles (above 55°) the signal in each station is basically due to muons only and the residual EM component can be removed with a simple threshold cut. In order to increase the event statistics, an extension of the analysis to a wider angular region is required, and the study of methods to separate EM and muon components must be done.

If the reconstruction is performed for lower zenith angles, two issues arise:

- detector effects, mostly due to the discrete sampling at ground and the detector response to muons.
- separation of the electromagnetic and muonic component.

In order to investigate the first issue, we consider the ideal case: the MPD reconstruction with the Monte Carlo muon traces. Then, we will discuss the problem of the electromagnetic contamination and the method through which it can be estimated and subtracted.

7.1.1 The Gold Deconvolution Algorithm

As indicated above, the detector response to muons introduces a distortion in the shape, more and more important as the zenith angle increases.

As an illustrative example, the mean MPD profile reconstructed using the simulated muon traces of stations from 1200 m is shown in Figure 7.1 (red dotted line), together with the simulated MPD profile in the same distance range from the core (black solid line). The reconstructed profile is distorted with respect to the simulated one, in all zenith angle bins. The distortion is due to the station response to muons: the typical width of a muon signal is larger than a single time bin and this causes an uncertainty in the arrival time of muons.

Indeed, the photoelectrons produced by muons and electrons arrive on the photomultiplier tube according to an exponential law in time. This law reflects the attenuation in water and the multiple reflections off the Tyvek. From experimental measurements of the tank response [Castellina & Navarra (2006)], the light decay time results to be about 65 ns in the case of muon signals, as shown in Figure 7.2.

The measured signal S_μ^{meas} is the result of the convolution of the true signal S_μ^{true} with the detector response $R(\tau)$:

$$S_\mu^{meas}(t) = \int S_\mu^{true}(\tau) \times R(t-\tau)\, d\tau \tag{7.1}$$

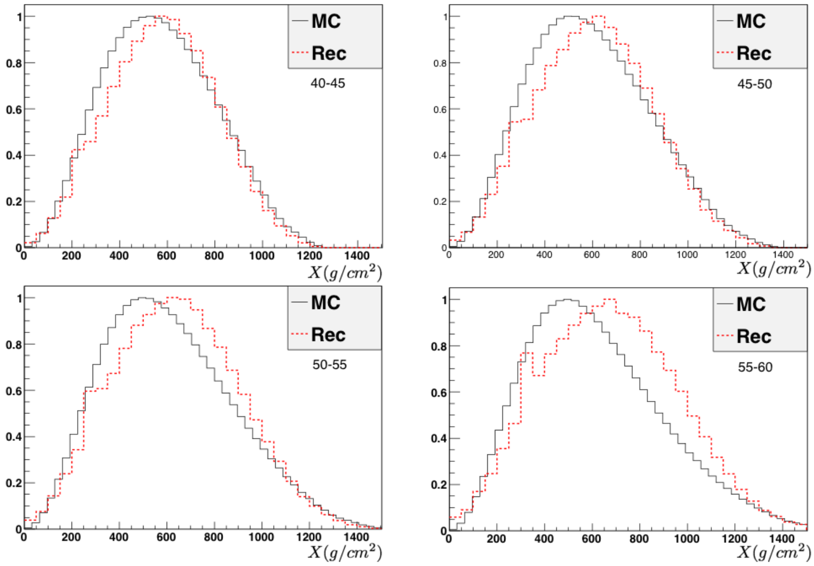

Figure 7.1: The mean MPD profile obtained from the MC muon traces for 4 angular bins (red dotted line). The solid black line profile is the simulated one, shown in Figure 6.2. Iron events, with energy between 20 and 30 EeV.

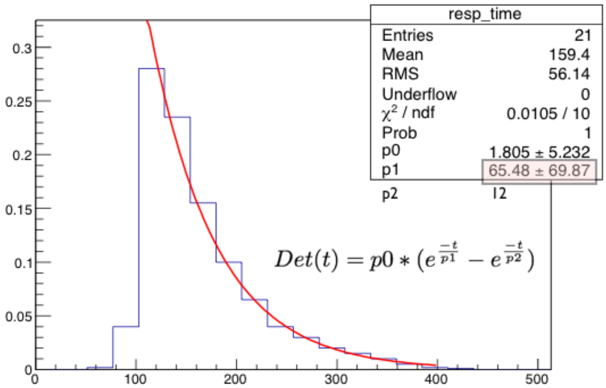

Figure 7.2: The mean muon pulse from 2000 muons injected isotropically in a SD tank. The pulse is fitted with a double exponential function. The time decay of the muon signal is about 65 ns.

The knowledge of $R(\tau)$ through the measured output signal to a single muon in a station (that of Figure 7.2) makes possible to reconstruct S_{μ}^{true}. In such reconstruction the muons will be concentrated in one or few bins and therefore appear as a peak in the traces. This will allow to reduce the detector effects and the distortion in the MPD profile. In order to deconvolve the signal, the Gold deconvolution algorithm (implemented in the ROOT package, see [Morhac et al. (1997)] for a detailed discussion of the algorithm) can be exploited: this method has proved to preserve peak positions and areas without producing any negative or oscillating behavior.

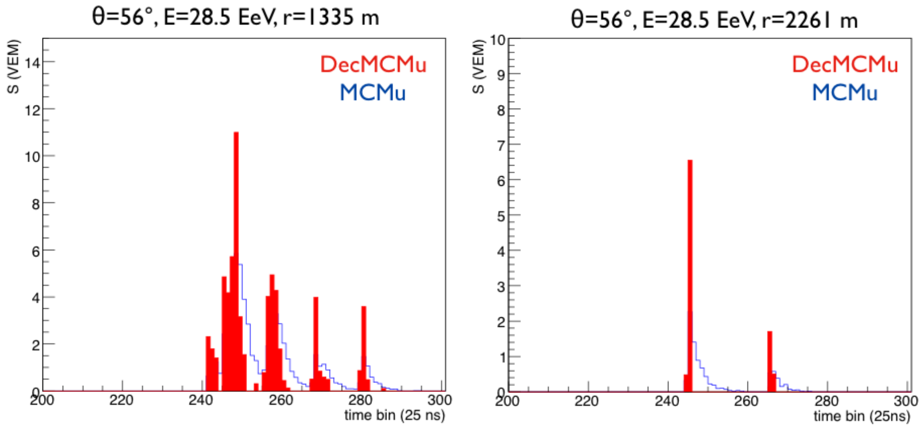

Figure 7.3: The MC muon traces and the deconvoluted trace for a station close to the core (left) and a station far from the core (right) are shown. Iron event with 56° is considered here.

An example of deconvoluted FADC trace for two different stations is shown in Figure 7.3. While far from the core (Figure 7.3(right)) spikes produced by muons are well separated and then the deconvolution output consists of two single peaks, near the core signals produced by several muons are overlapped and thus the deconvolution output is broader (Figure 7.3(left)).

Moreover, the deconvoluted trace is characterized by a small number of non-physical spikes which represent a background in our reconstruction, as it is visible in detail in Figure 7.4. To remove them, we decided to apply a constant threshold cut. To define its value, different thresholds have been applied to FADC trace bins (0.05, 0.1, 0.2, 0.3 VEM). We decided then to use a threshold of 0.1 VEM, such that the most part of the total signal (98-99%) is preserved.

The same MPD profiles of Figure 7.1, reconstructed after applying the deconvolution algorithm to MC muon traces are shown in Figure 7.5.

The profiles are no more distorted and the detector effects are corrected on average in the whole zenith angle range. The use of the deconvolution algorithm allows then to take into account the detector effects without introducing any ad-hoc time offset, as it is done in the MPD analysis for inclined events.

7.1.2 Evaluation and subtraction of the EM component

As described at the beginning of this chapter, the second main issue in extending the MPD analysis to a wider angular range is the evaluation of the EM component, which is needed to correctly extract the muonic part from the total trace.

In order to evaluate the EM component, as a first exploratory trial we applied to the total FADC time distribution:

- a constant threshold cut, based on the hypothesis of a flat EM signal, using values from 0.3 to 2 VEM;
- a time cut, based on the different fall time of the EM and muonic components.

In both cases, the EM component is not removed efficiently and the MPD profile remains distorted.

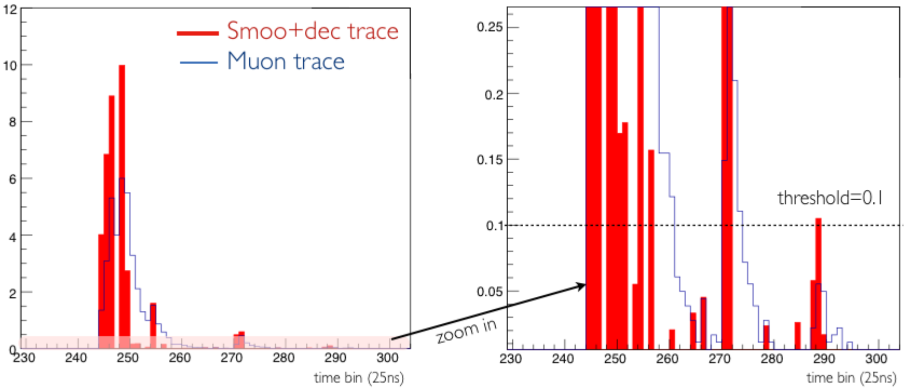

Figure 7.4: The deconvoluted trace (red filled area) resulted from the application of the deconvolution on a muon trace (blue line). To the right, a portion of the shown trace is enlarged, in order to see the small non-physical peaks in the deconvoluted trace.

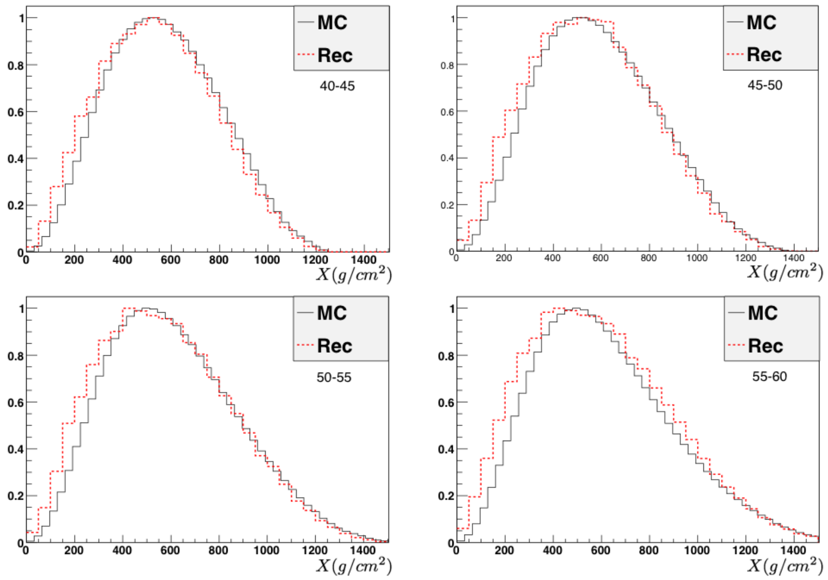

Figure 7.5: The mean MPD profile obtained by applying the deconvolution and a threshold equal to 0.1 VEM on the MC muon traces for different zenith angles. Iron events, with energy between 20 and 30 EeV.

In order to disentangle the electromagnetic and the muon components more refined techniques have been investigated, most of them based on the temporal structure of the traces in the individual Auger stations.

The time distribution of the trace is related to the height of the shower development above the detecting surface while the signal structure depends on the energy with which particles hit the Cherenkov tank and on their number density.

In the case of muons, the spread of arrival times at ground is narrow since, once produced, muons no longer interact and follow more or less a straight trajectory. Moreover, because of their low number density and the high energy (about 1 GeV/muon at ground for UHECRs), muons produce peaked signals.

On the contrary, electromagnetic (EM) particles are a part of a cascade and the time spread at ground is large. Besides, the high number density together with a mean energy of about 10 MeV/particle give rise to smooth signals.

All methods which assume that muons produce peaks in the trace have to deal with the physical background of high-energy EM particles ($E > 300$ MeV) which produce spikes indistinguishable from those of muons. This background is unavoidable in this kind of methods and has to be evaluated (see section 5.3 for a complete discussion).

In our analysis the evaluation of the electromagnetic component is done via the smoothing method. The technique is described in depth in Chapter 5 and we recall here that it allows to extract the muon signal from the total one in the $0^\circ - 60^\circ$ zenith angle range and for a large range of core distances [700, 1500 m] with a systematic uncertainty of about 10%.

We used the full sample of Monte Carlo simulations, extracting the EM and muonic components from the total trace after deconvolution.

Several parameters can be examined in order to check the quality of the muon time distribution reconstruction. For example, defining as Tx the time at which the muon signal reaches x% of the total one, it is possible to examine the relative differences ΔTx = $(Tx_{smoo} - Tx_{MC})/Tx_{MC}$ for T10, T50 and T95, as a function of energy. The results are shown in Figure 7.6.

The relative difference is below 1% in the case of $\Delta T10$ and below 5% in the case of $\Delta T50$. Therefore, the first part of the muon signal is estimated correctly by the smoothing method. It is noteworthy that even if the method has been tuned to estimate the muon signal, it has demonstrated to reconstruct the muon time distribution well too. Moreover, the method works well in the whole energy range, even if it was tuned at low energies.

If T95 is considered, the relative difference results to be greater. Indeed, the last part of the muon trace obtained with the smoothing is also populated by the spikes produced by high energy electromagnetic particles, which represent the physical background described above. Therefore T95 is significantly greater for the muon signal extracted from the total one with the smoothing method. We can qualitatively discuss the impact of this background on the MPD profile reconstruction while looking at the mean MPD profile reconstructed with the smoothed muon trace.

Indeed, what is important is how well the smoothing can reconstruct the muon time distribution, in order to obtain the MPD profile.

Figure 7.7 shows the mean MPD profile obtained with the Smoothing technique and the deconvolution (dotted red line), superimposed to the one obtained with MC muon traces and the deconvolution (blue dotted line), and the simulated one (black solid line). The mean MPD profile reconstructed with the smoothed muon trace is comparable to the one obtained with the true muon trace, except for a distortion in the tail.

The distortion is due to the high energy EM background to the smoothing method,

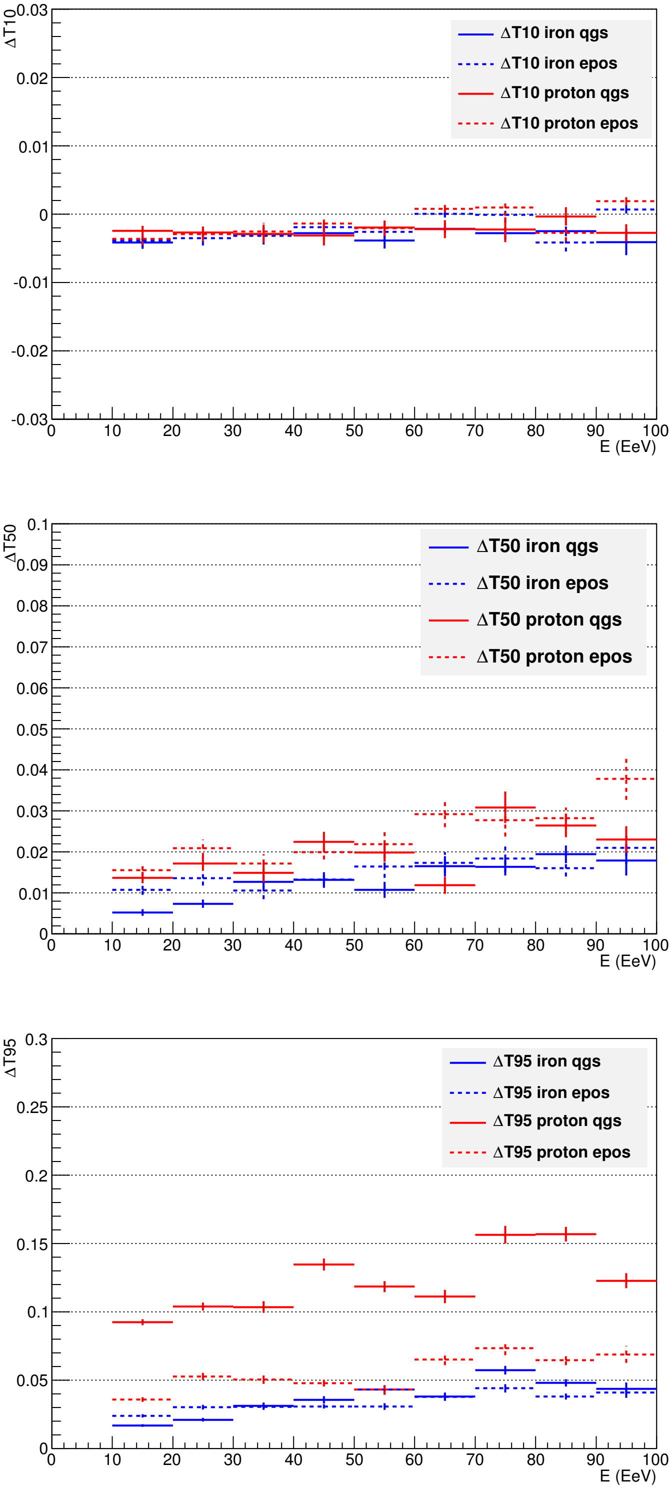

Figure 7.6: $\Delta T10$ (top), $\Delta T50$ (center) and $\Delta T95$ (bottom) as a function of energy for proton and iron showers. See text for details.

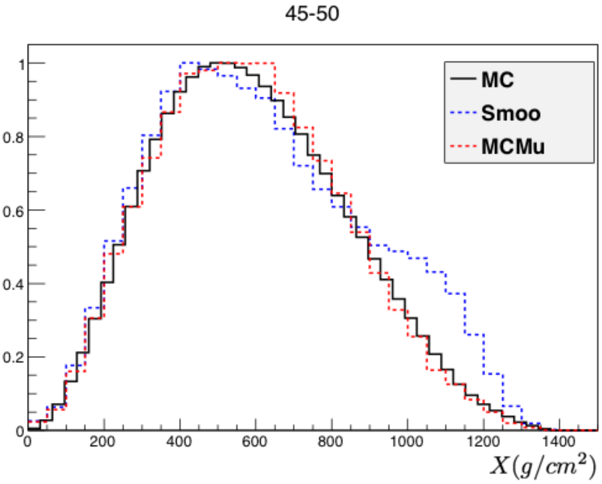

Figure 7.7: The reconstructed mean MPD profiles obtained with the deconvolution (see text for details) superimposed to the simulated one. Iron events, with energy between 20 and 30 EeV. The zenith bin $[45^\circ - 50^\circ]$ is considered here as example.

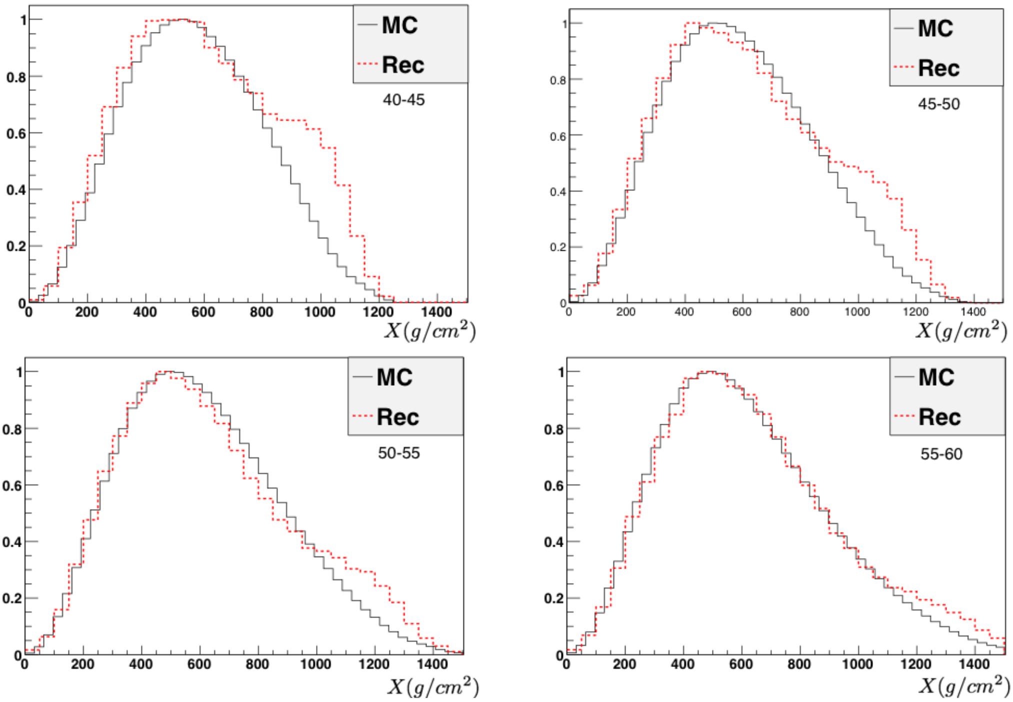

Figure 7.8: The mean MPD profile obtained with the Smoothing technique and the deconvolution applied to all stations at distance larger than 1200 m from the core, for 4 increasing θ bins. Iron events, with energy between 20 and 30 EeV.

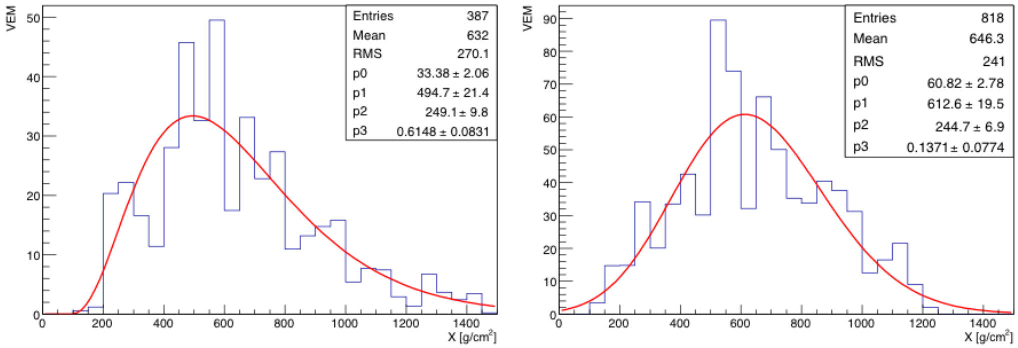

Figure 7.9: The reconstructed MPD for an iron (left) and proton (right) shower is shown. The USP fit is superimposed and the fit statistics is reported in the box.

discussed in the Section 5.3. Indeed, even if EM Spike Producing Particles may arrive at ground in a wide time window, they also produce peaks in the last part of the traces where the presence of muon signal is low. As it is visible in Figure 7.8, where the mean MPD profile obtained with the Smoothing technique and the deconvolution is shown in the four zenith angle bins, the distortion is more important at low zenith angles. Indeed, this EM background decreases with the zenith angle but it is still important between $40°$ and $50°$ (see Figure 5.7).

This background could be removed with a time cut, to be chosen in order that at least the 95% of the muon signals is preserved. The time cut will depend on energy since the trace length will increase with energy. The time cut could be based on the T95 of the simulated muon signal, i.e. the time needed for the MC muon signal to reach the 95% of the total muon one. As an example, a cut for delay greater than $\sim$ 1500 nsec completely removes the distortion at all angles for energies up to 30 EeV.

However, the SPP distortion does not affect the maximum position. Therefore we decided to apply no cut, in order to avoid the introduction of a non-negligible uncertainty due to the energy reconstruction resolution. The distortion may affect the RMS value at energies greater than 50 EeV, giving rise to an overestimation of it. A tim cut would probably be needed in that case fo low zenith angles.

7.2 Optimization of the reconstruction bias

The maximum of the longitudinal distribution function of the muon component, X^{μ}_{max}, is estimated event by event by fitting the profile with the Universal Shower Profile function described in Section 6.2, leaving all the three parameters free as was done at CORSIKA level.

The USP function reproduces the MPD profile as well as the Gaisser-Hillas function. On the other hand, it allows to fit the profile without setting any parameters, thus avoiding to introduce further sources of systematic uncertainty.

An example of reconstructed MPD profile is shown in Figure 7.9 for a proton and iron event.

A set of simple quality cuts is applied. At event level:

- 6T5 trigger condition. This is a quite stringent cut to guarantee a good reconstruc-

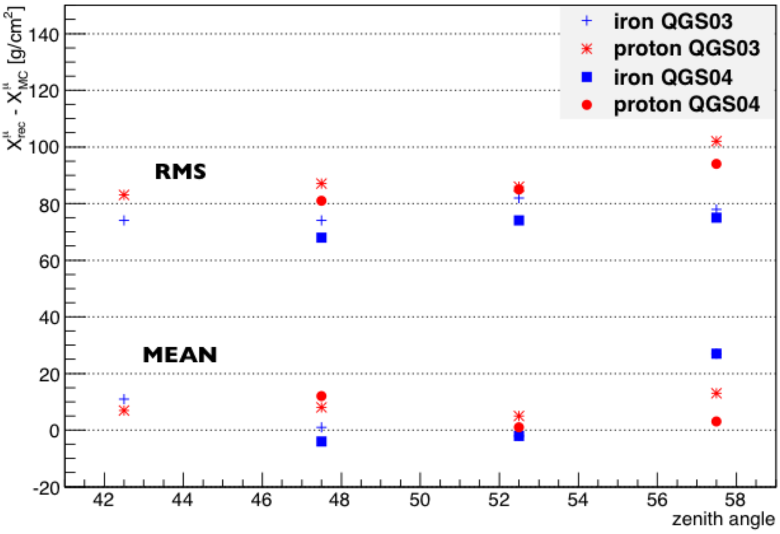

Figure 7.10: The reconstructed bias for 20-30 EeV proton and iron showers, simulated with QGSJetII03 and QGSJetII04.

tion of the shower parameters at ground.

- events with less than 5 stations participating to the MPD reconstruction are discarded. This is justified in order to have a good muon sampling at ground.

At station level:

- only candidate stations with $S_{tot} > 3$ VEM are considered, in order to minimize the impact of accidental signals and to avoid trigger fluctuations.
- traces are corrected for the effect of direct light using the algorithm described in [Smith et al. (2007)] to avoid artificial peaks.

Finally we require the following conditions for fit parameters:

- X^{μ}_{max} has to be between 100 and 1200 g/cm^2;
- the parameters L and R of the USP fit must be positive.

The first condition is fulfilled for almost all events (only 10 events in the whole simulation sample fall outside boundaries), as well as the condition for the L parameter. The request for the parameter R removes many events, mostly at low energies and for proton showers.

To check the dependence of the bias on the hadronic interaction models employed in the MC simulations, we exploited the samples of events simulated with two different versions of QGSJetII (03 and 04) and EPOS-LHC. In the case of QGSJetII-03, the angular range $[40°, 60°]$ is available. The reconstruction bias for the two different versions of QGSJetII is shown as a function of the zenith angle in Figure 7.10. The bias is within 15 g/cm^2 for both primaries in the range [40°,55°] while it is about 27 g/cm^2 in the case of

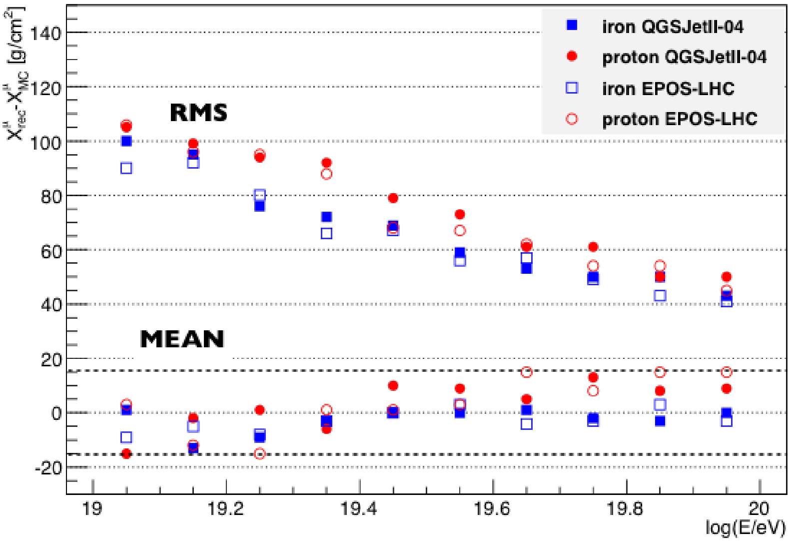

Figure 7.11: The reconstructed bias for proton and iron showers as a function of log(E/eV), estimated for all zenith angles between $45°$ and $55°$. The results for both QGSJetII-04 and EPOS-LHC are shown.

iron primaries in the range [$55°$,$60°$]. In this angular range, a time offset T_{offset} could be subtracted to the estimated arrival time of muons in SD stations in order to reduce the reconstruction bias. In particular we found that a time offset $T_{off} = 8$ ns could be used to minimize the bias. However, even if its value is well below the sampling time of the detector (the time bin of FADC traces is 25 ns) and it is comparable to the detector time uncertainty ($\delta t = 25/\sqrt{12}\ ns$), we prefer to avoid using it since its source is not clear yet. As it will explained later, from preliminary studies it has turned out that the high bias at high zenith angles could be related to the non-optimal parameterization of the kinematic delay, described in 4.3.1, which was tuned on old hadronic models.

Therefore, from now on only events with zenith angle between $40°$ and $55°$ are considered in the analysis.

Figure 7.11 shows the reconstructed bias and its RMS as a function of primary energy, for proton and irons showers, simulated with QGSJetII-04 and EPOS-LHC. All zenith angle between $45°$ and $55°$ are taken into account here since the QGSJetII-04 and EPOS-LHC simulations are available only above $45°$. The reconstruction bias results to be within 15 g/cm^2, regardless of the zenith angle, the energy, the atomic mass of the simulated primary and the hadronic model.

The RMS of $(X^{Rec}_{max} - X^{MC}_{max})$ distribution spans from 105 g/cm^2 at the lowest energies to 40 g/cm^2 at the highest energies. Its value is larger at low energies, where a smaller number of muons participate to the reconstruction and the discrete sampling at ground is more important.

7.3 Method resolution

Many sources contribute to the method resolution:

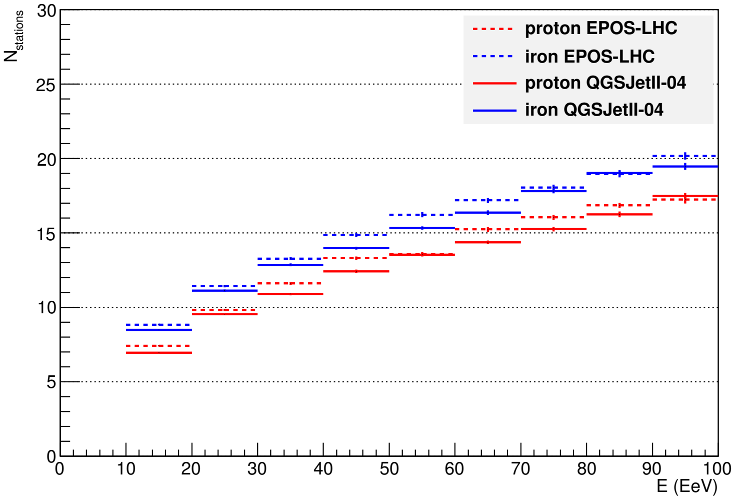

Figure 7.12: The number of stations partecipating to the MPD reconstruction as a function of energy.

- the number of muons involved in the reconstruction;
- the time uncertainty due to the FADC sampling at 40 MHz;
- the accuracy in the geometry reconstruction;
- the time distribution model and the kinematic delay approximation.

The resolution is mostly limited by the number of muons involved in the reconstruction, which accounts for about 50% of the total resolution. Indeed, the discrete sampling of muons at ground worsens the resolution, especially for low energies where the number of partecipating stations is small (see Figure 7.12).

Figure 7.13 shows the contribution due to the number of muons N_μ detected in all available detectors, for different primaries and hadronic models. δX_μ decreases as the square root of N_μ and therefore it decreases with energy and is smaller for iron showers, richer in muons.

The time uncertainty of the detector plays an important role too. Detectors have an intrinsic time resolution, δt, which limits the precision on the determination of muon arrival time. The time uncertainty of the detector, i.e. $\delta t = 25/\sqrt{12}\ ns$, translates into an uncertainty in the production distance z according to Equation 4.21:

$$\frac{\delta z}{z} \simeq -\frac{\delta t}{t} \simeq 2\frac{z}{r^2}c\delta t \tag{7.2}$$

By assuming an exponential atmospheric density, $\rho(z) = \rho_0 exp(-z cos\theta/h_0)$, the uncertainty in X_μ is then

$$\delta X_\mu = \frac{X h_0}{cos\theta}\frac{2}{r^2}log^2\frac{X cos\theta}{h_0 \rho_0}c\delta t \tag{7.3}$$

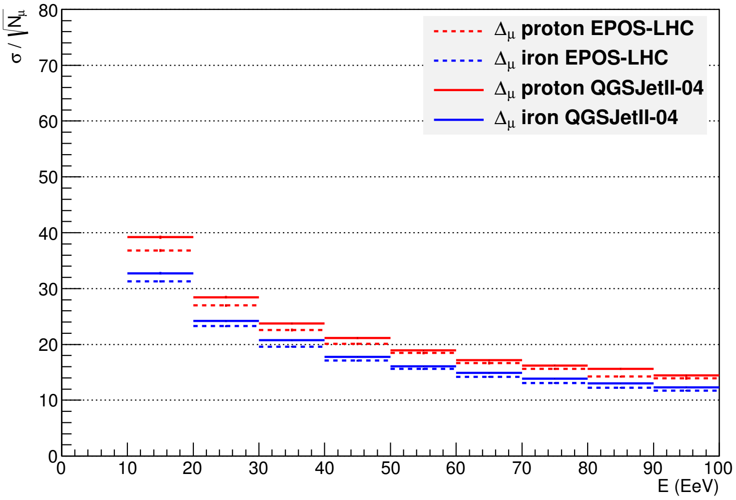

Figure 7.13: The intrinsic statistical limitation (given in g/cm^2) for X^{μ}_{max} position due to the number of muons detected in all candidate stations.

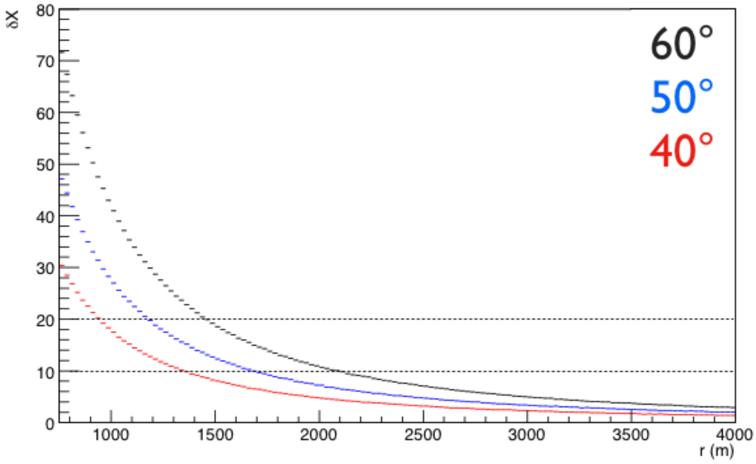

Figure 7.14: The X^{μ}_{max} uncertainty (given in g/cm^2) due to detector resolution, as a function of the distance from the core. Iron events.

where $h_0 = 7270$ m, $\rho_0 = 1.24 \cdot 10^{-3} g\ cm^{-2}$ and r is the distance from the core (see 4.3.2 for details). The uncertainty is greater at high zenith angles and decreases rapidly with the distance from the core (see Figure 7.14). In particular, its contribution to the resolution is about 15% at 60° and 30% at 60°. Therefore, reconstructing the MPD profile nearer the core increases the contribution to δX_{μ} due to the detector resolution but on the contrary decreases the more important contribution due to the number of muons sampled at ground.

Finally the contribution of geometric reconstruction accuracy is at the level of 15% [Aab et al. (2014)].

As regarding the kinematic delay approximation, we plan to study a new kinematic delay parametrization in the near future, and we will evaluate its contribution to the method resolution and systematics. Nevertheless, its effect is already incorporated in the reconstruction bias.

CHAPTER 8

MPD Analysis: application to SD data

In Chapter 7 we have discussed the MPD reconstruction based on the combined use of the smoothing method and the deconvolution algorithm.

In this chapter we will discuss the application of the method to SD data and the results achieved.

In the next section we summarize the different analysis steps, most of them are the same of the MPD analysis for inclined events described in section 4.3.2. Then the data selection, the method systematics and the results are discussed.

8.1 MPD reconstruction: summary

The MPD profile is reconstructed by following these steps:

- all candidate stations between 1200 m and 4000 m from the shower core are used in the analysis. Stations with total signal smaller than 3 VEM are rejected.
- the time traces are corrected for the effect of direct light using the algorithm discussed in [Smith et al. (2007)] to avoid artificial peaks.
- the smoothing method is applied to the total signal in order to extract the muon signal time distribution.
- the deconvolution algorithm is then applied to the smoothed muon trace and all bins with signal smaller than 0.1 VEM are set to zero.
- for each i_{th} time bin where $S(i) > 0.1$ VEM the arrival time is estimated: $t = t_0 + (i - i_0) * 25\ ns$ where t_0 is the arrival time of the shower plane and i_0 is the start bin of the trace.
- an approximate production distance z is estimated, by assuming that the time delay comes from the geometrical one only.
- the first estimate of z is used to calculate the kinematic delay from the parametrization discussed in Section 4.3.1.
- the time delay is corrected by the kinematic one and z is calculated again.
- the production distance z $[m]$ is converted in X $[g/cm^2]$ by using the atmosphere density profile from GDAS (Global Data Assimilation System) corresponding to the considered data taking period.

Quality cut	Number of Events	Efficiency
Energy and zenith ranges	2800	100%
$N_{stations} > 4$	2664	95.1%
$L > 0$ (fit parameter)	2664	95.1%
$R > 0$ (fit parameter)	2432	86.9%

Table 8.1: Quality cuts applied to data and their relative selection efficiency.

- the different $X_{\mu}(i)$ are stored in an histogram. The MPD profile is reconstructed in each station, from each functioning PMT.
- the MPD of the event is built by adding the MPD profile of all the stations partecipating to the reconstruction.
- the MPD profile is then fitted with the USP function [Cazon et al. (2012)]. All parameters are left free and the following values are set as starting points: $X^{\mu}_{max} = 600\ g/cm^2$, $L_0 = 250$ and $R_0 = 0.3$.

8.2 Data selection

The SD data of Pierre Auger Observatory between the 1^{st} january 2004 and the 31^{th} december 2013 have been analyzed, for which atmosphere database information is available.

We have considered all events with $45° - 55°$ and energy greater than 10 EeV. As we have discussed in the previous chapter, our analysis can be performed between $40°$ and $55°$. We present here the analysis in the narrower angular region [$45°$,$55°$] in order to compare the results with the currently available simulations. We therefore postpone the data analysis for zenith angle smaller than $45°$ to the near future.

We have rejected lightning events and bad periods (periods with known software or hardware malfunctioning) in order to analyze physically significant events and we took 6T5 events. The request of 6T5 trigger is a stringent quality cut (about 35% of events do not satisfied the 6T5 condition) but it allows to consider SD events with good reconstruction of all parameters at ground.

Then, we applied the quality cuts described in Section 7.2. These cuts and their selection efficiency are summarized in Table 8.1.

8.3 Method systematics

We have estimated the different contributions to the systematic uncertainty on X^{μ}_{max}.

The overall systematic uncertainty in the X^{μ}_{max} estimation is 18 g/cm^2, which represents approximately 25% of the proton-iron separation, and it is almost the same of the standard MPD analysis, for which $\sigma(sys)$=17 g/cm^2.

The different sources of systematic uncertainty are shown in Table 8.2. We will discuss each of them separately:

Reconstruction + Hadronic model + Primary As shown in Figure 7.10 and 7.11, the difference between the reconstructed maximum and the simulated one is within 15 g/cm^2 for both primaries and hadronic models, in all zenith and energy range considered. This value is then considered as the systematic error due to reconstruction effects,

Source	Systematic Uncertainty ($g\ cm^{-2}$)
Reconstruction + Hadronic model + Primary	15
Mass bias	7
Time variance model	5
Angular resolution	3
Energy resolution	2
Seasonal effects	5
Total	18

Table 8.2: The different contributions to systematic uncertainty of the reconstruction method.

the kinematic delay approximation, differences on the interaction hadronic models and on the unknown nature of the primary particle.

Mass bias The MPD profile is better reconstructed when a great number of muons is sampled. For this reason, the analysis shows a better performance in the case of iron showers, which are richer in muons. The difference in the *selection efficiency* ϵ_{rec} of the method, i.e. the number of events which pass the selection cuts, for the two primaries is smaller than 10% at all energies and for both hadronic models. This difference introduces a systematic uncertainty in the determination of X^{μ}_{max} which can be determined by analyzing a mixed sample (50% proton, 50% iron). It results in a contribution of 7 g/cm^2 to the systematic error.

Time Variance Model The uncertainty on the arrival time of the EAS front influences the reconstruction of the curvature and of the impact point on ground. Therefore, it has an impact on the reconstruction of the MPD maximum. To evaluate its contribution to the systematics of the method, two different parametrizations of the time variance [Bonifazi et al. (2008)] have been used. The difference between the two models induces a systematic uncertainty of 5 g/cm^2 on the determination of the maximum.

Energy resolution The energy resolution of the Pierre Auger observatory is 14% and it is thus necessary to study its effect on the maximum reconstruction. By allowing the energy to vary within this resolution, the reconstructed maximum results to be modified by 2 g/cm^2 at most.

Angular resolution The angular resolution of the Pierre Auger observatory is $0.7°$ in the energy and zenith angle range of interest, given the cut on the minimum number of stations participating to the event reconstruction. Its contribution to the total systematic uncertainty turns out to be 3 g/cm^2.

Seasonal Effects Changes in atmosphere affect the MPD reconstruction. In order to estimate the systematic uncertainty associated to this effect, the difference between the mean X^{μ}_{max} measured for each season and the average X^{μ}_{max} over all seasons has been studied. The data show a dependence of the measured X^{μ}_{max} with seasons, as shown in Figure 8.1. Their contribution to the systematic error is about 5 g/cm^2.

Aging Effects The physical properties of the SD may change with time. The difference between the mean X^{μ}_{max} measured for each year and the average X^{μ}_{max} over all

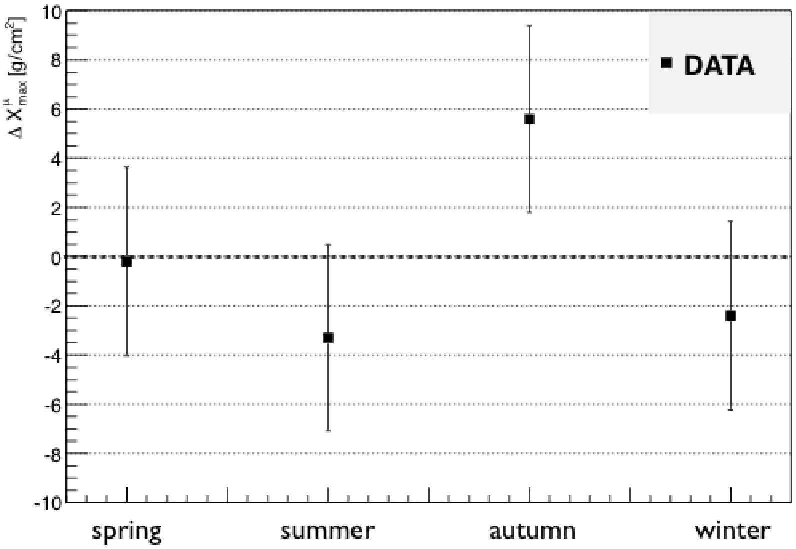

Figure 8.1: The difference between the mean maximum measured in each season and the average one is shown for each season.

years has been studied. No important ageing effects are found, as it is shown in Figure 8.2.

Indeed ΔX^{μ}_{max} is always within 10 g/cm^2, except in 2004 when there was a lack of information about the atmosphere and the number of events was smaller than in the following years. Besides, we have also checked that the average number of stations which partecipate to the MPD reconstruction be constant with time.

Fitting Procedure The fit of the MPD profile is done with the USP function and all parameters are left free, without limiting their range. Therefore there are no systematic uncertainty due to the fit procedure.

8.4 The evolution of the measured X^{μ}_{max} with energy

The evolution of X^{μ}_{max} with energy is shown in Figure 8.3, together with reconstructed X^{μ}_{max} for QGSJetII-04 and EPOS-LHC. The error bars represent the statistical uncertainty. The bin width in log(E/eV) is set to 0.1 up to $log(E/eV) = 19.7$. For higher energies, there is not enough statistics to keep this binning and only one point is used.

Two problems are still open for discussion and deserve further investigation.

The first issue is related to the kinematic delay parametrization which, as hinted before, needs to be retuned with the most recent hadronic interaction models and a dependence on zenith angle has to be introduced.

The second one regards the effectiveness of the deconvolution algorithm in correcting for the detector effects. The method was checked up to 30 EeV and needs to be verified at higher energies.

Once an optimal kinematic delay parametrization is studied, we will investigate the deconvolution performance in the whole energy range.

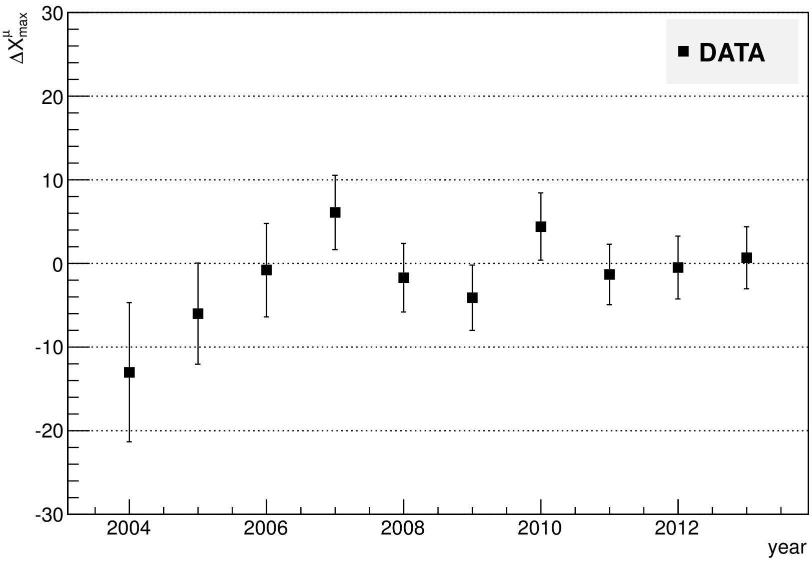

Figure 8.2: The difference between the mean X^{μ}_{max} $[g/cm^2]$ measured in each year and the mean one.

The two underlined issues will be faced in the near future. For the moment, we compare the X^{μ}_{max} from data with the reconstructed X^{μ}_{max} for the different primaries and hadronic models.

Inspecting Figure 8.3, it is clear that the interpretation of the results strongly depends on hadronic models. If QGSJetII-04 is taken as reference, data show an evolution from a mixed composition at the lower energies to an heavier composition at the highest energies. If instead EPOS-LHC is chosen, it is difficult to interprete the results since in almost the whole energy range Auger data fall below the average value for iron. However, the same problem arises in the case of the MPD analysis for inclined events (see Figure 4.13). The MPD analysis is thus a good test to understand hadronic Physics.

As regarding the last data point, it falls below both the average value for QGSJetII-04 and EPOS-LHC iron. Indeed, the distortion in the MPD profile due to the issues discussed above affects the maximum region and gives rise to an underestimation of X^{μ}_{max}. A new kinematic delay parametrization is thus required, together with a deep study of the deconvolution performances, especially at the highest energies.

It is notable that the last energy bin at $\langle log(E/eV)\rangle = 19.85$ corresponds to a center-of-mass energy that is a factor of about 40 higher than the LHC energies and the model predictions have thus to be treated carefully at these energies.

8.5 The evolution of RMS(X^{μ}_{max}) with energy

As already hinted, another important observable sensitive to mass is the RMS of X^{μ}_{max} distribution. We have seen that our method allows to correctly reconstruct the whole MPD profile, and therefore we can exploit the RMS to obtain further informations about

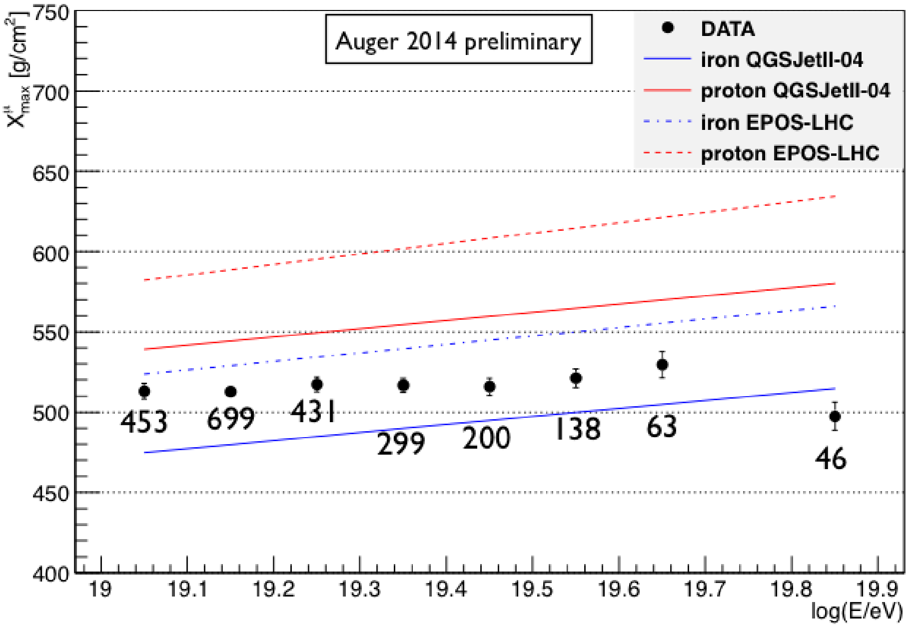

Figure 8.3: The measured X^{μ}_{max} from Pierre Auger Data is shown as a function of energy, compared to MC simulations for different primaries and hadronic models. The X^{μ}_{max} has been estimated for all zenith angles between 45° and 55°. The error bars represent the statistical uncertainties while the numbers reported indicate the number of data events in each energy bin.

primary mass.

The evolution of RMS(X^{μ}_{max}) with energy is shown in Figure 8.4. The numbers of events in each energy bin is the same reported in Figure 8.3.

As done before for the X^{μ}_{max} measurement, the comparison with models is done at reconstruction level. In this case, the main reasons behind this choice are the discrete sampling at ground and the detector resolution which broaden the X^{μ}_{max} distribution, enhancing the RMS. Therefore, the reference lines in Figure 8.4 represent the RMS of the reconstructed X^{μ}_{max} distribution for the different primaries and hadronic models. It is noteworthy that the predicted RMS(X^{μ}_{max}) are quite similar for the different models and that in all cases the data points are always bracketed between proton and iron lines.

The last point shows an RMS value which could be considered in contradiction with the respective value of X^{μ}_{max}. Indeed, while the latter falls below both the average value for QGSJetII-04 and EPOS-LHC iron, the RMS value is bracketed between proton and iron lines. The high RMS value may be due to the distortion due to the EM background which, as indicated in Section 7.1.2, may affect the RMS value at energies greater than 50 EeV. In particular, the RMS may be overestimated at the highest energies. We plan to study this issue in depth and evaluate the introduction of a time cut in order to remove the distortion in the MPD profile tail.

The results suggest a trend from a mixed composition to heavier composition as the energy rises, which is in agreement with the observations of the FD in the energy region log(E/eV) =[19.,19.5]. For higher energies, where no FD measurements are available, our analysis shows a trend to heavier elements, except the last point discussed above.

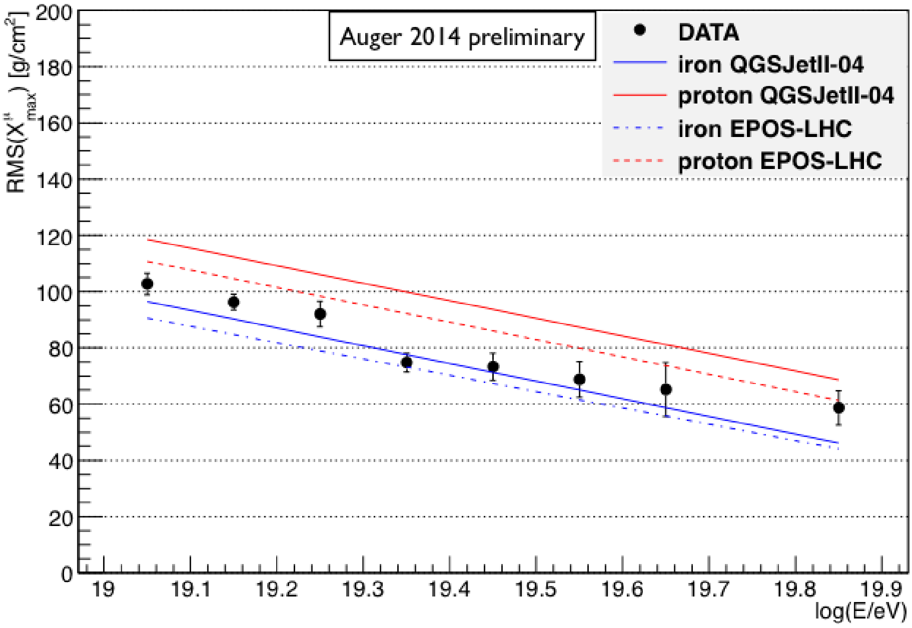

Figure 8.4: The measured RMS(X^{μ}_{max}) as a function of primary energy, for Pierre Auger data and MC simulations.

CHAPTER 9

Muon production depth reconstruction with LSD

The data taken at the Pierre Auger Observatory have allowed important developments in the field of ultra high energy cosmic rays.

Firstly the suppression of the cosmic ray flux at energies above $5.5 \cdot 10^{19}$ eV has been established unambiguously.

Then, the Auger limits to neutrino and photon fluxes at ultra-high energy have led to exclude the *top-down* source scenarios for a significant part of the observed flux.

Finally, there are indications of anisotropy in the case of particles with energies greater than $5.5 \cdot 10^{19}$ eV.

However, the origin of the flux suppression cannot be determined univocally at the moment, as well as the mass composition at the highest energies. Besides, as we have seen in Chapter 4, the muon fraction estimated from SD detectors is not properly described by current hadronic interaction models. Therefore, a better understanding of hadronic interaction properties is a crucial aspect of composition determination at the highest energies.

The results described above and these open questions have motivated the Auger Collaboration to plan an upgrade of the observatory, starting in 2015.

9.1 Beyond 2015: science case and technical strategy

The main goal of the proposed upgrade is to clarify the origin of the flux suppression, providing fundamental constraints on the astrophysical sources.

The second objective is to determine the mass composition and the proton fraction at the highest energies, in order to fully understand the origin of the suppression and the source nature. Moreover, the knowledge of the proton fraction is an important ingredient to estimate the physics potential of existing and future cosmic ray, neutrino, and gamma-ray detectors.

Composition studies crucially depend on hadronic interaction models. Therefore, the third key science objective will be to study the hadronic interactions, at the base of the models used to interpret the data, in the UHE range, well above particle accelerators reach. This will be possible by exploiting the detailed shower observations possible with the upgraded Auger detector.

In order to achieve these three goals, the upgrade must allow to:

- measure the primary energy and mass with high precision, particularly at the highest energies;
- measure the LDF of the muon and electromagnetic components separately, with better muon identification and extending closer to the core without saturation of the SD detector signals;

- measure the depth of the shower maximum for both the electromagnetic and muonic component.
- collect as many events as possible.

Several proposals have been suggested for the upgrade detector, as it will be briefly described in the following section. Common to all of them is the surface detector electronics (SDE) upgrade, which includes faster sampling of the FADC traces (120 MHz) and an improved GPS timing.

9.2 Beyond 2015: proposed upgrades

The upgrade detectors must improve the muon/electromagnetic separation achieved with the standard SD detector and reduce model-dependent systematic errors. Two different technologies are under study and prototyping include:

- placement of external scintillator-based detectors;
- segmentation of the current SD detectors, i.e. Layered Surface Detector (LSD).

A full array upgrade is required in order to do unbiased measurements, to better control shower-to-shower fluctuations and to exclude a dependence on systematic offset of energy for protons and iron nuclei.

The upgraded Pierre Auger Observatory, if built, would continue operations from 2015 to 2023, approximately doubling the available data set.

We will briefly describe the scintillator option below. The LSD option will be discussed in a dedicated section, since part of the present thesis work was performed at LPNHE in Paris and dealt with the application of the MPD analysis to the LSD simulated data.

9.2.1 Scintillator-based detectors

The muon component can be measured directly by using buried plastic scintillator detectors. The proposed detectors are 10 m^2 active surface of plastic scintillators with wavelength shifting fibers, read out in integrated mode by a single PMT and installed next to each SD tank 1.3 m underground. The ground provides passive shielding from the electromagnetic component of the showers: the expected contamination from EM energy deposition is of the order of few % at 500 m from the core, and decreasing with distance. Therefore, no simulation based algorithms are needed to separate muonic and EM signals [Aglietta et al. (2013),Aglietta et al. (2014)].

However, the deployment of buried detectors can be considered not feasible over the whole experimental area (3000 km^2) due to the presence of underground water in some locations. There, one could envisage the deployment of similar detectors, smaller in size, on the top of each WCD. This will allow to estimate the muon component by comparing the scintillator signal with the tank one. Indeed, as the WCD is already quite sensitive to the muonic component of the extensive air showers (EAS), a scintillator detector on the surface, more sensitive to the electromagnetic component of the EAS, could provide a complementary measurement. The muon signal can be obtained , in this case, by performing a global fit of the two detector signals, based on the universality features of the showers [Schmidt et. al (2007)].

9.3 LSD

The LSD option [Letessier-Selvon et al. (2014)] is based on the fact that EAS EM particles reach ground with an average energy of about 10 MeV and are absorbed in water over lengths of the order of 36 cm while EAS muons, which have a mean energy of about 1 GeV, can go through several meters without being absorbed. Figure 9.1 shows the distribution of Cherenkov photons production point in the WCD by photons (left), electrons/positrons (center) and muons (right). As expected the EM component mainly deposits its energy on the top and side of the station, while muons deposit energy uniformly in the tank. Therefore, if the water Cherenkov tank is divided into two horizonal layers, the bottom one will be partially shielded from the EM component and the two volumes will provide distinct responses allowing separation of the EM and muonic components of the EAS.

In its simplest form, a LSD is composed of two independent and light-tight volumes created by inserting an horizonal reflective layer at a height of 80 cm from the WCD bottom. The LPNHE group has built three prototypes between March and July 2014 that are taking data in a part of the Auger array dedicated to the prototypes study.

The signal in the top layer will be read out by the three PMTs that equip the Auger WCD, while the light in the bottom will be collected by an additional PMT. Some simplified schematics and an artistic view of the LSD is shown in Figure 9.2.

The reconstruction of the two components relies on the fraction of the signal deposited by each component in each segment. Those fractions define a 2x2 matrix M which gives the measured top and bottom signal as a linear superposition of the EM and muon contributions:

$$\begin{pmatrix} S_{top} \\ S_{bottom} \end{pmatrix} = M \begin{pmatrix} S_{em} \\ S_{\mu} \end{pmatrix} = \begin{pmatrix} a & b \\ 1-a & 1-b \end{pmatrix} \begin{pmatrix} S_{em} \\ S_{\mu} \end{pmatrix} \tag{9.1}$$

If the matrix M can be inverted, the EM and muonic signal in the LSD can be estimated as

$$\begin{pmatrix} S_{em} \\ S_{\mu} \end{pmatrix} = M^{-1} \begin{pmatrix} S_{top} \\ S_{bottom} \end{pmatrix} \tag{9.2}$$

The coefficient a represents the fraction of EM p.e. collected in the top layer while b represents the fraction of muon ones collected in the top layer. Both are obtained from Monte Carlo simulations and are essentially independent of the primary type, energy, incident angle, distance and hadronic models.

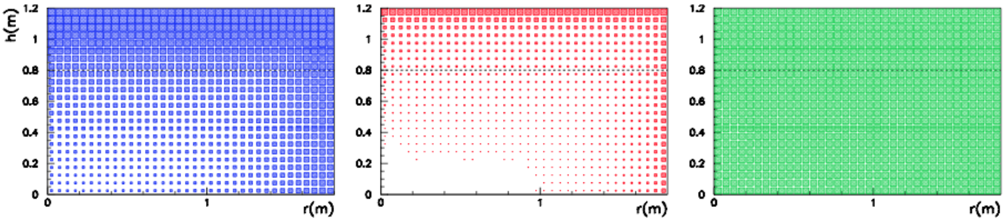

Figure 9.1: Distribution of the Cherenkov photons production point in a 1.2 m height and 1.8 m radius WCD. From left to right the contribution from the photons, $e^{+}e^{-}$ and muon component of a 30 EeV EAS with 45° zenith angle is shown [Letessier-Selvon et al. (2014)].

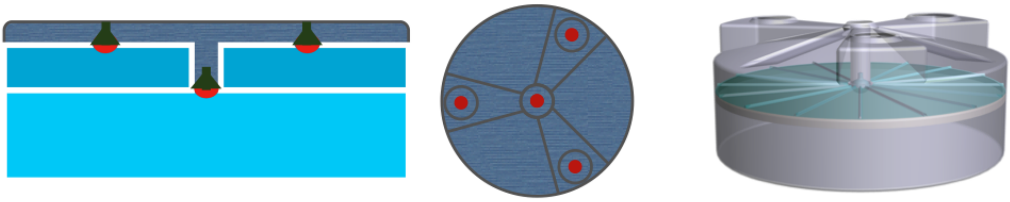

Figure 9.2: Schematic and artistic view of a LSD built from an Auger WCD design [Letessier-Selvon et al. (2014)].

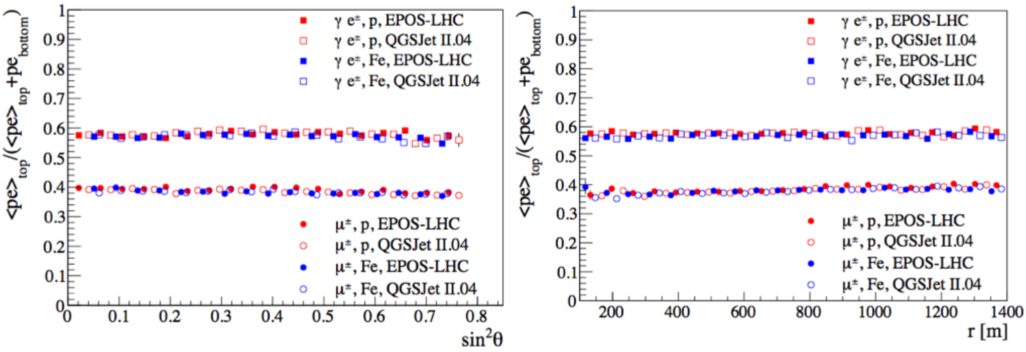

Figure 9.3: The fraction of the number of photoelectrons in the top layer for the EM (square symbols, *a* coefficient of the matrix) and muonic (round symbols, *b* coefficient) component, as a function of zenith angle (left) and distance from the core (right) [Letessier-Selvon et al. (2014)].

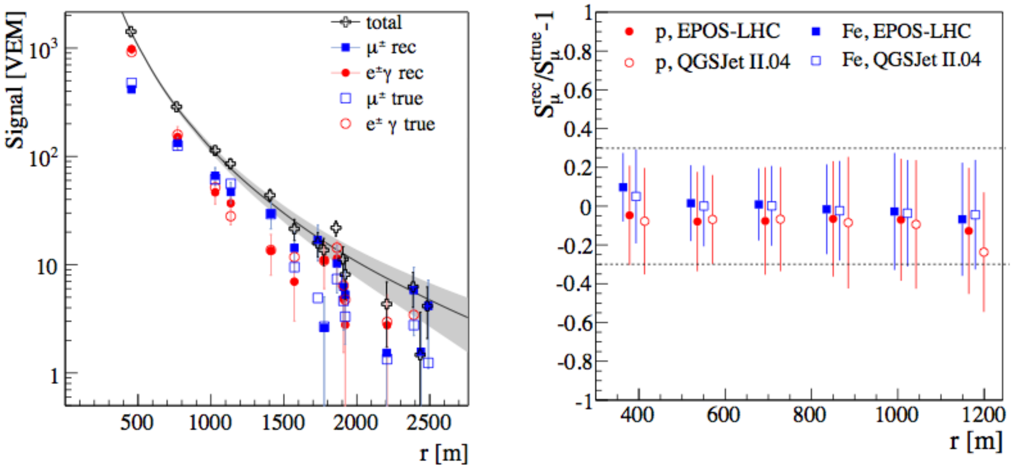

Figure 9.4: Left) Example of muonic and EM independent LDFs, reconstructed using the inversion matrix in each LSD detector. Right) Individual LSD muon signal reconstruction as a function of the distance to core, the error bars represent the signal resolution [Letessier-Selvon et al. (2014)].

They only depend on tank geometry, which can be easily modeled, and on the efficiency of the light collection.

Figure 9.3 shows that, in the case of the Auger WCD geometry, a and b are independent of the shower zenith angle in the range [0, 60°] and on the distance from the core in the range [0, 1500] m. The mean values are: $a = 0.57 \pm 0.01$ and $b = 0.38 \pm 0.01$.

The estimated EM and muonic signal can be used to derive the respective LDFs (see Figure 9.4(left)). The two independent LDFs are then exploited to perform an energy reconstruction that takes into account the muon size and shower age and to produce a calibration based on the electromagnetic component only.

With LSD, the muon signals can be reconstructed for distances from nearly 400 m to 2000 m for the highest energetic showers. At 10 EeV, the relative difference between the reconstructed muon signal and the simulated one is better than 25% when more than 20 muons enter the detector, as shown in Figure 9.4(right).

The global resolution on the EAS muon size parameter, i.e. the muon signal at 1000 m from the core, is 20% (16%) for proton (iron) at 10 EeV, improving to about 10% for both at 70 EeV (see Figure 9.5).

9.4 MPD reconstruction with the bottom layer

As we have seen in Chapter 6, the MPD reconstruction via the muon time distribution model can be performed far from the core ($r > 1200$ m). Indeed, closer to the core the kinematic delay contribution is important and cannot be considered as a correction.

On the contrary, the reconstruction of the muon signal with LSD is accurately performed near the core, i.e. for distance between 200 m and 1400 m, where the inversion matrix works properly.

Farther from the core the latter fails because the ratio between the top and bottom signal is small and there are not enough muons. This limitation has not a big impact on the estimation of $S_{\mu}(1000)$ because the fit is basically determined by the 3 stations closer

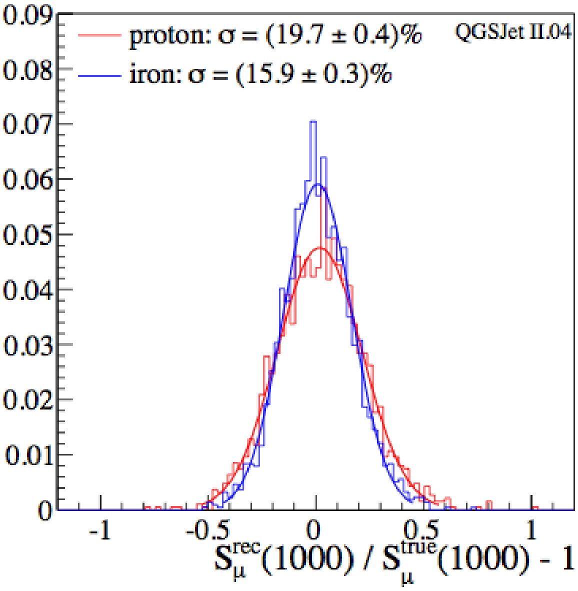

Figure 9.5: Global resolution on the muon size at 1000 m S_μ for air showers with energy between 8 and 13 EeV [Letessier-Selvon et al. (2014)].

to the core. The resolutions on $S_\mu(1000)$ changes by only about few % if the stations at distances larger than 1400 are included.

On the contrary, the limitation is important for the MPD reconstruction, for which only stations at distance greater than 1200 m can be used and it is thus necessary to go farther than 1400 m in order to sample with enough points the MPD distribution.

Therefore, we investigated several methods to extract the muon signal, all based on the different signal structures in the top and bottom layers.

We tested the extraction of the muon signal in the bottom layer, which is partially shielded to EM particles by the top layer. Indeed it is possible to exploit a simple threshold cut to remove the EM contamination and estimate the muon signal and its time distribution.

The threshold cut is performed after applying a deconvolution algorithm to the total trace in the bottom. As seen in 7.1.1, the deconvolution allows to determine the muon peak position more accurately, and it can be exploited to correct the distortion of the MPD profile due to the detector effects.

The Gold deconvolution [Morhac et al. (1997)] of the ROOT package is exploited (see 7.1.1 for details), and the mean bottom response to muons used to deconvolute the bottom signal is shown in Figure 9.6. In particular the detector response to muons is different for the top and the bottom layers, and both are different from the standard tank response to muons. We have thus determined the mean muon pulse in each layer by injecting 1000 omnidirectional muons in the tank, for the different considered geometries. The threshold cut is obtained as a function of the total signal in the bottom:

$$S_{thr} = 0.15 + 0.02 \cdot S_{bottom} \tag{9.3}$$

and has been tuned such that the 95% of the muon signal is preserved, regardless of the energy and mass of the primary particle.

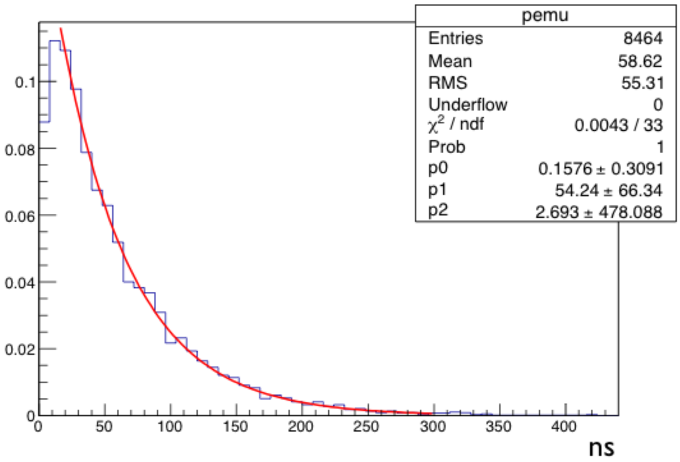

Figure 9.6: The mean muon shape averaged on 2000 muons injected in LSD and read out in the bottom, fitted with a double exponential law.

	QGSJetII04 p — Fe	EPOS-LHC p — Fe
energy	63 EeV	63 EeV
zenith angle	51°	51°
showers	400	400
reconstructed events	1000	1000

Table 9.1: Simulation libraries used.

By requiring a minimum signal in the bottom of 10 VEM, the muon signal is reconstructed with a relative difference $\Delta_{\mu,dec} = (S_{\mu}^{dec} - S_{\mu}^{MC})/S_{\mu}^{MC}$ smaller than 10%, for $\theta > 30°$ and distances from the core between 600 m and 1800 m.

The MPD profile is then reconstructed from the deconvoluted muon trace by exploiting the muon time distribution model (discussed in 4.3.1).

9.4.1 Reconstruction bias and resolution

The maximum of the longitudinal distribution function of the muon component, X^{μ}_{max}, is estimated event by event by fitting the MPD profile with the Universal Shower Profile function (see Section 6.2), leaving all parameters free.

We have tuned the method using 63 EeV iron and proton showers with $\theta = 51°$, since they were the only available simulations at the moment. A summary of the libraries used is given in Table 9.1.

We performed the reconstruction by considering stations with distance greater than 1200 m from the core, and we applied a set of simple quality cuts, as in the analysis presented in Chapters 7 and 8.

At event level:

- 6T5 trigger condition. This is a quite stringent cut to guarantee a good reconstruction of the shower parameters at ground;

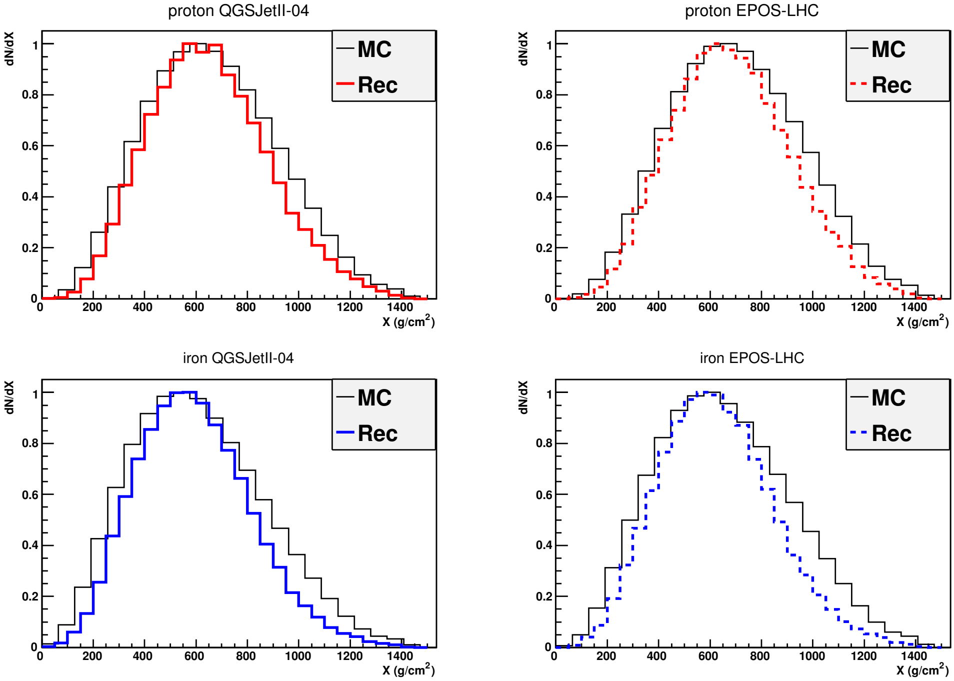

Figure 9.7: The mean MPD profile reconstructed with stations at distance greater than 1200 m from the core, superimposed to the simulated one. Iron and proton showers, simulated with QGSJetII-04 and EPOS-LHC, $\theta = 52°$, E=63 EeV.

- events with less than 5 stations participating to the MPD reconstruction are discarded. This is justified in order to have a good muon sampling at ground.

At station level:

- only candidate stations with $S_{tot} > 3$ VEM are considered, in order to minimize the impact of accidental signals;
- traces are corrected for the effect of direct light using the algorithm described in [Smith et al. (2007)] to avoid artificial peaks.

Finally we required the following conditions to fit parameters:

- X^{μ}_{max} has to be between 100 and 1200 g/cm^2;
- the parameters L and R of the USP fit must be positive (see Section 6.2 for details).

Figure 9.7 shows the mean MPD profile reconstructed with the bottom side of LSD. As it is visible, the position of X^{μ}_{max} is reconstructed correctly for both proton and iron showers and for the two considered hadronic models. The reconstructed MPD profile is narrower than the simulated one, because the muon component is slightly undersampled.

We have estimate the reconstruction bias $X^{\mu}_{rec} - X^{\mu}_{MC}$ event by event and it results to be within 12 g/cm^2, regardless of the mass of the simulated primary and the hadronic model used. A summary of the obtained values is shown in Table 9.2.

	QGSJetII-04 proton	QGSJetII-04 iron	EPOS-LHC proton	EPOS-LHC iron
$X^{\mu}_{rec} - X^{\mu}_{MC}$ $[g/cm^2]$	-1	11	-12	-5
RMS($X^{\mu}_{rec} - X^{\mu}_{MC}$) $[g/cm^2]$	51	50	57	44

Table 9.2: The reconstruction bias and the resolution obtained for the different simulations.

The RMS($X^{\mu}_{rec} - X^{\mu}_{MC}$) turns out to be smaller than 60 g/cm^2 for both primaries and hadronic models considered here, and it is comparable to the one obtained with the standard WCD (about 55 g/cm^2 at 63 EeV).

We can notice that the reconstruction bias for a given primary differs significantly in the two hadronic models: 16 g/cm^2 in the case of iron showers, 11 g/cm^2 in the case of proton ones.

As discussed for the standard WCD, the kinematic delay parametrization [Cazon et al. (2012)] may not reproduce correctly the kinematic delay of muons at ground for the two different hadronic models considered here. The difference in the reconstruction bias could thus be due to that. In particular, we have seen that the mean muon energy at ground and the muon number turn out to be greater in the case of QGSJetII-04 with respect to EPOS-LHC (see Figure 9.8(top)). As a result, the kinematic delay is smaller on average in the case of QGSJetII-04 model (see Figure 9.8(bottom)) and it can therefore justify the greater bias obtained in the X^{μ}_{max} reconstruction for QGSJetII-04.

As already hinted, a new parametrization of the kinematic delay will be done with the new hadronic models in the near future.

However, this preliminary study shows that the MPD reconstruction can be performed with the proposed upgrade LSD. Even if the analysis has not be tuned in detail, its potentialities are evident and the results obtained are compatible to the ones obtained with the standard tank (shown in Chapter 7).

The advantage of using an upgraded detector as LSD is that it will directly provide the timing of the muonic signal and thus it will not require further analysis algorithm (e.g. smoothing method) for the subtraction of the em component. Indeed, a simple threshold cut is enough, even for events with $\theta < 60°$.

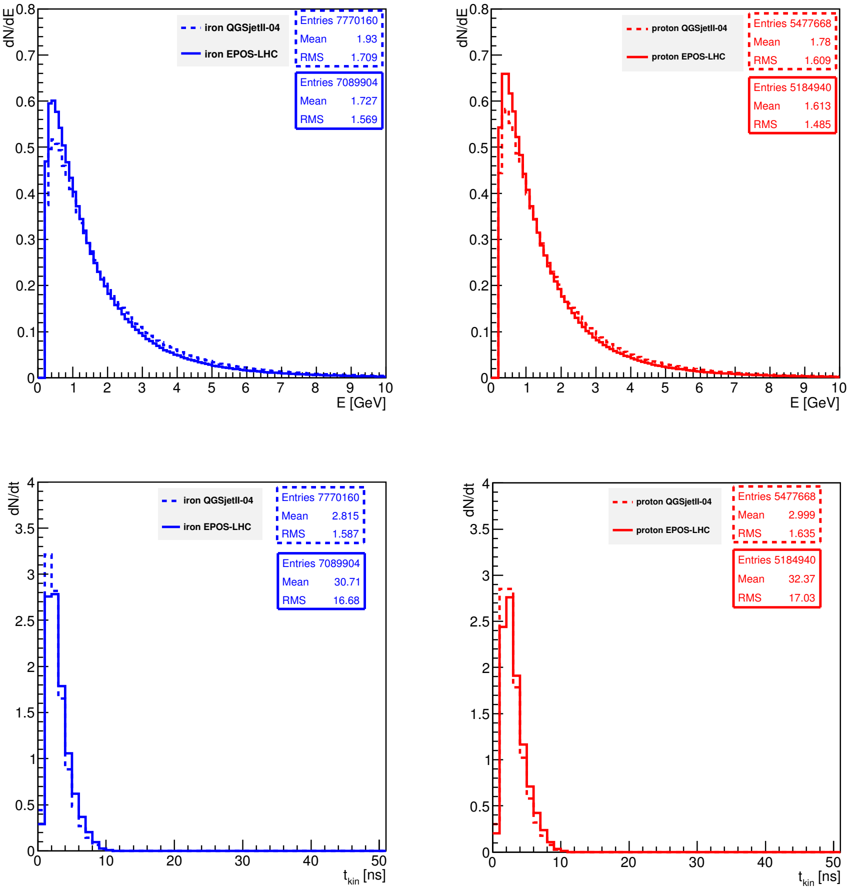

Figure 9.8: Top) The muon energy distributions averaged over 10 showers, for $r > 1200$ m. Bottom) The muon parametrized kinematic delay averaged over 10 showers, for $r > 1200$ m.

Conclusions and outlook

The main topic addressed by the present thesis is the measurement of UHECR mass composition using data from the surface detector (SD) of the Pierre Auger Observatory. The knowledge of the nature of the primaries at the highest energies is a mandatory task from the astrophysical point of view, since it could allow to separate the different scenarios of origin and propagation of cosmic rays. Furthermore, these studies are of utmost importance for particle physics, as knowing the composition one can explore the hadronic interaction at ultra-high energies, inaccessible to present accelerator experiments.

The goal of this thesis is the reconstruction of the muon production depth profile (MPD) from the SD traces. The reconstruction of the MPD is a promising method to extend the study of composition to an energy range higher than the one covered by the FD (we remind here that the maximum of the EAS development, X_{max}, measured by the FD, is the most sensitive observable for composition studies).

Until now, the MPD analysis was limited to ultra high energy inclined events. In the present thesis we present a method which is able to extend the range of applicability to lower zenith angles and energies.

In order to do that, different problems have been addressed.

Separation of the EM and muonic components in the SD signals

We have exploited the smoothing method to extract the muon time distribution from the total one recorded in SD.

We have demonstrated that the method is not only able to reconstruct the muonic signal, but also its time distribution.

In particular we have established that the method works well in a wide range of energies, zenith angles and distances from the core, as reported in the following table:

log(E/eV)	[19,20]
Zenith angle	$[40°, 60°]$
Distance	1200-4000 m

Correction of the detector effects

The detector response to muons affects the MPD profile reconstruction. In order to correct for it we have exploited the deconvolution algorithm of the ROOT package:

the deconvolution is applied to the muon signal, allowing to determine the muon peak position accurately.

We have demonstrated that the method removes efficiently the detector effects in the zenith angle range considered and up to 30 EeV, without introducing any ad-hoc time offset (as, on the contrary, it is done in the inclined events analysis). Moreover the deconvolution allows to take into account the detector effects without MC-based corrections and this feature makes the method robust and independent from hadronic models.

A study of the performances of the deconvolution method at higher energies is however still to be performed. At these energies, the algorithm may not be able to effectively correct for the detector effects, due to the fact that muon signals could be highly overlapped. We will investigate this issue in the near future.

Extension of the MPD analysis to a wider zenith angle and energy range

The combination of the smoothing method and the deconvolution algorithm allows to extend the MPD analysis range down to 10 EeV and down to $40°$ (although the simulations at our disposal allowed to test it above $45°$, the method is applicable down to $40°$).

The following table summarizes the improvements in the SD data analysis with respect to the MPD analysis for inclined events:

	Std. Analysis	This work
r_{cut}	1700 m	1200 m
Zenith angle	$[55°, 65°]$	$[45°, 55°]$
log(E/eV)	> 19.3	$> 19.$
Statistics	$\approx$ 500 events	$\approx$ 2400 events

The X^{μ}_{max} and its RMS have been reconstructed event-by-event in the range reported above, for the data collected by the SD array of the Pierre Auger Observatory between January 2004 and December 2013.

The interpretation of the measured elongation rate depends strongly on the hadronic interaction models used in the simulations. If QGSJetII-04 is taken as reference, the data show an evolution from a mixed composition at lower energies to an heavier composition at the highest energies. If instead EPOS-LHC is chosen, it is difficult to interpret the results since in almost the whole energy range Auger data fall below the average value for iron primaries. However, the same problem arises in the case of the MPD analysis for inclined events. The MPD analysis is thus a good test to understand hadronic Physics.

In the case of RMS(X^{μ}_{max}), the interpretation depends less on hadronic models and data points are always bracketed between proton and iron lines, for both QGSJetII-04 and EPOS-LHC models.

The results suggest a trend from a mixed composition to heavier composition as the energy rises, which is in agreement with the observations of the FD in the energy region log(E/eV) =[19.,19.5]. For higher energies, where no FD measurements are available, our analysis shows a trend to heavier elements.

Reconstruction of the MPD with the Layered Surface Detector

We have shown that the MPD can be reconstructed with the LSD detector, proposed for the upgrade of the Observatory.

In particular it is possible to exploit the shield to EM particles provided by the top layer to reconstruct the muon signal in the bottom one.

The analysis has not been tuned in detail because of the lack of targeted simulations. However the potentialities of the method have been outlined and the results turn out to be compatible to the ones obtained with the standard WCD.

The advantage of using an upgraded detector as LSD is that it will directly provide the timing of the muonic signal and thus it will not require further analysis algorithm for the subtraction of the EM component.

Outlook

The results shown in the present thesis demonstrate that the MPD analysis can be performed for events with zenith angle smaller than $55°$, with a significant improvement in the available statistics.

Different issues can be addressed in the future to improve the results. Among them:

- the parametrization of the kinematic delay must be optimized for the most recent hadronic models and a dependence on zenith angle has to be introduced;
- the deconvolution power in correcting for detector effects must be checked for the highest energies.

After optimization of the kinematic delay parametrization, the deconvolution performance can be studied in the whole energy range. For example, differet MPD reconstruction strategies can be thought of, exploiting the differencies in arrival times among the muons for different shower energies and core distances.

Besides, new and higher statistics simulations will be available soon, thus allowing to extend the data analysis down to $40°$.

Afterwards, we plan to combine our results with the ones of the other MPD analyses.

Finally, we plan to study the MPD reconstruction with LSD in the same energy and angular range of the standard WCD, when targeted simulations will be available.

Bibliography

A. Aab et al (Auger Coll.), *Proc. 33rd ICRC*, Rio de Janeiro (2013)

A. Aab et al. (Auger Coll.), *Depth of Maximum of Air-Shower Profiles at the Pierre Auger Observatory: Measurements at Energies above* $10^{17.8}$ *eV* (2014) [arXiv:1409.4809]

A. Aab et al. (Auger Coll.), *Reconstruction of inclined air showers detected with the Pierre Auger Observatory* (2014) [arXiv:1407.3214v1]

A. Aab et al. (Auger Coll.), *Muons in air showers at the Pierre Auger Observatory: measurement of atmospheric production depth* (2014) [arXiv:1407.5919]

R. Abbasi et al. (HiRes Coll.), *A Study of the Composition of Ultra–High-Energy Cosmic Rays Using the High-Resolution Fly's Eye*, Astrophys. J., 622:910 (2005)

R. Abbasi et al. (HiRes Coll.), *First Observation of the Greisen-Zatsepin-Kuzmin Suppression*, Phys. Rev. Lett., 100:101101 (2008)

R. Abbasi et al. (HiRes Coll.), *Indications of Proton-Dominated Cosmic-Ray Composition above 1.6 EeV*, Phys. Rev. Lett. 104, (2010) 161101.

R. Abbasi et al. (TA Coll.), *Study of Ultra-High Energy Cosmic Ray Composition Using Telescope Array's Middle Drum Detector and Surface Array in Hybrid Mode* (2014) [arXiv:1408.1726]

J. Abraham et al. (Auger Coll.), *Measurement of the energy spectrum of cosmic rays above* 10^{18} *eV using the Pierre Auger Observatory*, Phys. Letters B 685, 239 (2010) [arXiv:1002.7975v1]

J. Abraham et al. (Auger Coll.), *The fluorescence detector of the Pierre Auger Observatory*, Nucl. Instrum. Meth. A 620, 227 (2010) [arXiv:0907.4282]

J. Abraham et al. (Auger Coll.), *Measurement of the Depth of Maximum of Extensive Air Showers above* 10^{18} *eV* (2010) [arXiv:1002.0699v1]

J. Abraham et al. (Auger Coll.), *Trigger and aperture of the surface detector array of the Pierre Auger Observatory*, Nucl. Instr. Meth. A613, 29 (2010)

P. Abreu et al. (Auger Coll.), *Proc. 32nd ICRC*, Beijing (2011)

P. Abreu et al. (Auger Coll.), *The Rapid Atmospheric Monitoring System of the Pierre Auger Observatory* (2012) [arXiv:1208.1675v1]

P. Abreu et al. (Auger Coll.), *Interpretation of the Depths of Maximum of Extensive Air Showers Measured by the Pierre Auger Observatory* (2013) [arXiv:1301.6637]

P. Abreu et al. (Auger Coll.), *Constraints on the Origin of Cosmic Raysi above* 10^{18} *eV from Large-scale Anisotropy Searches in Data of the Pierre Auger Observatory* (2013) [arXiv:1212.3083]

T. Abu-Zayyad et al. (TA Coll.), *The surface detector array of the Telescope Array experiment*, Nucl. Inst. and Meth. A 689 (2012) 87–97

T. Abu-Zayyad et al. (TA Coll.), *The Cosmic Ray Energy Spectrum Observed with the Surface Detector of the Telescope Array Experiment* (2012) [arXiv:1205.5067]

M. Aglietta et al. (Auger Coll.), *Response of the Pierre Auger Observatory water Cherenkov detectors to muons*, Proc. 29th ICRC (2005)

M. Aglietta et al., *MuScint - An underground Muon Detector for the Beyond 2015 Auger Upgrade*, Internal Auger GAP Note 50 (2013)

M. Aglietta et al. , *TOSCA, The Observatory Scintillator Array Technical Project*, Internal Auger GAP Note 74 (2014)

S. Agostinelli et al. (GEANT4 Coll), *Geant4 — a simulation toolkit*, Nucl. Instr. and Meth. A, 506:250 (2003)

D. Allard, E. Parizot and A. Olinto, *On the transition from galactic to extragalactic cosmic-rays: Spectral and composition features from two opposite scenarios*, Astropart. Phys. 27, 61 (2007)

D. Allard, *Extragalactic propagation of ultrahigh energy cosmic-rays*, Astropart. Phys. 39-40, 33 (2012), [arXiv:1111.3290]

I. Allekotte et al. (Auger Coll.), *The surface detector system of the Pierre Auger Observatory*, Nucl. Instr. and Meth. A586, 409 (2008) [arXiv:0712.2832]

J. Allen and G. Farrar, *Electromagnetic Contamination in Spiky FADC Traces*, Internal Auger GAP Note 31 (2009)

R. Aloisio,V. Berezinsky and P. Blasi, *Ultra high energy cosmic rays: implication of Auger data for source spectra and chemical composition* (2013) [arXiv:1312.7459v1]

J. Alvarez-Muniz et al., *Influence of shower fluctuations and primary composition on studies of the shower longitudinal development*, Phys. Rev. D 69 (2004) [arXiv:astro-ph/0402092]

L. Anchordoqui et al, *Ultrahigh energy cosmic rays: The state of the art before the auger observatory* (2002) [hep-ph/0206072]

L. Anchordoqui (Auger Coll.), *The Pierre Auger Observatory: Science Prospects and Performance at First Light* (2004) [arXiv:astro-ph/0409470]

S. Argiro et al., *The Offline Software Framework of the Pierre Auger Observatory*, (2007) [arXiv:0707.1652]

M. Ave et al., *Composition sensitivity of the auger observatory through inclined showers*, Phys. Rev. D 67 (2003)

R. Baltrusaitis et al., *The Utah Fly's Eye Detector*, Nucl. Instr. and Meth. A240, 410 (1985)

E. Barcikowski et al., *Mass Composition Working Group Report* (2013) [arXiv:1306.4430v1]

P. M. Bauleo and J. R. Martino, *The dawn of the particle astronomy era in ultra high energy cosmic ray*, Nature 458, 847-851 (2009)

E. G. Berezhko, S. P. Knurenko and L. T. Ksenofontov, *Composition of cosmic rays at ultra high energies*, Astr. Phys. Vol 36, Issue 1, 31-36 (2012)

V. Berezinsky, *Transition from galactic to extragalactic cosmic rays*, (2007) [arXiv:0710.2750]

X. Bertou et al. *Calibration of the surface array of the Pierre Auger Observatory*, Nucl. Instr. and Meth. A 568 (2006)

P. Bhattacharjee and G. Sigl, *Origin and propagation of extremely high energy cosmic rays*, Phys. Rep. 327 109–247 (2000) [arXiv:astro-ph/9811011]

P. Billoir, *A sampling procedure to regenerate particles in a ground detector from a "thinned" air shower simulation output*, Astropart. Phys. 30, 270 (2008)

C. Bonifazi and P. L. Ghia, *Selection of data periods and calculation of the SD geometrical acceptance*, Internal Auger GAP Note 101 (2006)

C. Bonifazi, A. Letessier-Selvon and E.M. Santos, *A model for the time uncertainty measurements in the Auger surface detector array*, Astropart. Phys. 28, 523 (2008) [arXiv:0705.1856]

C. Bonifazi (Auger Coll.), *The angular resolution of the Pierre Auger Observatory*, Nucl. Phys. B Proc. Sup. 190, 20 [arXiv:0901.3138] (2009)

A. Castellina and L. Collica, *Estimation of the Electromagnetic and Muon shower components* *from the Surface Detector traces*, Internal Auger GAP Note 133 (2012)

A. Castellina and L. Collica, *Measurement of the Muon Signal* S_{μ}*(1000) at 10 EeV in the Pierre Auger Surface Detector*, Internal Auger GAP Note 134 (2012)

A. Castellina and G. Navarra, *Separating the electromagnetic and muonic components in the FADC traces of the Auger Surface Detectors*, Internal Auger GAP Note 65 (2006)

L. Cazon et al., *Time structure of muonic showers* (2003) [arXiv:0311223v1]

L. Cazon et al., *Depth Development of Extensive Air Showers from Muon Time Distributions*, (2005) [arXiv:0412338v2]

L. Cazon et al., *The Muonic Longitudinal Shower Profiles at Production*, (2012) [arXiv:1111.1424v2]

T. Csörgö, et al (TOTEM Coll.), *Elastic Scattering and Total Cross-Section in p+p reactions measured by the LHC Experiment TOTEM at* $\sqrt{s}$*=7 TeV*, Prog. Theor. Phys. Suppl. 193 180 (2012)

J. W. Cronin, T. K. Gaisser and S. P. Swordy, *Cosmic rays at energy frontier*, Scientific American (1997)

J. W. Cronin, *The highest-energy cosmic rays*,Nucl. Phys. B (Proc. Suppl.), 138:465 (2005)

J. W. Cronin, *Recent results from the Pierre Auger Observatory* (2009)

B. R. Dawson et al., *The Energy Spectrum of Cosmic Rays at the Highest Energies* (2013) [arXiv:1306.6138]

D. De Marco and T. Stanev, *On the shape of the ultrahigh energy cosmic ray spectrum*, Phys. Rev. D 72, 081301 (2005)

R. E. Dinnebier, *Powder Diffraction*, 18(3) 199 (2003)

M. Erfani et al., *Simulation Study of Muons in Air Showers (1)*, Internal Auger GAP Note 51 (2013)

M. Erfani et al., *Simulation Study of Muons in Air Showers (2)*, Internal Auger GAP Note 51 (2014)

E. Fermi, *On the origin of the cosmic radiation*, Phys. Rev. 75, 1169– 1174 (1949)

B. Fick et al., *The central laser facility at the pierre auger observatory*, JINST 1, P11003 (2006)

J. W. Fowler et al.,*A Measurement of the Cosmic Ray Spectrum and Composition at the Knee*, Astropart. Phys. 15, 49 (2001)

T. K. Gaisser and A. M. Hillas, *Proc. 15th ICRC*, Plovdiv (1977)

D. G. Gamez et al., *Composition analysis with MPD distributions: A case study at 60 degree zenith angle*, Internal Auger GAP Note 100 (2010)

D. G. Gamez, *Muon Arrival Time distributions and its relationship to the mass composition of Ultra High Energy Cosmic Rays: An application to the Pierre Auger Observatory*, Ph.D. Thesis, Universidad de Granada (2010)

K. Greisen, *Progress in Cosmic-Ray Physics*, vol. 3. Interscience Publishers, New York (1956)

K. Greisen, *End to the cosmic ray spectrum?*, Physical Review Letters 16 748 (1966)

D. Harari, S. Mollerach and E. Roulet, *The toes of the ultra high energy cosmic ray spectrum*, Journal of High Energy Physics 8, 22 (1999)

D. Heck et al., *CORSIKA: A Monte Carlo Code to Simulate Extensive Air Showers*, Report FZKA 6019 (1998)

D. Heck and T. Pierog, *Extensive Air Shower Simulation with CORSIKA: A User's Guide*, KIT (2011)

W. Heitler, *Quantum Theory of Radiation*, Oxford University Press (1954)

J. Hersil et al.,*Observations of Extensive Air Showers near the Maximum of Their Longitudinal Development*, Phys. Rev. Lett. 6, 22 (1961)

V. Hess, *Uber Beobachtungen der durchdringenden Strahlung bei sieben Freiballonfahrten*, Physik. Zeitschr. 13, 1084–1091 (1912)

A. M. Hillas, *The origin of ultra high energy cosmic rays*, Ann. Rev. Astr. Astrophys. 22, 425 (1984)

A. M. Hillas, *Cosmic Rays: Recent Progress and some Current Questions* (2006) [arXiv:astro-ph/0607109]

N. N. Kalmykov and S. S. Ostapchenko, *The nucleus-nucleus interaction, nuclear fragmentation, and fluctuations of extensive air showers*, Physics of Atomic Nuclei 56, 346–353 (1993)

K. H. Kampert, *Ultra-High Energy Cosmic Rays: results and prospects* (2014) [arXiv:1404.6515v1]

B. Kegl, D. Veberic and S. Micanovic, *Estimating Muon Fraction from Individual Traces of SD Stations*, Internal Auger GAP Note 126 (2012)

E. Kido and O. E. Kalashev (TA Coll.), *Constraining UHECR source models by the TA SD energy spectrum* (2013) [arXiv:1310.6093v2]

D. Kuempel, K. Kampert and M. Risse, *Geometry reconstruction of fluorescence detectors revisited*, Astropart. Phys. 30, 167 (2008)

C. Jui et al. (TA Coll.), *Cosmic Ray in the Northern Hemisphere: Results from the Telescope Array Experiment*, Proc. APS DPF Meeting (2011) [arXiv:1110.0133]

A. Letessier-Selvon and T. Stanev, *Ultrahigh Energy Cosmic Rays* (2011) [arXiv:1103.0031v1]

A. Letessier-Selvon, *Highlights from the Pierre Auger Observatory*, 33th ICRC (2013)

A. Letessier-Selvon et al., *Layered Water Cherenkov Detector for the Study of Ultra High Energy Cosmic Rays* (2014) [arXiv:1405.5699v1]

J. Matthews, *A Heitler model of extensive air showers*, Astropart. Phys. 22, 387-397 (2005)

M. Morhac et al., *Efficient one- and two-dimensional Gold deconvolution and its application to gamma-ray spectra decomposition*, Nuclear Instruments and Methods in Physics Research A 401, 385-408 (1997)

M. Mostafa, *The Hybrid Activities of the Pierre Auger Observatory*, Nucl. Phys. B Proc. Suppl. 165, 50–58 (2007)

M. Nagano and A. A. Watson, *Observations and implications of the ultrahigh- energy cosmic rays*, Rev. Mod. Phys. 72, 689 (2000)

D. Newton, J. Knapp and A. A. Watson, *The optimum distance at which to determine the size of a giant air shower* (2006) [arXiv:astro-ph/0608118]

T. Nonaka et al., *The present status of the Telescope Array experiment*, Nucl. Phys. B Proc. Suppl. (2009)

R. Pesce for the Pierre Auger Collaboration, *Proc. 32nd ICRC*, (2011) [arXiv:1107.4809v1]

S. Ostapchenko, *Nonlinear screening effects in high energy hadronic interactions*, Phys. Rev. D74 014026 (2006)

S. Ostapchenko, *Monte Carlo treatment of hadronic interactions in enhanced Pomeron scheme: QGSJET-II model*,Phys. Rev. D 83 014018 (2011)

T. Pierog and K. Werner, *EPOS Model and Ultra High Energy Cosmic Rays*, Nucl. Phys., Proc. Suppl. 196 102 (2009)

T. Pierog, *LHC results and High Energy Cosmic Ray Interaction Models*, J. Phys.: Conf. Ser. 409 012008 (2013)

T. Pierog, *talk at the 27th MACROS Workshop*, Paris (2013)

H. M. Rivera Bretel, *Measurement of the energy spectrum of cosmic rays above* $3x10^{17}$ *eV using the infill array of the Pierre Auger Observatory*, Ph.D. Thesis, Universita' di Milano (2014)

F. Schmidt et al., *Applying Extensive Air Shower Universality to Ground Detector Data*, (2007) [arXiv:0706.1990v2]

B. Smith, C. Wileman and A. A. Watson, *The risetime as an indicator of the mass composition of UHECRs*, Internal Auger GAP Note 110 (2007)

P. Sokolsky and G. B. Thomson, *Highest energy cosmic-rays and results from the HiRes experiment*, J. Phys. G: Nucl. Part. Phys. 34 R401 (2011)

T. Stanev, *High Energy Cosmic Rays*, Springer Praxis Books (2010)

T. Stanev, *Ultrahigh Energy Cosmic Rays: Review of the Current Situation* (2012) [arXiv:1210.0927v1]

R. Ulrich, R. Engel and M. Unger, *Hadronic multiparticle production at ultrahigh energies and extensive air showers*, Phys. Rev., D83:054026 (2011)

M. Unger et al., *Reconstruction of Longitudinal Profiles of Ultra-High Energy Cosmic Ray Showers from Fluorescence and Cherenkov Light Measurements*, Nucl. Instrum. Meth. A 588 (2008) 433

M. Unger, *Cosmic Rays above the Knee* (2008) [arXiv:0812.2763]

E. Varela (Auger Coll.), *The low-energy extensions of the Pierre Auger Observatory*, Journal of Physics 468 (2013)

A. A. Watson, *High-energy cosmic rays and the Greisen-Zatsepin-Kuzmin effect*, (2013) [arXiv:9709187v1]

B. Zamorano, *Inferring the mass composition of UHECR through the characterization of the muon production profile*, Ph.D. Thesis, Universidad de Granada (2014)

G. T. Zatsepin and V. A. Kuzmin, *Upper limit of the cosmic-ray spectrum*, Zh. Eksp. Teor. Fiz., Pisma Red. 4, no. 3, 114–17 (1966)